IMAGE IMPROVEMENT USING DYNAMIC OPTICAL

LOW-PASS FILTER

by

Branko Petljanski

A Dissertation Submitted to the Faculty of

The College of Engineering and Computer Science

in Partial Fulfillment of the Requirements for the Degree of

Doctor of Philosophy

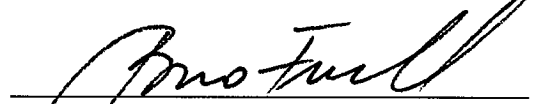Florida Atlantic University

Boca Raton, Florida

May 2010

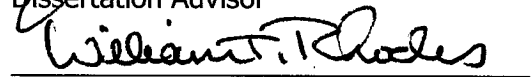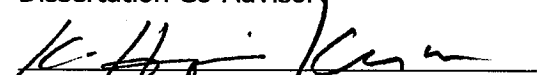IMAGE IMPROVEMENT USING DYNAMIC OPTICAL LOW-PASS FILTER ·

by

Branko Petljanski

This dissertation was prepared under the direction of the candidate's dissertation advisor, Dr. Borko Furht, Department of Computer & Electrical Engineering and Computer Science, and has been approved by the members of his supervisory committee. It was submitted to the faculty of the College of Engineering and Computer Science and was accepted in partial fulfillment of the requirements for the degree of Doctor of Philosophy.

SUPERVISORY COMMITTEE:
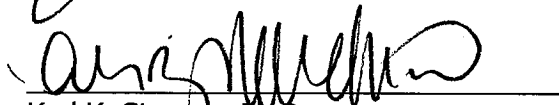
Borko Furht, Ph.D.
Dissertation Advisor

William T. Rhodes Ph.D.
Dissertation Co-Advisor
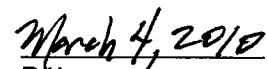
Hari Kalva, Ph.D.

Oge Marques, Ph.D.

Borko Furht, Ph.D.
Chair, Department of Computer & Electrical Engineering and Computer Science

Karl K. Stevens, Ph.D.
Dean, College of Engineering and Computer Science

Barry T. Rosson, Ph.D.
Dean, Graduate College

March 4, 2010
Date

ii

Acknowledgments

I could not have done any of this without my parents' moral support, for which I am very grateful. They have encouraged me in anything I have ever endeavored, and this project is no exception.

Finally I wish to thank my wife Audrey, whose unconditional support made this project much better in many ways. I dedicate this dissertation to her.

Los Angeles, California   Branko Petljanski

January 27, 2010

Abstract

Author: Branko Petljanski

Title: Image Improvement using Dynamic Optical Low-pass Filter

Institution: Florida Atlantic University

Dissertation advisor: Dr. Borko Furht

Degree: Doctor of Philosophy

Year: 2010

Professional imaging systems, particularly motion picture cameras, usually employ larger photosites and lower pixel counts than many amateur cameras. This results in the desirable characteristics of improved dynamic range, signal to noise and sensitivity. However, high performance optics often have frequency response characteristics that exceed the Nyquist limit of the sensor, which, if not properly addressed, results in aliasing artifacts in the captured image.

Most contemporary still and video cameras employ various optically birefringent materials as optical low-pass filters (OLPF) in order to minimize aliasing artifacts in the image. Most OLPFs are designed as optical elements with a frequency response that does not change even if the frequency responses of the other elements of the capturing systems are altered. An extended evaluation of currently used birefringent-based OLPFs is provided.

In this work, the author proposed and demonstrated the use of a parallel optical window positioned between a lens and a sensor as an OLPF. Controlled X- and Y-axes rotations of

the optical window during the image exposure results in a manipulation of the system's point-spread function (PSF). Consequently, changing the PSF affects some portions of the frequency components contained in the image formed on the sensor. The system frequency response is evaluated when various window functions are used to shape the lens' PSF, such as rectangle, triangle, Tukey, Gaussian, Blackman-Harris etc.

In addition to the ability to change the PSF, this work demonstrated that the PSF can be manipulated dynamically, which allowed us to modify the PSF to counteract any alteration of other optical elements of the capturing system. There are several instances presented in the dissertation in which it is desirable to change the characteristics of an OLPF in a controlled way. In these instances, an OLPF whose characteristics can be altered dynamically results in an improvement of the image quality.

Table of Contents

List of Tables

List of Figures

Chapter 1

Introduction and Motivation

The common use of terminology such as "digital photography" and "digital audio" belie the fact that virtually all transducers such as microphones for recording audio or CCDs and CMOS devices for capturing images are analog devices. It is commonly accepted that digital equivalents of images, video, music, and other signals that originate in the analog world can be the starting point for various post processes, evaluation, and research. What is often ignored is that, before digital processing algorithms can be implemented, from the simplest to the most complex, an operation involving the conversion of a continuous analog signal into a discrete, quantized digital equivalent has to be performed. The conditions for capturing and converting analog signals into their digital equivalents, which are often unknown, are fundamental to our understanding of the validity of the results of any subsequent processing, evaluation, or research. Once the signal is digitized, an accurate reconstruction from the quantized digital data may not be possible.

Commercially available imaging systems in particular often employ preprocessing before digitization, the details of which are often well guarded secrets by the equipment manufacturers. This, despite the fact that the characteristics of these preprocesses fundamentally affect the accuracy of the reconstructed result. In the following work, an attempt to shed some light on this portion of the technology will be presented.

In any imaging system, the lens is an essential part of the capturing system, performing the function of collecting light energy from the scene and producing an image on the transducer. A lens can be as simple as a single element, or as complex as modern cine zoom lens with more than 26 optical elements. Minimizing optical aberrations has occupied some of the greatest minds of mankind for over a thousand years. The corrections of these artifacts, both achromatic and chromatic, are done in the analog domain, which makes these corrections especially challenging. Lenses are entirely analog devices, and they have been used in "digital" image acquisition unmodified, even though they may originally have been designed for an analog imager such as a silver halide film emulsion. Interchangeable lenses are often used on cameras with various resolution sensors that match only in optical size. Even with today's highs speed computers running sophisticated ray tracing software, designing and manufacturing high-quality lenses is an expensive and lengthy process. Mass production of electronics has resulted in a situation in which producing a good-quality lens can be more expensive than all other aspects of the image acquisition system.

Although image sensors are based on an analog process—the conversion of photons to electrons—with the advent of CMOS devices with integral A/D converters they became digital devices that perform conversion from the continuous to the discrete spatial domain. Their system performance is often not defined by technology but by their manufacturer's marketing department. Currently we are at a crossroad between CMOS and CCD processes used for sensor manufacturing. However, whatever process is used, the photosite dimension and the distance between their centers determine the sampling frequency of the sensor and, therefore, its Nyquist frequency. Recently, the size of the photosite has been determined mostly by market forces rather than optimization. The race to market to manufacture a sensor with a higher number of photosites than the

competition has resulted in very small photosite sizes that place an impossible burden on camera optics, electronics, and storage. An often ignored rule of thumb, suggests that the smallest desired resolution element should be matched in size by the minimum sensor element. Another useful rule of thumb states that, in a diffraction-limited system, the Airy disk diameter in the visible part of the spectrum is approximately equal to the F-number of the system expressed in microns. For example, the smallest photosite dimension is currently 1.4 μm x 1.4 μm, which would require, based on the aforementioned rules, an aberration-free lens faster than F1.4 to appreciate such small photosites (pixels). The race to produce the smallest photosite and, therefore, the highest pixel count has gone so far that some sensors are being compared by their pixel density rather than the total number of pixels. Beside the dynamic range and noise problems present in the systems with such minute pixels, these capturing systems suffer from optical limitations as well. The sensor is often designed independently from the lens, resulting in frequency response discrepancies between these two critical elements of the capturing system.

Recognizing this problem, professional imaging systems, particularly motion picture cameras, usually employ larger photosites (pixels) and lower pixel counts than many amateur cameras. This results in the desirable characteristics of improved dynamic range, signal to noise and sensitivity. However, high performance optics often have frequency response characteristics that exceed the Nyquist limit of the sensor.

This mismatch between the lens and the sensor frequency characteristics results in an irreparable artifact that must be minimized for the majority of applications.

The Nyquist criterion requires that the sampling frequency must be at least twice the desired system bandwidth; therefore it is necessary to reduce the bandwidth of the lens before the image is formed on the discrete imaging array. Typically, an optical filter, employing the principle of birefringence, is placed between the lens and the imager. This

optical low-pass filter (OLPF) is designed to match the lens performance with sensor performance. Despite the fact that the frequency response of the capturing system is, in good part, determined by the frequency response of the OLPF (the frequency response of the OLPF is in the upper boundary of the frequency response of the system), the characteristics and construction of this obscure optical element are rarely published. This might be partially because its function is to intentionally blur the image before it is formed on the sensor. Inserted between the lens and the sensor, the optical low-pass filter degrades the image in spite of the hard work that was put into designing the lens and the sensor. It will be shown in the dissertation that certain types of optical low-pass filters can be analyzed using the tools from discrete signal processing, although they essentially belong to the analog domain.

Due to its interesting position between the analog and digital worlds, the fundamental importance of the OLPF in defining the imaging system performance is often ignored. This situation has motivated the author to investigate the current limitations of OLPFs and to propose and demonstrate an alternative approach. As we will see, the proposed solution can dynamically modify its characteristic, which allows an interesting possibility in reference to performing real-time signal processing in the analog domain.

There are several instances in which it is desirable to change the characteristics of an optical low-pass filter in a controlled way; to compensate for the performance of a particular lens or the characteristics of a lens that varies with aperture, or when the spatial characteristics of an sensor change due to binning or sub-sampling, or when integration time and subject or camera movement result in a reduction of high frequency content. In all of these instances, an optical low pass filter whose characteristics can be altered dynamically results in an improvement in image quality when compared to the fixed

frequency response of the traditional birefringent OLPF. Thus, there is a need for an improved optical low-pass filter that remedies the shortcomings of the prior solutions.

1.1 Contribution

The main contributions of this work are that it provides:

- A novel optical low-pass filter based on a dynamically controlled parallel optical window or rigid mirror,
- Theoretical analysis and practical implementation of various window functions for shaping the point spread function of the optical capturing system using the DOLPF,
- A proposal and demonstration of coupling the DOLPF with other elements of the capturing system with a goal to dynamically counteract alterations of the modulation transfer functions,
- The practical implementation and related problems of an optical low-pass filter based on the parallel optical window,
- Detailed analysis of currently used birefringent optical low-pass filters.

1.2 Organization

This Ph.D. dissertation is structured as follows: Chapter 2 introduces some basic theory that is necessary for a better understanding of the work, including the sampling theory with examples, cause of aliasing in the sample systems, introduction to optical prefiltering, a brief introduction to the modulation transfer function of lenses, and a rule for MTFs of optical elements when they are cascaded. Chapter 3 contains a review of the theory behind the OLPFs with an emphasis on their current implementation in modern digital still and video cameras. In Chapter 4, we propose a novel, dynamically controlled optical low-pass filter, its principle of operation, and the possible use of such a device. Chapter 5

summarizes the results of the experiments with a device built based on the proposal. In Chapter 5, we present the methods used in evaluation of the system with a dynamically controlled optical low-pass filter. Chapter 6 provides conclusions and proposes some future research regarding the presented work. Lastly, the appendix contains graphs from the optical simulation that were not reported in the main text.

Chapter 2

Preliminaries

In this chapter, the modulation transfer function (MTF) is used, for the first time, to describe the frequency responses of the optical elements of the image capturing system. The MTF is the magnitude response of the optical element or system to sinusoidal patterns of different spatial frequencies [1]. It is often plotted as a function of frequency, expressed in line pairs per millimeter (lp/mm).

Throughout all chapters, the characteristics of the capturing system or its elements are frequently shown as a function of the F-number—i.e., the lens's focal length divided by the clear aperture diameter [2]. In addition to controlling the amount of light energy that reaches the sensor, the frequency components of the continuous scene that passes through the lens are altered by an amount that is a function of the F-number. Due to the importance of the lens's frequency response, a section of this chapter is dedicated to that phenomenon.

Sampling is the essential part of the digitizing process, and a section of this chapter is dedicated to two-dimensional sampling. The sampling theory is supported by three practical examples. An adverse consequence of sampling, aliasing, is briefly discussed in this chapter as well.

The last section of this chapter analyzes the MTF of the capturing system when the system consists of several cascaded optical elements that are characterized by their own MTFs.

2.1 Sampling

The first step of any digital image or video processing is the conversion of a continuous scene into a digital equivalent by digitization. The digitization can be applied onto the various scopes of the signal such as intensity, time, and space. The digitization over the regular sampling grid—a grid with equal distance between samples in one direction—is the most common, and it will be a focus of this study.

When sampling a continuous signal over the regular grid, a question arises about the distances between the sampling points. The Nyquist sampling theorem states that in order to acquire a discrete equivalent of a continuous signal, the signal should be sampled by at least twice the maximum bandwidth of the continuous signal. Half of the sampling frequency is called the Nyquist frequency.

When a continuous tone image is sampled by a device that has a discrete sampling structure, the frequencies present in the scene tend to exceed the Nyquist frequency because of the practical constraints of the capturing system. Violating the Nyquist-Shannon sampling theorem results in aliasing, an irreversible process that permanently contaminates the discrete equivalent of the continuous scenes.

For practical reasons, a sensor has a finite size and a finite number of photosites. The physical dimensions of the sensor and the number of photosites determine the geometrical shape and dimensions of the photosites. The centers of the photosites' light-sensitive areas mark the positions of the sensor's sampling points. The distances between these points determine the sampling frequency, which is usually expressed in pixels per millimeter. In the following sections, the sampling structures of three different sensors are studied in detail. The sensors are evaluated depending on two characteristics: their Nyquist frequencies (expressed in lp/mm) and their modulation transfer functions.

2.1.1 Two-dimensional sampling and sensors' MTFs

The photosites of an image sensor are designed with various geometrical shapes and orientations. Furthermore, to separate color information in the sampled scene, the color sensors are designed with various color filter arrays (CFA), which are placed over the photosites. Figures 2.1(a) and 2.1(b) show examples of the two typical modern color sensors: the stripe CFA and the Bayer pattern CFA, respectively. Figure 2.1(c) shows the experimental diagonal stripe CFA pattern incorporated in the Panavision Dynamax sensor [3]. Note that the photosites in the third sensor are rotated by 45°.
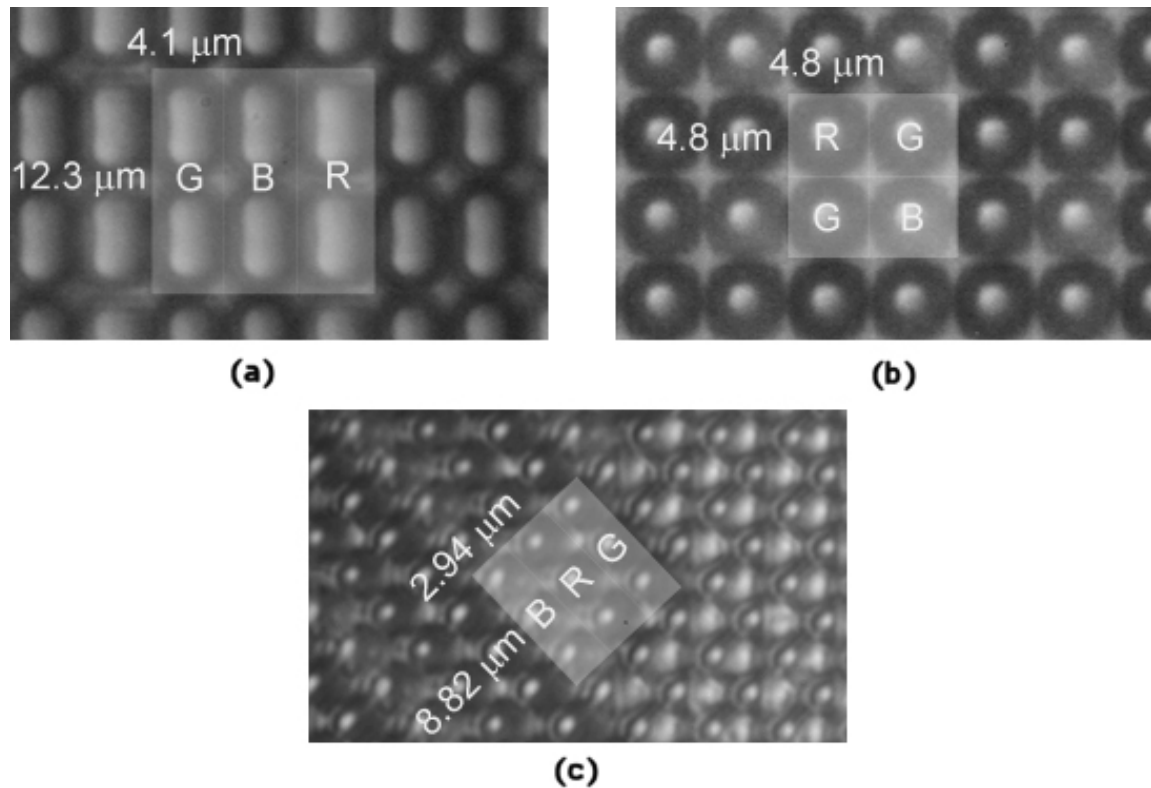
Figure 2.1: (a) 400x-magnified photosites of the Panavision Genesis camera, demonstrating the stripe CFA. (b) The Bayer pattern CFA of the Olympus E510 sensor. (c) Panavision Dynamax Blue photosites with a diagonal stripe pattern.

The shape of the photosite determines the frequency response of the image sensor. The pixel pitch, defined as the distance between the centers of photosites of the same color, determines the sampling frequency and the Nyquist frequency of the sensor.
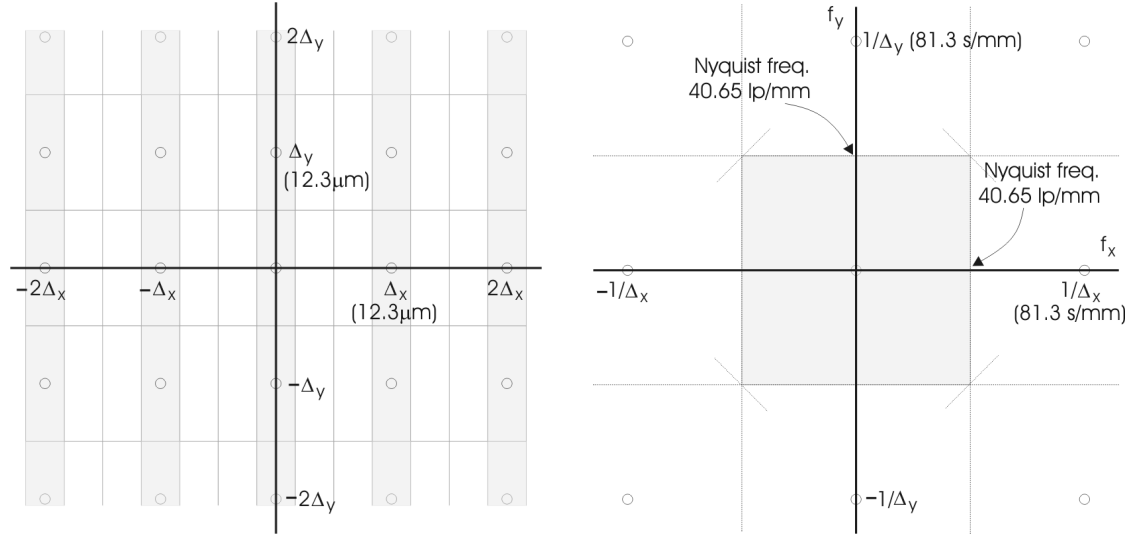
Figure 2.2: The spatial distribution of same-color photosites found in the Genesis sensor is shown on the left. The horizontal and vertical Nyquist frequencies are shown on the right.

Using the lattice theory [4], we can formalize the sampling structure and the frequency response of a sensor. Figure 2.2, on the left, shows same-color photosites and the distances between them. As seen in the figure, the horizontal and vertical distances between centers of same-color photosites are both 12.3 μm. Hence, the horizontal and vertical sampling frequencies for each color are 81.3 samples/mm. The lattice representation of the Genesis sensor, shown on the right side of Figure 2.2, helps us to determine the Nyquist frequencies. As seen in the figure, the horizontal and vertical Nyquist frequencies are 40.65 lp/mm. The gray square on the same figure shows a contour of the ideal frequency prefilter for this sampling structure that is required to prevent aliasing.

The lattice theory is useful for determining the Nyquist frequency of a sensor sampling structure, but it does not reveal the sensor's frequency response. The frequency response

is determined by the shape of the photosensitive area of a photosite. If the photosensitive area is infinitely small (i.e., point sampling), then the frequency response of the imager would be infinite. Of course, a sensor with infinitely small photosites would have poor sensitivity. Therefore, the pixel designers' goal is to maximize the photosensitive area of a photosite. A measure of their success is the ratio between the photosensitive area and the total photosite area; this ratio is called the fill factor [5]. To demonstrate how the dimensions of a photosite determine the sensor frequency response, we will assume that the fill factor has a value of 100% (a value not achievable in practice). As seen in Figure 2.2, the photosensitive area forms a rectangle in the spatial domain, which results in a sinc function in the frequency domain. The left side of Figure 2.3 shows the horizontal and vertical MTFs of the sensor. On the right side is a 2D representation of the sensor's MTFs.
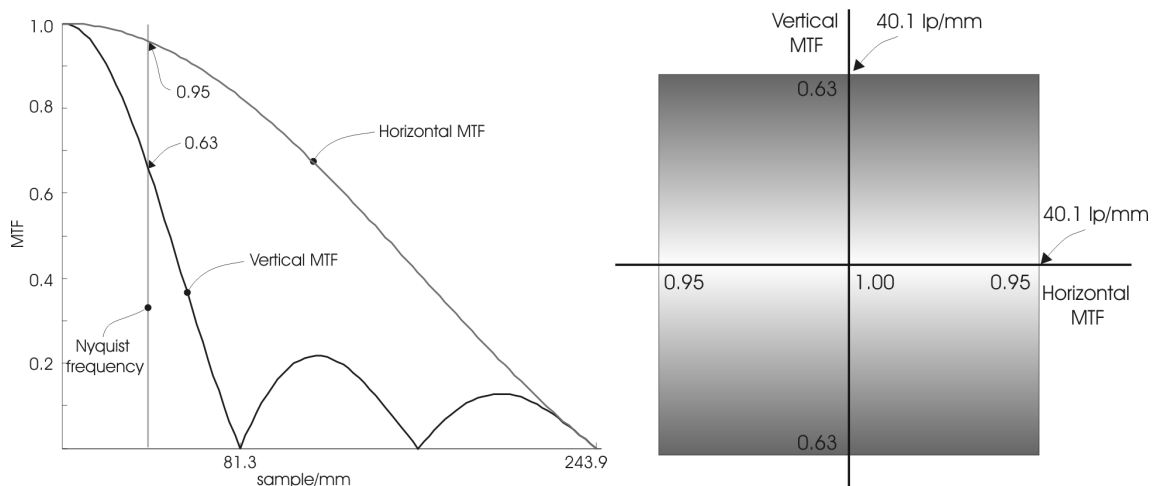
Figure 2.3: On the left are the horizontal and vertical MTFs of the Genesis sensor. On the right is a 2D representation of the sensor's MTFs.

As seen in the figure, the horizontal MTF of the sensor is better than the vertical MTF. It will be shown in Chapter 3 that this asymmetric MTF requires an asymmetric optical low-pass filter. The stripe-pattern CFA has the same bandwidth for all three colors; hence, the MTFs for all three colors are the same. The sensor found in the Olympus E-510 camera has the Bayer pattern CFA, with red and blue photosites located on a rectangular structure

11

while the green photosites form a diagonal sampling structure. Figures 2.4 and 2.5 show the spatial distribution of the green samples, the Nyquist frequency response, and the 1D and 2D MTFs. The diagonal Nyquist frequency is lower than the horizontal and vertical Nyquist frequencies. The sensor's frequency responses for the red and blue samples are different from those for the green samples. In all cases, the MTF responses are symmetric.
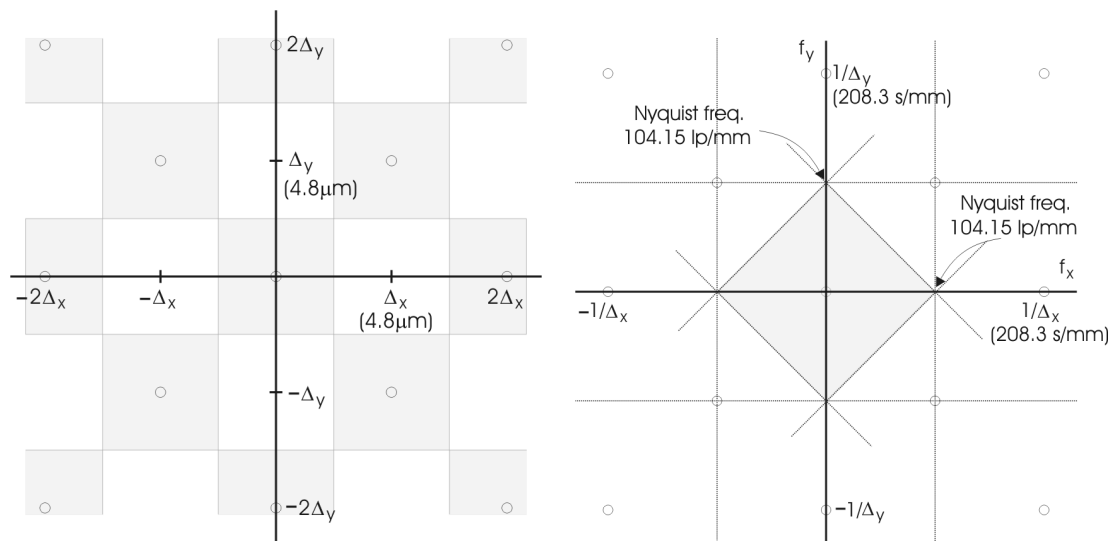
Figure 2.4: Green photosites from the Olympus sensor are depicted on the left. The horizontal and vertical Nyquist limits are shown on the right.
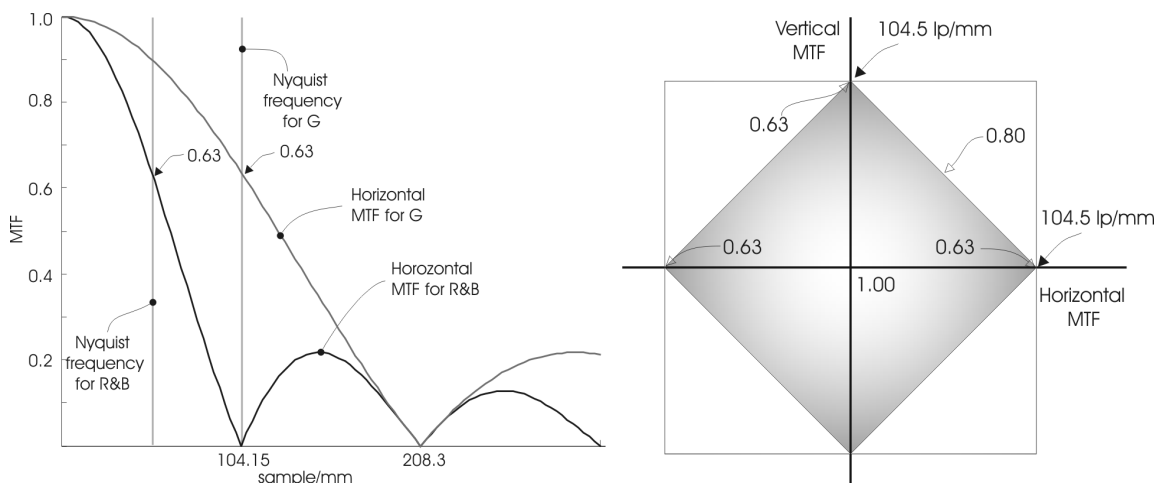
Figure 2.5: On the left is the horizontal MTF for the three colors in the Olympus sensor. On the right is a 2D representation of the sensor's MTFs for the color green.

The Dynamax sensor has the diagonal stripe CFA; the spatial distribution of its one-color photosites is shown in Figure 2.6. The same figure shows the Nyquist limits for the sensor. The sensor's MTFs are evaluated on the main and minor diagonals and are shown in Figure 2.7. As seen on the right side, the horizontal and vertical MTFs are equal, whereas the diagonal frequency responses differ significantly.
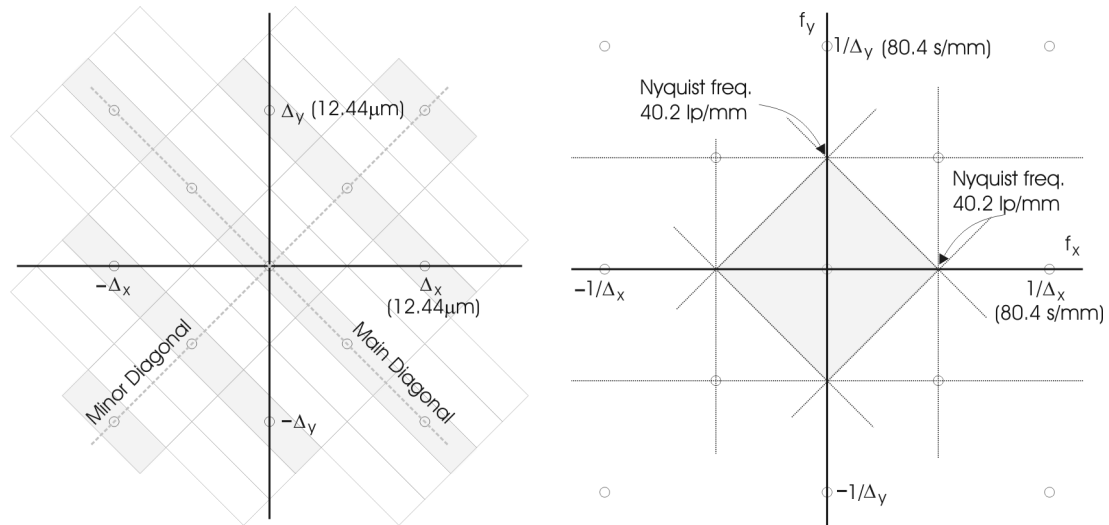
Figure 2.6: Green photosites in the Dynamax sensor are depicted on the left. The horizontal and vertical Nyquist frequency limits are shown on the right.
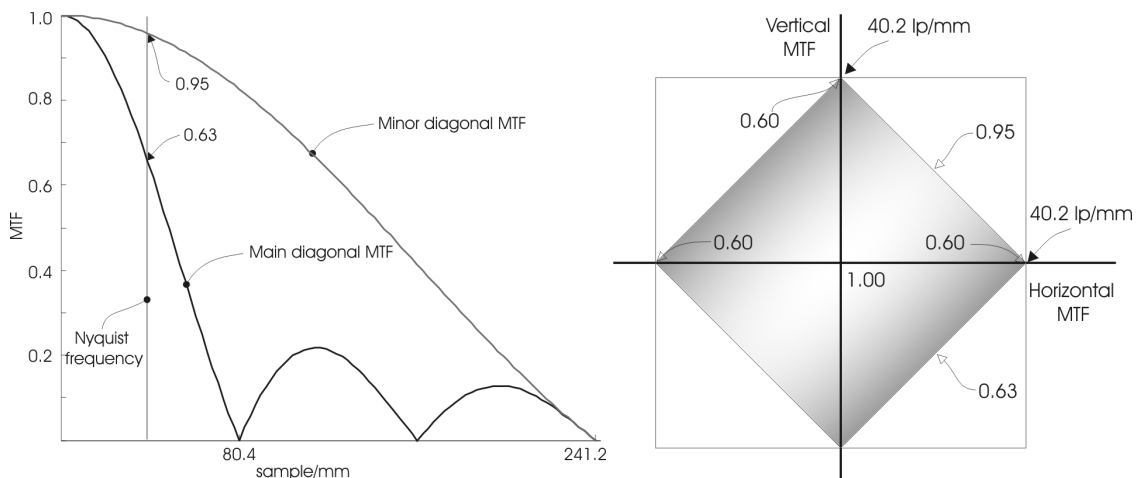
Figure 2.7: On the left are the main and minor diagonals of the sensor's MTFs for the three colors. On the right is a 2D representation of the sensor's MTFs.

2.1.2 Aliasing

As the frequency-domain representation of sampling [6] shows, the result of sampling is periodically repeated copies of the Fourier transform of the continuous scene formed on the sensor. The copies are shifted by integer multiples of the sampling frequency. Hence, when a continuous scene contains frequency components greater than half of the sampling frequency (i.e., greater than the Nyquist frequency), aliasing will occur in the captured image. Figure 2.8 depicts the "wrapping" effect of the frequency components that are above the Nyquist frequency. As seen in the figure, the frequency components higher than the Nyquist frequency "wrap" around the Nyquist frequency. The frequency components above the sampling frequency wrap around the DC level.
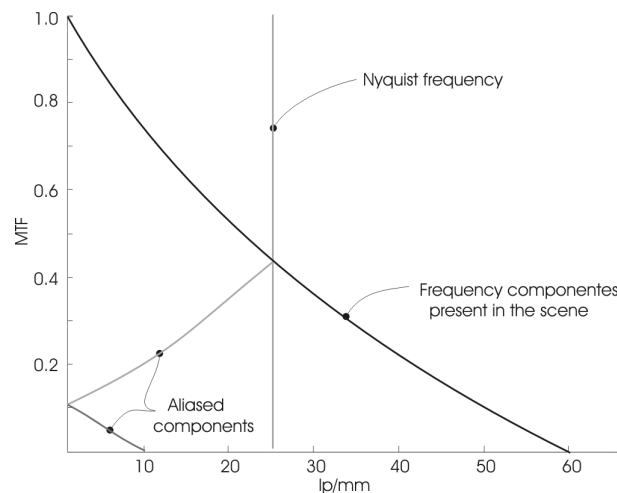
Figure 2.8: An illustration of the aliasing of an arbitrary signal, with the frequency components above the Nyquist frequency.

On the right sides of Figures 2.2, 2.4, and 2.6 are shown 2D illustrations of the Nyquist limitations for the three sensors. The gray squares represent the extent of the frequency components that are correctly captured if they are present in the image formed on the sensor. However, the frequency components that are outside the gray square will be incorrectly interpreted by the sensor. Figure 2.9 shows one example of the scene,

14

captured with the Genesis sensor (with the OLPF removed), which contains horizontal frequency components that are below and above the Nyquist limits. The original frequencies and the sensor's Nyquist limit are indicated in the figure. The frequency components above the Nyquist frequency wrap around and appear as the lower frequencies. For example, the 70 lp/mm sinusoidal pattern appears as a 10 lp/mm pattern in the digital equivalent.
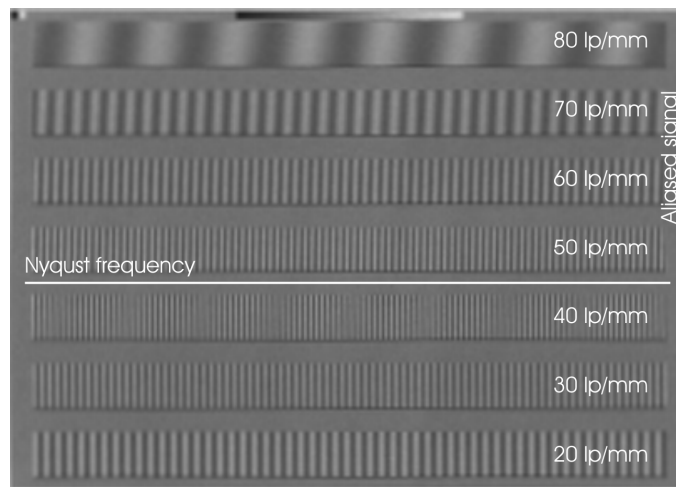
Figure 2.9: The green color plane of an image captured with the Genesis sensor, illustrating aliasing. On the right are indicated the original frequency components of the continuous scene that is formed on the sensor.

2.1.3 Binning and decimation

Some sensors [7] reduce the number of photosites that are transferred off-chip in order to increase the frame rate and/or sensitivity. There are two ways to conduct this operation on-chip: binning and spatial decimation. In the binning method, two or more photosites are tied together and transferred off-chip as one value. The binning can be deployed horizontally, vertically, or in both directions. The spatial decimation approach transfers only selected photosites off the sensor. For example, every second vertical photosite can

be sent off-chip (i.e., every second line). As in the binning method, the decimation can be deployed horizontally, vertically, or in both directions.

When two or more photosites are binned, the locations of the binned photosites' centroids determine the Nyquist frequency in the direction of the binning. For example, vertically binning two photosites from Figure 2.2 would halve the vertical Nyquist frequency. In addition to altering the Nyquist frequency, the binning lowers the sensor's MTF in the given direction, due to the changed dimensions of the photosensitive area.

When the spatial decimation is used, the locations of the selected photosites determine the Nyquist frequency in the direction of decimation. For example, vertically decimating every second photosite from Figure 2.2 would halve the vertical Nyquist frequency. Unlike the binning method, the decimation improves the MTF of the sensor in the direction of decimation, due to the relatively smaller photosensitive area that results.

2.2 Optical prefiltering

As seen in the previous sections, the frequency components that are contained in the continuous scene formed on the sensor and that are higher than the Nyquist frequencies are incorrectly interpreted by the sensor, which results in aliasing. When an application requires minimizing aliased components, the frequency components above the Nyquist frequency must be minimized, using an optical element called an anti-aliasing filter or an optical low-pass filter (OLPF). The right sides of Figures 2.2, 2.4, and 2.6 show the non-zero regions of the ideal OLPFs for each given sensor, beside the Nyquist limits of the sensors. The amplitude of such an ideal filter is the unity across the non-zero region and is zero elsewhere. In Chapter 3, various implementations of OLPFs, a detailed explanation of their principles, and various examples are presented.

2.3 Lens's MTF

A study of the sensor's MTFs is a topic of the previous section, whereas a detailed study of the OLPF is presented in Chapter 3. The lens is the third essential optical element of the capturing system, and its influence on the overall system performance is briefly analyzed in the following text. A lens's performance can be appraised on many parameters, but in this section, the focus is the lens's effect on the frequency responses of the capturing system. Figure 2.10 shows the MTFs of a Nikon 50 mm lens, which is a typical 35mm photographic lens, measured on the optical axis using the MTF bench.
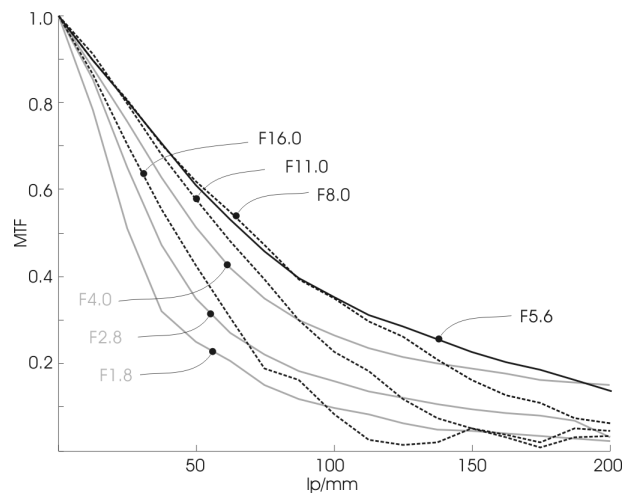
Figure 2.10: MTFs of the Nikon 50 mm lens, measured with the MTF bench.

As seen in the figure, the best lens performance, in terms of MTF, occurs when the aperture size is set to F5.6. Other aperture settings result in lower MTFs. In general, when a smaller aperture is selected, the most dominant limitation of the lens's MTF is caused by the diffraction. On the other hand, when a selected aperture is greater than F5.6, the MTFs of the lens are mostly dominated by the lens's geometrical aberrations. The cutoff frequency of the MTF that is dominated by aberration is still determined by the diffraction effect. However, aberration can reduce the high frequency components of the MTF and can effectively lower the cutoff frequency much more than what is predicted by diffraction.

The lens's optical transfer function (OTF) can be found directly from a Fourier transform of the lens's point spread function (PSF). The lens's modulation transfer function is then obtained by taking a modulus of the OTF. In the case of the diffraction-limited incoherent imaging, the lens's PSF (also known as the lens's impulse response) is proportional to the Fraunhofer diffraction pattern of the exit pupil—i.e., the image of the aperture stop when looking into the rear of the lens [2]. When the conditions for the Fraunhofer approximation are satisfied, the Fraunhofer diffraction pattern (and the lens's PSF) can be found directly from a Fourier transform of the aperture intensity function [8].
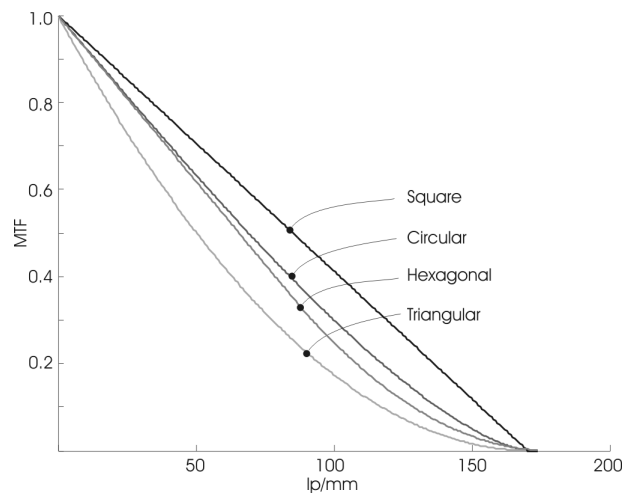
Figure 2.11: The MTFs for a diffraction-limited lens and various aperture intensity functions.

A high-quality lens usually has an aperture stop that approximates a circle, resulting in a circular intensity function. Figure 2.11 shows the MTFs of a diffraction-limited lens, with various aperture intensity functions calculated for the same F-number. As seen in the figure, the lens with the aperture stop constructed of three blades (resulting in a triangular intensity function) has a lower MTF than the same lens with other types of aperture stops. The MTF of the aperture stop constructed with six blades is similar to the MTF of the aperture that has a circular intensity function. Figure 2.12 shows the theoretical MTFs of an aberration-free lens that is diffraction limited, with various circular aperture sizes. The

18

dashed curves on the figure show the measured MTFs for the Nikon 50mm lens and for

three aperture sizes. As seen in the figure, the measured MTFs closely track the

theoretical curves for F16 and F11. On the other hand, when the lens aperture size

increases, other lens limitations become dominant in affecting the lens's MTF. Hence, the

diffraction limitation curves are no longer valid.
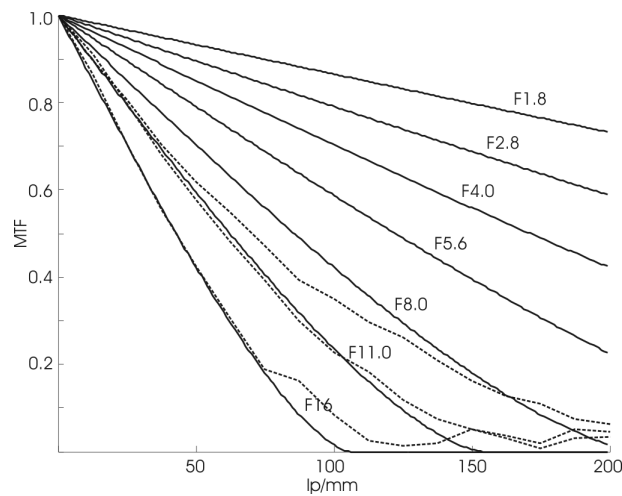
Figure 2.12: Theoretical MTFs of an aberration-free lens that is diffraction limited. The curves, calculated for monochrome light λ=587nm, are shown in full black lines. The dashed lines show the measured MTFs of the Nikon 50mm lens, with the aperture set to F16, F11, and F8.

As the lens aperture increases, the geometrical aberrations start to dominate the

limitation of the MTF. Spherical aberration, coma, and other aberrations are complex and

not straightforward; hence, they are difficult to describe in a closed form like the

diffraction-based limitation. Lens designers exercise great effort in order to minimize these

aberrations, and the quality of a lens is often determined by its success or failure in

minimizing the geometrical aberrations. In the following chapters, the effects of the

aberrations on the lens's MTF are observed and considered, albeit without examining the

specifics of these aberrations.

2.4 Cascading optical elements and their MTFs

An image-capturing system typically consists of multiple optical elements cascaded into one device. Before the continuous scene reaches the sensor, it is altered by each of the optical elements that precede the sensor. By passing through the optical elements, many image parameters are affected; however, the alteration of the image frequency components is the primary interest of this study. The behavior of each optical element (in the frequency domain) is described by its MTF. Figure 2.12 illustrates a system that consists of two optical elements, each with a different MTF. As the aggregate MTF explicitly shows, the frequencies in the image that enters the system are altered before the image emerges at the opposite end. The aggregate MTF is obtained by calculating the Fourier transform of the combined impulse response, which is calculated by spatially convolving the impulses responses of the two optical elements. The aggregate MTF is obtained by normalizing (i.e., providing unit value at zero spatial frequency) the frequency magnitude response of the system. When the MTF of each optical element is known, the easiest way to find the aggregate MTF is by multiplying the MTFs of the two elements, frequency by frequency [6].

<div align="center">

Optical element 1   Optical element 2

Input image → $h_1(x, y)$ $MTF_1(f_x, f_y)$ → $h_2(x, y)$ $MTF_2(f_x, f_y)$ → Output image

$$MTF_{agr.}(f_x, f_y) = MTF_1(f_x, f_y) \cdot MTF_2(f_x, f_y)$$

$$h_{agr.}(x, y) = h_1(x, y) \star h_2(x, y)$$

</div>
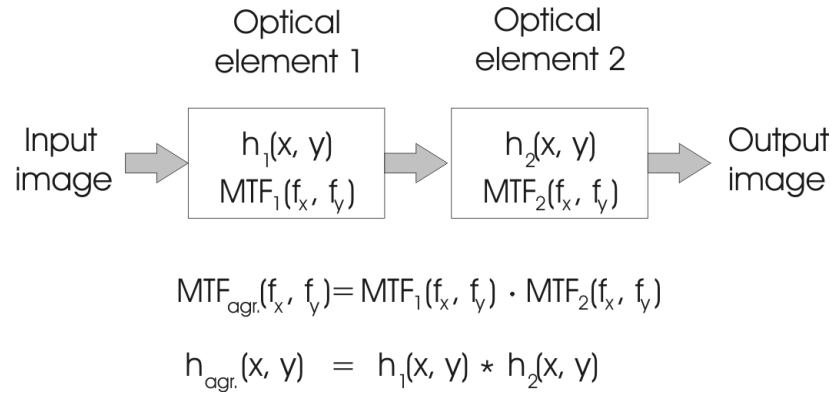
Figure 2.13: A capturing system consisting of two optical elements, each with different impulse responses and MTFs.

The consequence of multiplying normalized functions, which are less than or equal to unity, is that the aggregate MTF is always lower than or at least equal to the lowest MTF of the element. For example, if the MTF of the first element in Figure 2.12 at 30 lp/mm is 0.5, and the MTF of the second element, at the same frequency, is 1.0, then the overall MTF at the given frequency is 0.5. Hence, only one optical element of the capturing system that has a poor MTF is sufficient to affect the aggregate MTF negatively.

Chapter 3

Overview of Optical Low-Pass Filters

Previously related works on optical low-pass filtering are reviewed in this chapter, and several different approaches will be summarized. The first part of the chapter will primarily focus on birefringent-based OLPF, which accounts for the majority of filters used in both video and still cameras. The second part of this chapter is dedicated to adjustable optical low-pass filters. The last section briefly discusses grating optical low-pass filters, a type of filters that are based on diffraction. The purpose of this chapter is to present the theory, practical implementations, and limitations of a range of OLPF solutions.

3.1 Birefringent-based OLPF

The basics of birefringent materials will be briefly considered. Pritchard [9] presents one of the first investigations of possibilities for using the birefringent plates for spatial low-pass filtering. In addition to this work, there is a significant body of papers (including many typical examples [10][11][12][13][14][15]) whose topics of study are the birefringent-based filters, their construction, and their performance. All of these prefilters are monochromatic; they treat all colors in the same way. In order to address modern sensor color patterns, Greivenkamp in [16] and [17] presents color-dependent birefringent prefilters.

A birefringent optical low-pass filter comprises an arrangement of at least two birefringent plates that might have different thicknesses. They are interleaved with quarter wave delay elements. Under certain conditions, a single unpolarized ray passing through a uniaxial birefringent plate splits into two orthogonal linearly polarized rays. Figure 3.1 shows a ray that is split within a piece of uniaxial birefringent material [2]. These two rays are known as ordinary and extraordinary rays, and each of them is governed by different refractive indices. The thickness of the birefringent plate and the difference between extraordinary and ordinary refractive indices determine the offset between the emerging rays. Many materials exhibit birefringence [18], but quartz and lithium niobate are preferred materials for making OLPFs in contemporary digital video and still cameras. In lithium niobate, the difference between extraordinary and ordinary refractive indices is more significant than in quartz. The required displacement between emerging rays would result in a thinner filter when made of lithium niobate than when made of quartz.
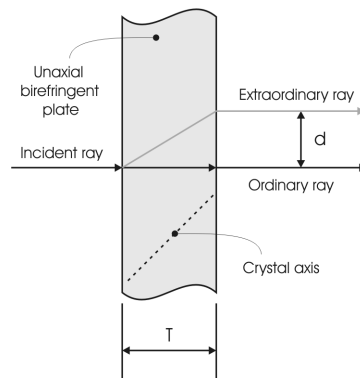
Figure 3.1: Under certain conditions, the incident ray splits into ordinary and extraordinary rays. The difference between refractive indices and the thickness of the plate determines offset **d** between emerging rays.

3.1.1 Two-plate birefringent OLPF

As its name indicates, this filter consists of two birefringent plates. This construction of birefringent OLPF is used in many still and video cameras with Bayer CFA, such as the

Canon Mark II, the Olympus E510, the Red One, and others. The crystal axis is oriented at approximately 45 degrees [18] relatively to the surface, which results in splitting an incoming ray into two linearly polarized rays on the opposite side of the first plate. In order to utilize the birefringence of the second plate, emerging rays from the first plate must be circularly polarized. A quarter-wave retarder is inserted between the first and second plates to carry out the linear-to-circular polarization. If the crystal axis of the second plate is oriented under some set angle (usually 90 degrees), relatively to the first plate, then the single ray, after passing through two successive plates with the retarder between them, splits into four output rays. The two-plate birefringent filter is also called a four-point separation filter. The optical axis of the retarder is oriented in such a way, relatively to the polarized light, that the intensity of each emerging ray is a quarter of the intensity of the incoming ray. The assembly is depicted in Figure 3.2.
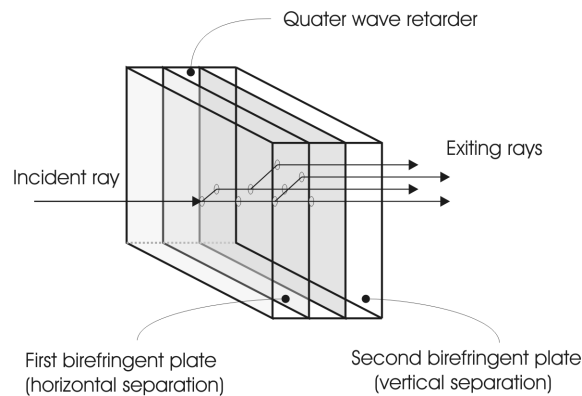
Figure 3.2: A single ray decomposition in a simple optical low-pass filter consisting of two plates with a retarder between them. The crystal axis of the second plate is rotated at 90 degrees relative to the crystal axis of the first plate.

As discussed earlier, the distance between output rays is a function of the thickness of the plates and the type of birefringent material. If the two plates shown in Figure 3.2 are of different thicknesses, then the resulting spatial impulse response appears as shown in Figure 3.3.
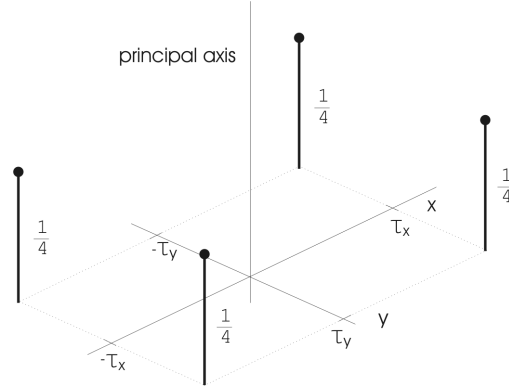
Figure 3.3: Spatial impulse response of a two-plate birefringent OLPF.

The spatial impulse response may be analytically written as:

$$f(x,y) = \frac{1}{4}\delta(x - \tau_x, y - \tau_y) + \frac{1}{4}\delta(x - \tau_x, y + \tau_y) +$$

$$\frac{1}{4}\delta(x + \tau_x, y - \tau_y) + \frac{1}{4}\delta(x + \tau_x, y + \tau_y)$$

Using two-dimensional Fourier transformation, this is the corresponding frequency response of the two-plate OLPF:

$$F(u,v) = \cos(2\pi u \tau_x)\cos(2\pi v \tau_y)$$

The result is a two-dimensional function whose absolute value is a modulation transfer function (MTF). It is graphically presented in Figure 3.4.
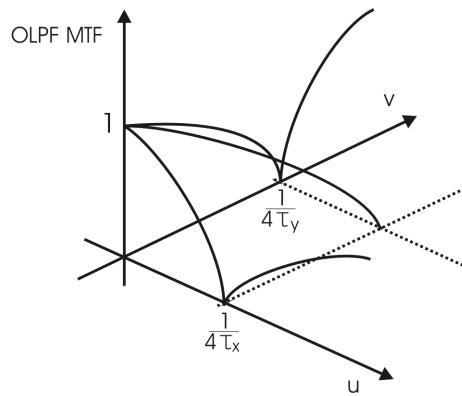
Figure 3.4: Modulation transfer function of an OLPF with two birefringent plates, arranged as shown in Figure 3.3.

25

Several important points should be noted here. First, from Figure 3.4 and the equation for filter's frequency response, it can be seen that the filter's zero-crossing is a function of the thickness of the plate and the type of birefringent material. Consequently, for a given birefringent material, varying the thickness of the plate changes the zero-crossing frequency. The second important point can be observed in the frequency response equation; it is a periodic function in which the period is equal to the inverse distance between emerging rays. Since it is a periodic function, it has non-zero values for even high frequency components. As a result, the two-plate OLPF is not a low-pass filter but rather a comb filter [19] whose frequency components below and above zero-crossing are passed with little or no alteration.
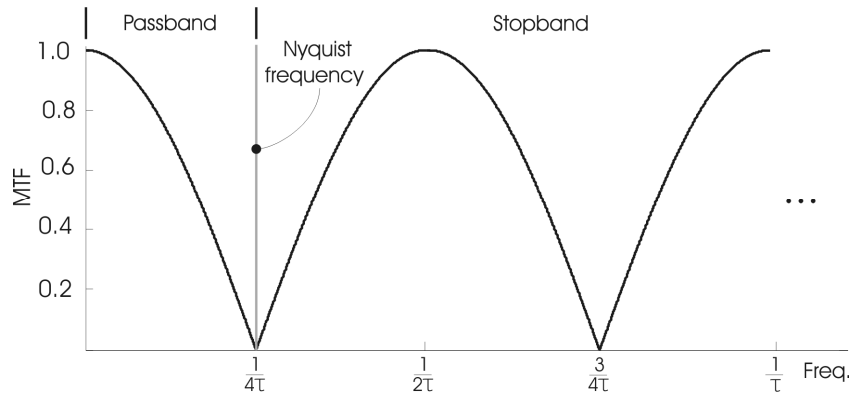
Figure 3.5: The vertical (horizontal) MTF of the two-plate OLPF with the first zero-crossing set at the Nyquist frequency of the imager. The frequency response is a periodic function; because of its features, it is closer to a comb filter [19] than a low-pass filter.

Assume that the zero-crossing of the OLPF is set at the Nyquist frequency of an imager. In addition, assume that the thicknesses of both plates are equal, which results in equally horizontal and vertical frequency responses. Figure 3.5 illustrates the vertical or horizontal modulation transfer functions of the OLPF. An ideal low-pass filter lets low-frequency components pass undisturbed but attenuates high-frequency components. As seen in Figure 3.5, the rolloff rate of the filter in the passband also attenuates frequencies below

26

the Nyquist frequency. This attenuation of passband frequencies will be perceived as a loss of image sharpness. Moreover, the frequency components in stopband that are not attenuated will fold back into the baseband signal and create aliasing. To reiterate an earlier statement, Figure 3.5 shows that the MTF of a two-plate OLPF is a periodic function in which the period is equal to the inverse distance between the emerging rays.

Example of a two-plate OLPF in Olympus E510

The Olympus E510 has Bayer pattern CFA with a 4.8μm distance between centers of photosites. When observed horizontally and vertically, the sensor has different sampling frequencies for red and blue samples than for green samples. Due to the specific spatial arrangement of green photodetectors, the horizontal Nyquist frequency of green samples is twice that of the red and blue samples.

Figure 3.6 shows actual and simulated results of a single ray of light passing through the OLPF from Olympus E510. The input ray is generated by light passing through a 1-μm pinhole. An optical microscope with 100x magnification and a digital camera were used to capture rays at the emerging side. The same figure also shows measured distances between output rays. When the distance in the frequency response equation is substituted for the two-plate OLPF with the measured value, the first zero-crossing is located at approximately 104 lp/mm. The Nyquist frequency for green samples coincides with the first zero-crossing of the OLPF.

Figure 3.7 shows only the horizontal MTF of the Olympus E510 OLPF because the vertical MTF is identical. As explained earlier, due to the specific arrangement of the Bayer CFA, the Nyquist frequency of red and blue samples is half the Nyquist frequency of green samples. It would be ideal to have separate OLPFs with appropriate zero-crossing frequencies for green and red/blue samples. Unfortunately, only one OLPF can be physically positioned in front of a sensor. If the OLPF is not color-dependent [16], then

both green and red/blue photodetectors will sample the same signal prefiltered by one OLPF. This situation results in a different amount of aliased signal for green image components than for red and blue ones. In other words, an OLPF designer can optimize an optical filter either for green samples or for red and blue ones, but not for both at the same time. In the case of the Olympus E510 digital still camera, the designers decided to match the filter's zero-crossing to the green Nyquist frequency, allowing more aliasing in red and blue image components.

(a)

(b)

(c)
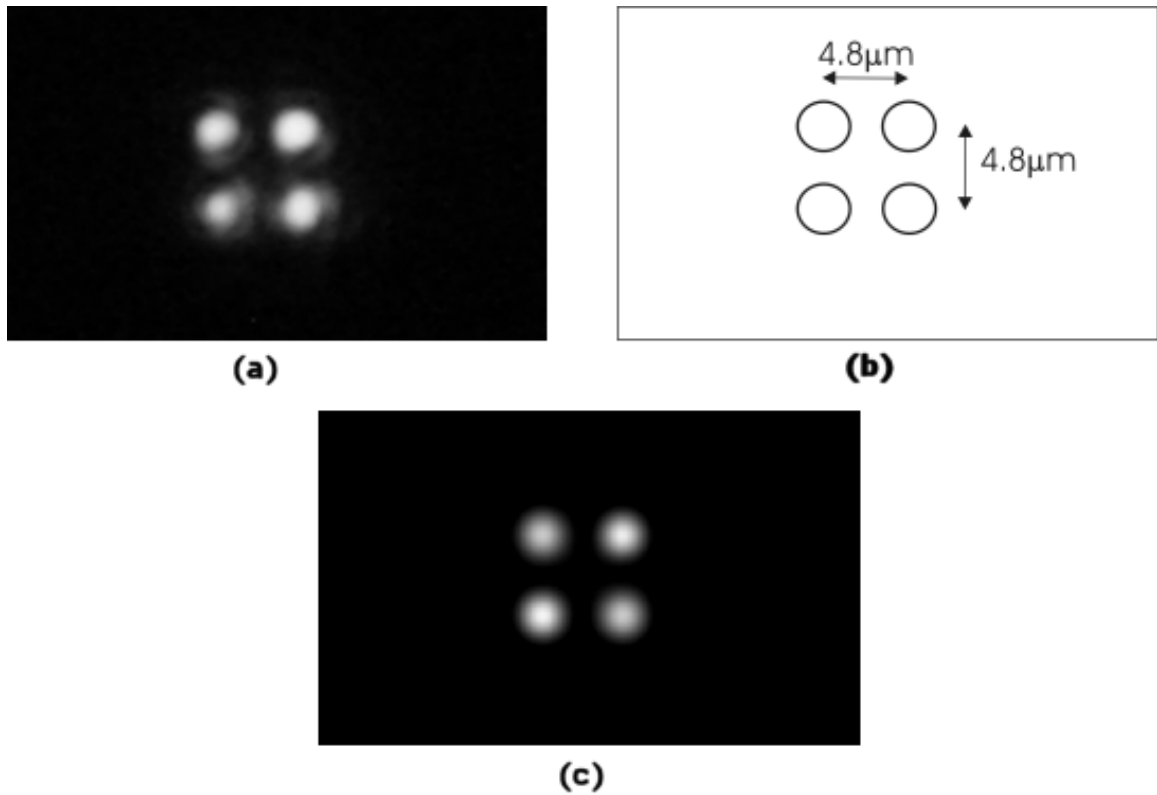
Figure 3.6: (a) 100x-magnified emerging rays when a single ray passes through the Olympus E510 OLPF. Measured distances between emerging rays are shown in (b). Code V simulated output of two-plate birefringent OLPF is shown in (c).
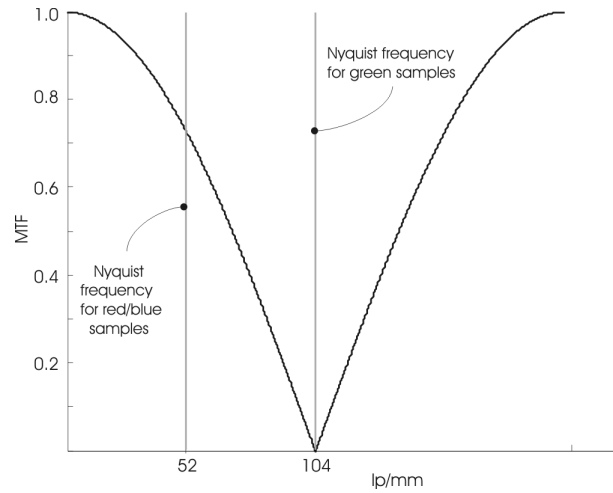
Figure 3.7: Horizontal MTF of the two-plate Olympus OLPF. The first zero-crossing coincides with the Nyquist frequency for green samples. The Nyquist frequency for red/blue samples is half the Nyquist frequency for the green samples.

3.1.2 Multiple birefringent plate OLPF

Example of a three-plate OLPF

One of the main disadvantages of OLPF, as examined thus far, is its poor performance for frequency components in stopband. Several forms of the three-plate birefringent filter are possible, differing in material and complexity of construction. One way to combine these forms is reported in [11]; this method results in a spatial impulse response, as shown in Figure 3.8.
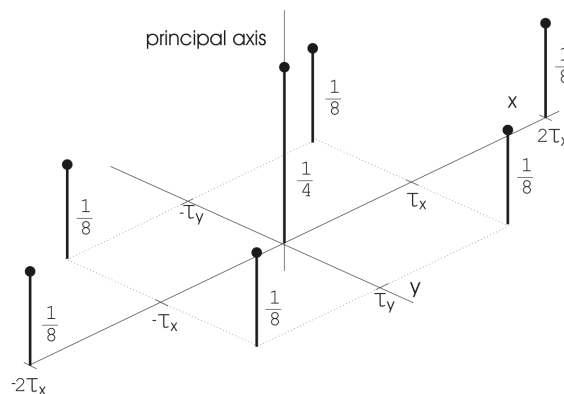
Figure 3.8: Spatial impulse response of the three-plate OLPF [11].

This can be achieved by adding one more plate, rotated at 45 degrees, to the assembly displayed in Figure 3.2. This birefringent OLPF has six output rays, with 1/8 of intensity of the input ray, and one ray, with 1/4 intensity, located in the center. Figure 3.9 illustrates Code V simulation of the same filter.

Figure 3.9: Code V simulation of the three-plate birefringent OLPF [11].

The impulse response derived from Figure 3.8 can be expressed analytically:

$$f(x,y) = \frac{1}{8}\delta(x - \tau_x, y - \tau_y) + \frac{1}{8}\delta(x - \tau_x, y + \tau_y) + \frac{1}{8}\delta(x + \tau_x, y - \tau_y) +$$
$$\frac{1}{8}\delta(x + \tau_x, y + \tau_y) + \frac{1}{8}\delta(x - 2\tau_x, y) + \frac{1}{8}\delta(x + 2\tau_x, y) + \frac{1}{4}\delta(x, y)$$

Using trigonometric identities and two-dimensional Fourier transformation, the frequency response of the three plates OLPF is a two-dimensional function:

$$F(u,v) = \cos\left(\frac{2\pi v \tau_y + 2\pi u \tau_x}{2}\right)\cos\left(\frac{2\pi v \tau_y - 2\pi u \tau_x}{2}\right)\cos(2\pi u \tau_x)$$

The horizontal and vertical MTF can be obtained by substituting zero for horizontal or vertical frequencies in the above equation:

$$F(u,0) = \cos^2(\pi u \tau_x)\cos(2\pi u \tau_x) \quad and \quad F(0,v) = \cos^2(\pi v \tau_y)$$

The horizontal MTF has two zero-crossings, which are a function of the plate thickness and the type of birefringent material. At the same time, the vertical MTF has only one zero-

crossing. If the first zero-crossing in the horizontal MTF is set at 40 lp/mm, then the second zero-crossing will be at twice that frequency, or 80 lp/mm. MTF is a periodic function with a period of 160 lp/mm. Comparing the MTF of a two-plate OLPF with the MTF of a three-plate OLPF reveals that the latter attenuates stopband frequency components more successfully. A graphical representation of both horizontal and vertical MTF is shown in Figure 3.10.
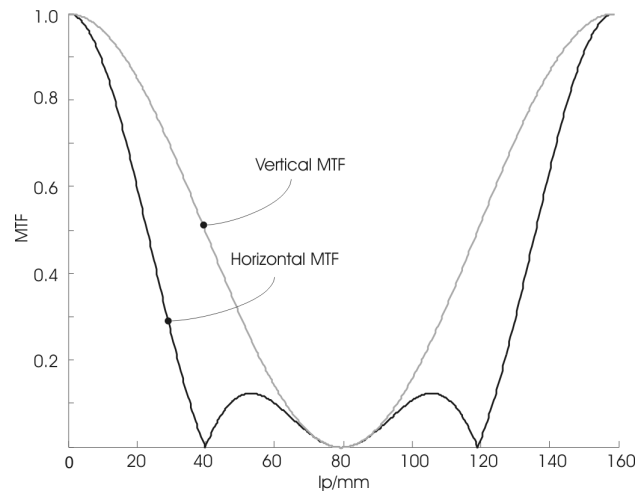
Figure 3.10: The horizontal and vertical MTF of the three-plate OLPF.

Example of a four-plate OLPF

The Sony F900 video camera is based on three 2/3-inch CCDs [20]. Each color is captured by a separate sensor with square $5\mu m$ x $5\mu m$ photosites. The distance between the centers of the photosites determines the Nyquist frequency at 100 lp/mm for each color component. Figure 3.11 shows the actual and simulated results of a single ray of light passing through the OLPF from F900. The same figure also shows the measured distances between emerging rays.

Figure 3.12 illustrates the two-dimensional impulse response of the filter. The four centered impulses are twice as large in amplitude than peripheral impulses. Observed along both diagonals, the output responses form a triangular impulse response.
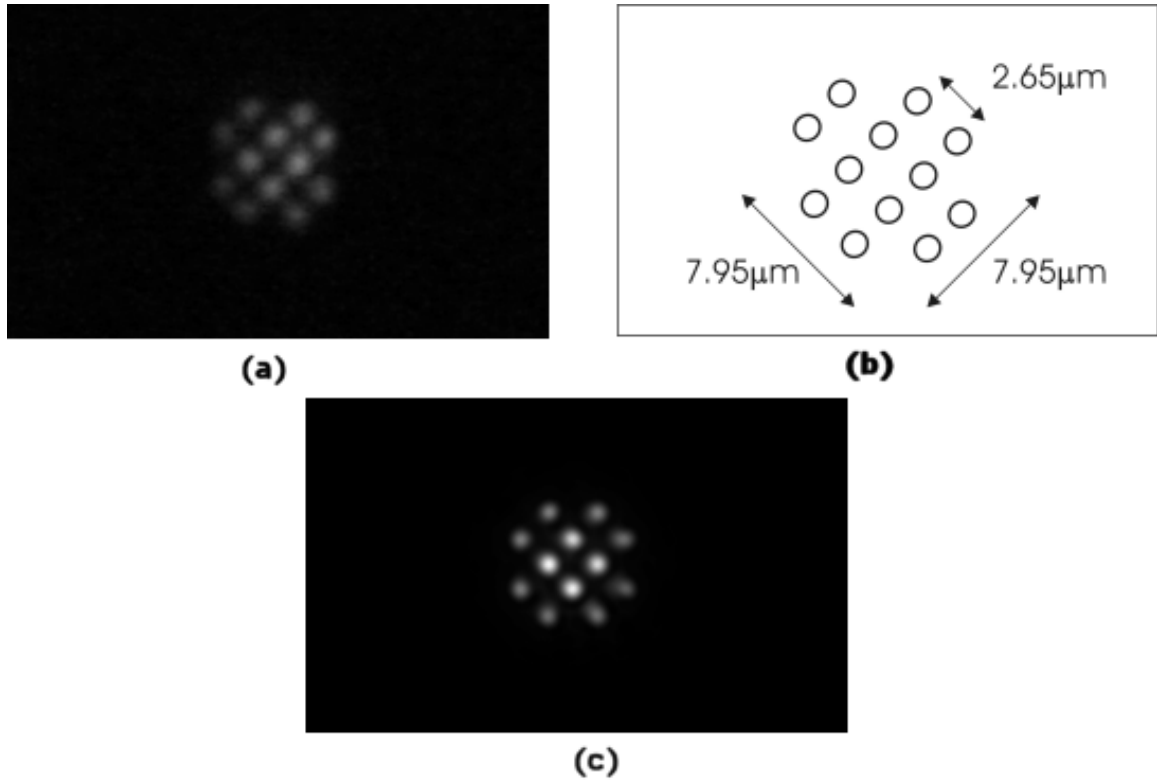
Figure 3.11: (a) 100x-magnified emerging rays when a single ray passes through the F900 OLPF. The measured distances between emerging rays are shown in (b). The Code V simulated output of the four-plate birefringent OLPF is shown in (c).

The impulse response of the filter is symmetric; as a result, the vertical and horizontal MTFs are identical. This is expected in a design where the photosites are square and, hence, where the vertical and horizontal distances between samples are identical. This is a nonseparable filter; finding a close-form equation for MTF is not trivial. The MTF of the filter was found using the fast Fourier transform (FFT). Figure 3.13 shows the diagonal and horizontal modulation transfer functions. The figure reveals that the diagonal MTF has a lower zero-crossing frequency and a different shape than the horizontal MTF.
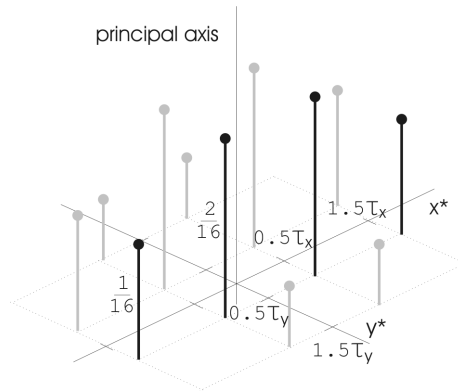
Figure 3.12: The spatial impulse response of a four-plate birefringent OLPF. The axes are positioned at the diagonals of the filter.
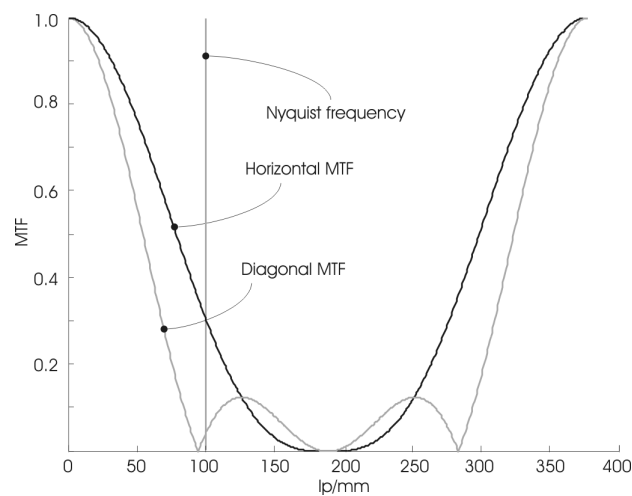
Figure 3.13: Horizontal and diagonal MTF of OLPF from Figure 3.12. Horizontal Nyquist frequency is also shown for reference.

Example of a five-plate OLPF

The sensor in a Genesis digital film camera is based on a single sensor that has a stripe-patterned CFA. The distance between the centers of same-color photosites is 12.3μm. This corresponds to a sampling frequency of 80 photosites/mm, which results in a horizontal Nyquist frequency of 40 lp/mm. Each photosite is a 12.3μm x 4.1μm rectangular shape. Observed in both horizontal and vertical directions, the number of red, green, and blue photodetectors are identical, which results in an equal frequency response of all three

33

color components. Due to the rectangular shapes of the photosites, the vertical footprint response is different from the horizontal response.

Figure 3.10 shows the actual and simulated results of a single ray of light passing through the OLPF from Genesis camera. The single-incident ray splits into 20 emerging rays. The rays' spatial distribution, with measured distances, is shown in Figure 3.14.

(a)   (b)

(c)
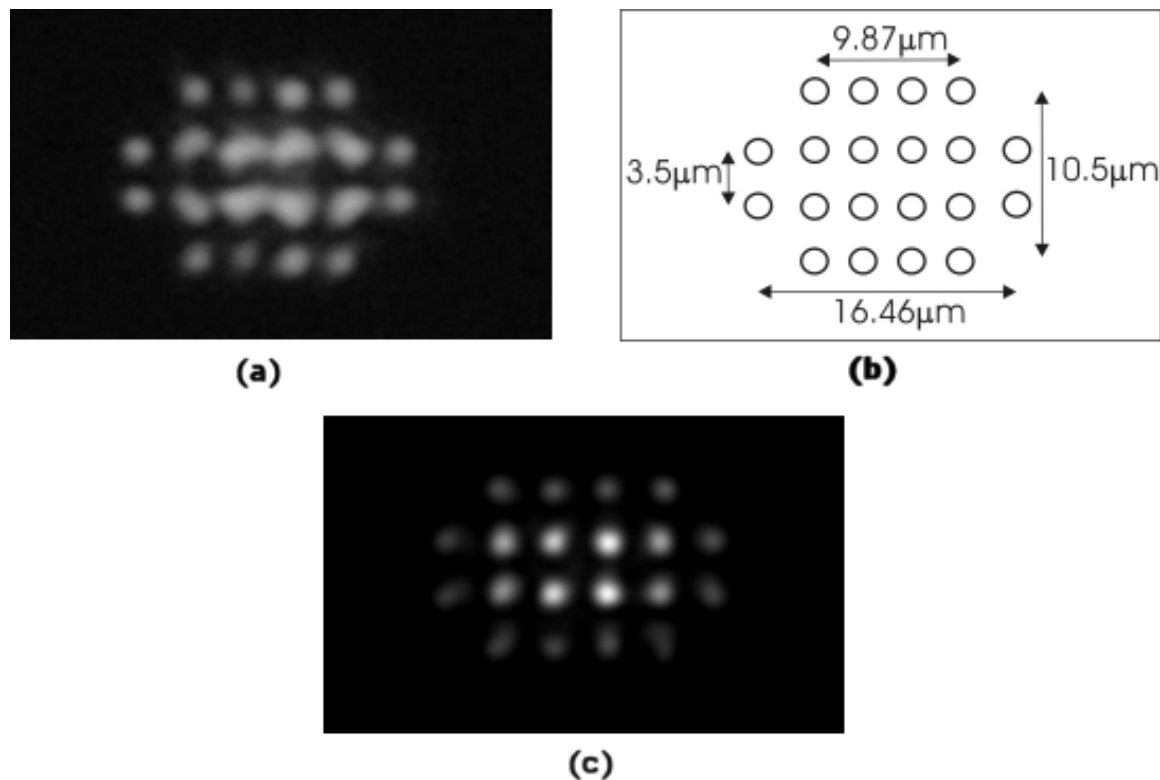
Figure 3.14: (a) 100x-magnified emerging rays when a single ray passes through the OLPF. Measured distances between emerging rays are shown in (b). Code V simulated output of a five-plate birefringent OLPF is shown in (c).

Figure 3.15 shows the two-dimensional impulse response, along with the accompanying amplitudes of the Genesis OLPF. As seen in the figure, along the x and y axes, the impulse responses are different; however, both of them form a triangular shape. The Genesis OLPF is a nonseparable filter, and since a closed-form MTF equation was not easily

34

accessible, the response was found using FFT. Horizontal and vertical MTFs are shown in

Figure 3.16.
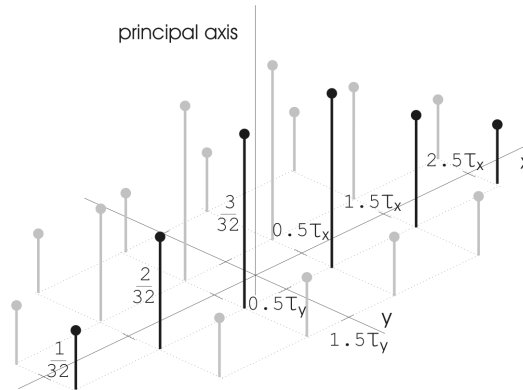
Figure 3.15: The spatial distribution of output rays, which is the result of a single ray passing through the Genesis OLPF. The impulse response along the x axis is highlighted in black.
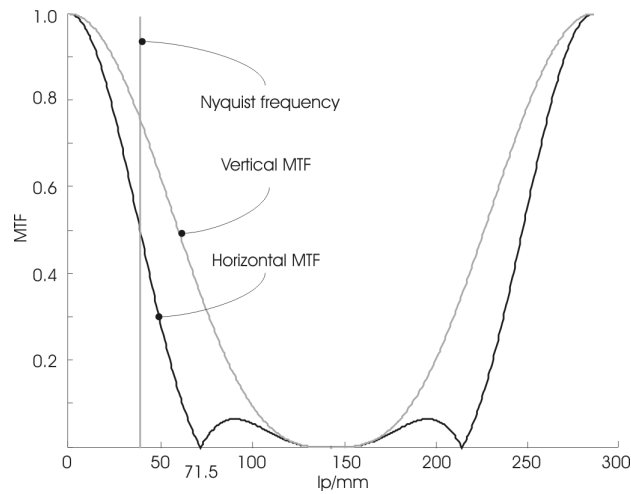
Figure 3.16: The horizontal and vertical MTF of Genesis OLPF. The Nyquist frequency of the Genesis sensor is also added for reference.

A comparison of the modulation transfer function of the Genesis OLPF, from Figure 3.16,

with the response of the Olympus OLPF, from Figure 3.7, demonstrates that the sidelobes

in the response of the Genesis OLPF are lower than that of the Olympus OLPF. This implies

that the frequency components above the Nyquist frequency will be more attenuated,

which may result in less aliasing after the image is digitized. When all other variables are equal, smaller filter sidelobes result in lower aliasing.

The vertical OLPF response has greater bandwidth than the horizontal OLPF response. Due to the rectangular shapes of the photosites, the horizontal photodetector response has greater bandwidth than the vertical response, and, consequently, it must be more limited in order to prevent aliasing.

3.1.3 Birefringent OLPF - Conclusion

As explained by the preceding material, designers have been using two or more birefringent plates to create spatial, two-dimensional OLPFs. In their basic form, birefringent OLPFs are simple, reliable, and relatively inexpensive, but they also possess a few drawbacks. Due to these filters' rolloff rates, camera designers must either under-correct, to maintain passband resolution and to allow some aliasing, or they must eliminate aliases with a more aggressive design that will also alter image information. Adding birefringent plates may improve MTF in the stopband region, to some extent.

In addition, most OLPFs are designed as passive optical elements with fixed frequency characteristics, and they do not adjust even if other parts of the capturing systems are changed.

3.2 Adjustable Optical Low-Pass Filters

One of the drawbacks of the birefringent OLPF is that it has fixed frequency characteristics. Several different attempts have been conducted to address this problem, and their summaries follow.

Pritchard [9] proposes using two birefringent filters, as described above, positioned in a sequence in the light path. Their rotations at different angular relationships, relatively to a

pickup device, produced a continuously adjustable frequency response of the OLPF. Authors in [21] propose various mechanical methods for rotating one of the birefringent plates, which would result in varying the distance between the emerging rays and varying the modulation transfer function of the filter.

Nishioka et al. [22] uses an optical low-pass filter comprised of liquid crystal. Liquid crystal has the ability to change the direction of the crystal axis when exposed to an electric field. This possibility allows control of the birefringent index, as requested; consequently, the ability to control the filter is enabled or disabled. The author also suggests the possibility of variably controlling the crystal axis and therefore controlling the frequency response during the observation of the image.

Authors in [23] present the idea of using a plurality of optical low-pass filters with different optical characteristics mounted on a wheel, which is externally controlled to set an appropriate filter in the light path.

Kreymerman in [24], proposes using a thin pellicle (i.e. 2μm), positioned in the path of light. Light bounces off the pellicle onto a pickup device. The author recommends using this apparatus in two possible ways. If a camera consists of color and luminance image sensors, then portions of the light rays pass undisturbed through the semitransparent pellicle onto the luminance sensor, while the other portions reflect from it onto the color sensor. If a camera consists of one sensor with CFA, then all light energy reflects from the pellicle onto the sensor. Alternating current is applied to piezo-ceramic stripes, which are attached to the pellicle, thereby forcing it to vibrate. The pellicle distortion affects the reflected light, thereby also affecting its higher-frequency components.

Although this is a very elegant approach, this solution may have several potential problems. The flange focal distance in the camera varies from manufacturer to manufacturer, ranging from a few millimeters to several dozens of millimeters. The

apparatus requires positioning a lens at 90 degrees relatively to the sensor, and it requires inserting the pellicle between. That can be challenging, if not impossible, for compact cameras. Bigger optical sensors require bigger pellicles to prevent obscuring the light bundle, which may cause a problem of uniformity of spatial distortion of the pellicle. If the pellicle has a nonuniformly distorted surface, then the captured image will be nonuniformly filtered. The author reported that the resulting OLPF MTF, with a certain voltage level, is a constant for lower frequencies (i.e., a flattop filter). However, that is physically impossible, as will be explained in the following chapter.

3.3 Diffraction-Based OLPF

The earliest proposal to use a diffraction grating as a low-pass filter in a video camera can be found in [25]. The authors proposed using phase elements provided on a transparent base plate to produce a blur in the images formed by the optical system. The principle behind the grating low-pass filter (GOLF) has been well-known for decades; a fine description can be found in [18], and it will be briefly presented in the following text. Figure 3.17 shows a transmission phase grating, which was made by ruling or scratching parallel notches onto the surface of a flat, clear glass plate.
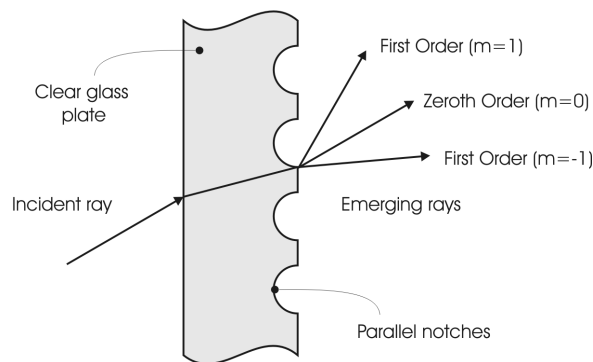
Figure 3.17: A transmission phase grating used as an optical low-pass filter.

Due to the grating, emerging light radiates with different phases over the grating surface and forms various principal maxima, whose positions can be found using the grating equation [18]. By controlling the density, orientation, and shape of the grating, it is possible to control the intensity distribution of the emerging light and therefore to control the frequency response of the GOLF.

There is a significant body of work, with some examples found in [26][27] [28][29][30][31][32] and [33], whose topics of study are the diffraction-based optical low-pass filters. The authors of these papers reported various shapes, orientations, and densities of grating used in GOLF. More recently, in [34], the authors presented comparisons between GOLF-based OLPF and birefringent-based OLPF.

It is important to note one of the most significant differences between GOLF and birefringent-based OLPF, as seen in Figures 3.2 and 3.17. In the case of a birefringent OLPF, emerging rays are parallel to each other. On the other hand, in a GOLF-type filter, emerging rays diverge from each other. This requires a precise positioning of the grating-based filters relatively to the pickup device, since the distance between the filter and the sensor will determine the system's frequency response. In the birefringent-based filters, emerging rays are parallel; hence, precise positioning of the filter is not required. As another drawback of GOLF, the position of a local maximum of scattered light is a function of the wavelength of incident light, which makes the modulation transfer function a function of wavelength.

Chapter 4

Dynamic Optical Low-Pass Filter

To address the deficiencies of the classic birefringent and diffraction-based OLPFs, specifically their stopband performances and fixed frequency responses, a dynamic optical low-pass filter (DOLPF) is proposed. The underlying principle of the DOLPF and some practical aspects of it are presented in the first half of this chapter. The second half of the chapter is dedicated to the theoretical analysis, design, and evaluation of the filters that are intended for implementation in the DOLPF.

4.1 Introduction

In this chapter, we propose the use of a parallel optical window or, alternatively, a rigid mirror positioned between the lens and the imager as a dynamically controlled optical low-pass filter. Simplified illustrations of the two proposed solutions are shown in Figure 4.1 and Figure 4.2. As seen in the figures, the DOLPF consists of either an optical window or a rigid mirror that has two rotational degrees of freedom: pitch and yaw. The underlying ideas for both solutions are the same, but the following study will focus on the former solution, the optical window. Due to the space constraints between the lens and the imager in a camera, that solution is easier to implement. Nevertheless, all conclusions drawn from the window implementation are relevant to the mirror solution, although with minor differences. The DOLPF utilizes the fact that image capturing is not an

instantaneous process and that in order to collect enough photons, the imager must be exposed to light for some finite amount of time. The mirror and the optical window move during the exposure. Therefore, the reflected ray (in the case of the mirror solution) and the emerging ray (in the case of the optical window) each strike more than one spot on the imager.
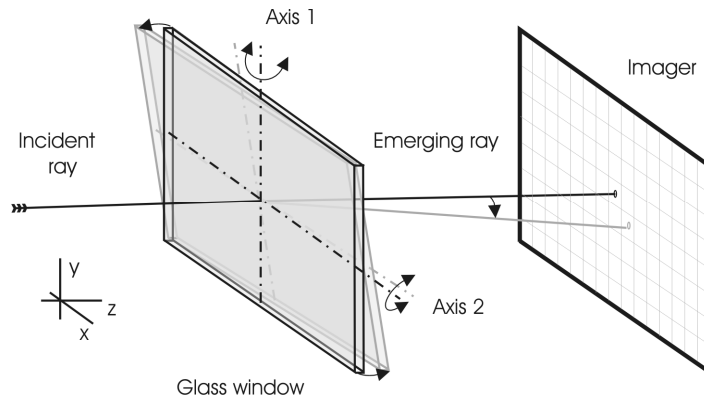
Figure 4.1: The DOLPF, based on a parallel optical window with two rotational degrees of freedom. The coordinate system is also indicated.
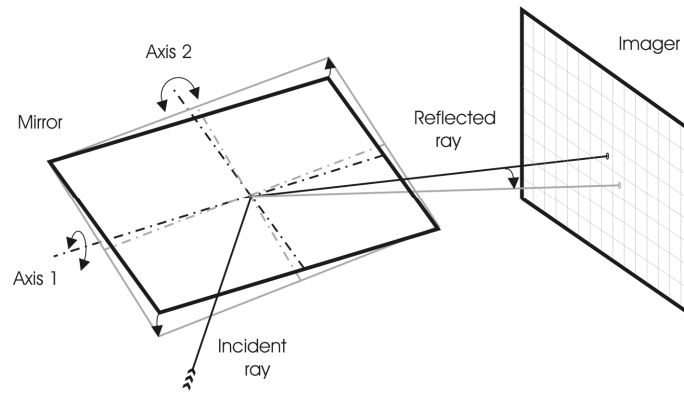
Figure 4.2: An alternative proposal for the dynamically controlled OLPF, based on the rigid mirror.

Since the window and mirror rotation directly manipulate the resulting point spread function of the system, their motions must be carefully controlled. Manipulating the point spread function of the optics before the image is digitized alters the frequency

components of the imaged continuous scenes. The effects of different paths and velocities onto the point spread function are analyzed later in the chapter.

4.2 Principle of Operation

The principal idea that enables the window-based DOLPF is the phenomenon of the lateral displacement of the emergent ray when the incident ray is not perpendicular to the window. When a parallel optical window with a thickness T and a refraction index n is tilted in the optical path, then the ray incident at an angle α is displaced laterally by amount δ, given by [35]:

$$\delta = \frac{T\sin(\alpha)\left(1 - \sqrt{1 - \sin^2(\alpha)}\right)}{\sqrt{n^2 - \sin^2(\alpha)}}$$

Figure 4.3 shows a top view of the DOLPF in two different positions when it rotates in the XZ plane. When the window is in a neutral position (position A), the incident ray is perpendicular to the surface of the window. Position B marks the location of the window when it is rotated at angle α, relatively to the neutral position.
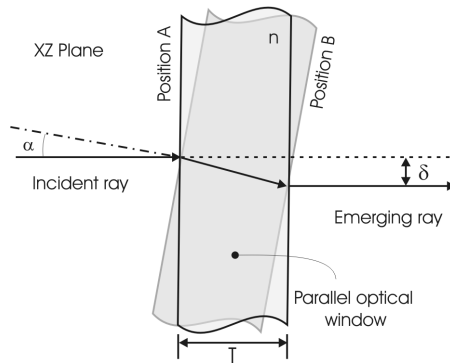
Figure 4.3: A ray incident to a parallel optical window, tilted in the optical path, is laterally displaced after emerging on the opposite side.

The rotation around the Y axis results in a displacement in the XZ plane. Furthermore, when the window rotates around the X axis, the ray displacement occurs in the YZ plane.

By enabling the window to rotate in both XZ and YZ planes, the incident ray can be laterally moved in two dimensions across the imager.

The parallel displacement of rays is used, for example, in the ophthalometer, an instrument for measuring the distance between points that cannot be measured directly [35]. This technique is also used in other fields; for example, it is used for image registration in scanners [36] and in cameras for image motion compensation [37].
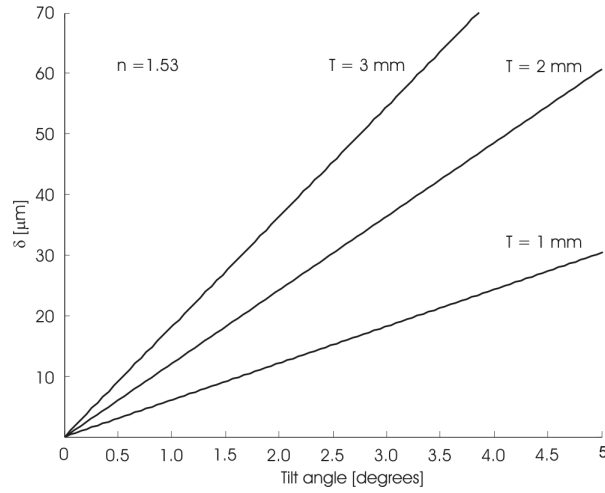
Figure 4.4: A lateral displacement of the emergent ray as a function of the window tilt angle and its thickness as a parameter.

For a given refractive index, Figure 4.4 shows the lateral displacement of the emergent ray as a function of the window tilt angle and its thickness as a parameter. As seen in the figure, for a small tilt angle, the lateral displacement is a linear function. To put the values from the figure in perspective, the lateral displacement should be similar in size to the imager photosites, which range from a few micrometers up to a few dozens of micrometers in imagers for special applications.

It is worth noting that in the window-based DOLPF, the emergent ray is parallel to the incident ray. Parallel emerging rays imply that the lateral displacement of rays, when they reach the imager, is not a function of the distance between the DOLPF and the imager. Consequently, a precise positioning of the window-based DOLPF between the lens and the

43

imager is not required. This is not the case in the mirror-based DOLPF, where the relative position of the mirror to the imager determines the ray deflection.

4.2.1 Optical Simulation

As part of the DOLPF design process, a study was undertaken to estimate the adverse effects caused by the window inserted between the imager and the lens. For that purpose, two optical simulation packages were used: 'Code V' from Optical Research Associates [38] and 'Zemax' from Zemax Development Corporation [39]. In this section, only the conclusion of the study is presented. The details of the optical simulation are presented in Appendix A. The parallel optical window used in the optical simulation is the same as the window used in the experiments.

The window inserted between the lens and the imager causes two noteworthy adverse effects. First, due to the longitudinal displacement of the image, the imager must be moved from its original position for approximately 0.625 mm. A similar problem is present with the birefringent OLPF, and it is normally addressed during the camera design.

The second and more significant adverse effect is illustrated in the figures showing Optical Path Difference (OPD) curves. The most affected OPD curves are those for the field angles that cover the corners of the imager. From those curves, it can be seen that for both non-tilted and tilted windows, the peak-to-valley OPD is greater than 1/4 of the reference wavelength. Furthermore, for all wavelengths, the blue light at 486nm is affected more than the other spectral frequencies. This is also reflected in the RMS OPD and MTF curves. Two observations are worth noting here. First, the Nyquist frequency of the imager used in the experiments is 67 lp/mm. The higher image frequency components will alias after sampling, so this frequency may be considered to be the limiting frequency of the system. Relatively to the reference system, the MTF at that frequency is affected less than 10%

when the window is maximally tilted. In the non-tilted window case, degradation at the same frequency is less than 5%. It can be argued that this degradation at the limiting frequency is acceptable, considering that we are building an optical low-pass filter.

Second, Code V and other software packages are not intended to evaluate a time varying system such as the DOLPF. In our situation, the window will stay in simulated positions for only a fraction of the exposure time. This may grant some insight into the system's behavior when the window is at certain positions, but our final setup is more complex.

4.2.2 Practical Considerations

Several factors must be considered in the practical implementation of the DOLPF. Some of those considerations are discussed here. Minimal physical dimensions of the parallel optical window are limited by the optical dimensions of the imager. The window inserted in the optical path should not obstruct the light bundle between the lens and the imager. Sensor formats are not standardized, but typical diagonal dimensions range from 2.3 mm to 43.27 mm [40]. The camera used in our experiments is based on a one-inch sensor whose diagonal is 16.0 mm. For the experiments, a square optical window with dimensions 25 mm x 25 mm proved to be large enough to avoid any image vignetting.

The required lateral displacement is determined by the frequency response of the optical low-pass filter that we aim to create. As shown in the examples with the birefringent OLPF, the ray lateral displacement is tailored based on the dimensions of the imager photosite. For example, considering the case of the two-plate birefringent OLPF designed for the Bayer CFA imager, which has square 4.8 μm x 4.8 μm photosites, the lateral displacement is 4.8 μm in both horizontal and vertical directions. In our experiments, for the purpose of presenting our ideas clearly, we designed filters that have their first zero-

crossings at 30 lp/mm. To be equivalent to the two-plate birefringent OLPF, the DOLPF filter requires a lateral displacement of 16.6 μm.

The thickness of the parallel optical window determines the lateral displacement and the weight of the window. Thicker glass results in more lateral displacement but also leads to increased total weight. A heavier window requires more force applied in order to achieve the necessary angular acceleration and velocity. For our experiments, we use a 2 mm thick optical window that has 2.55 g/cm^3 density. This results in a window weight of 3.19 g. For that thickness, every 1° of the window rotation results in 12 μm of lateral displacement.

The mirror and the optical window move during the exposure, and the path that the ray should trace on the imager surface must be finished before the exposure ends.

4.3 Designing Filter Shape

This section studies the design of the spatial filters used in the DOLPF and focuses on their shape. OLPFs are analog domain devices; their functionality is applied on a continuous signal before discretization. However, as seen with the birefringent-based OLPFs, their spatial impulse responses can fully be described using discrete-space signals, and they can be treated using discrete signal processing.

During the imager exposure, the optical window or mirror rotates around one or both axes and, as a consequence, results in a two-dimensional lateral displacement of the image. In our implementation, these optical elements move in discrete steps, which results in a finite number of image lateral displacements during the exposure. If the time that the optical elements spend traveling from one position to another is negligible in comparison to the exposure time, then the output of the imager is the integration of several spatially displaced images. Figure 4.5 illustrates an example when the window moves three times

during the exposure, resulting in a lateral move of the projected image on the imager. After the image exposure is over, all three image positions are accumulated in the final image.

It is important to note that the positions of laterally shifted continuous images on the imager are independent from the sampling structure of the imager. These positions on the imager are a function of the continuous angle at which the optical window travels around the axes. The lateral displacements of the image also determine the spatial position of impulses in the two-dimensional impulse response of the filter.
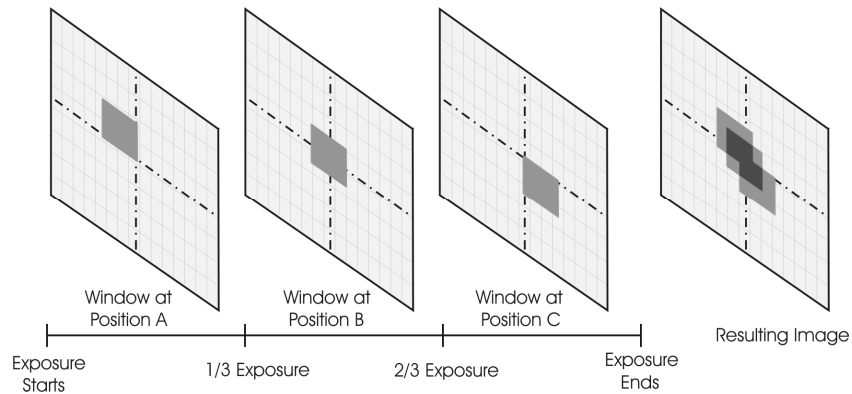
Figure 4.5: An illustration of the window moving in three discrete steps during the exposure. Only the imager is shown. The darker gray square represents the object projected onto the imager. The lateral move is exaggerated; in reality, it is less than the dimensions of the photosite.

While the angular positions of the window determine the spatial distribution of the impulses in the filter's impulse response, the amplitude of these impulses is determined by the time that the optical element spends on each discrete position.

The same tools from the discrete signal processing that are used to analyze the birefringent OLPF are used in the DOLPF analysis as well. Also, the physical limitations of the DOLPF impose certain constraints on the filter design and must be taken into account.

47

Two strategies are used in the DOLPF filter development. The first strategy is a classic approach where a filter is designed independently from the other elements of the optical system. Filters are designed to maximize the passband frequencies while minimizing the stopband frequency components. If it exists, the first zero-crossing of the filter frequency response will be considered as a border between the passband and the stopband of the filter. The second approach in the filter design attempts to exploit the frequency characteristics of other elements of the optical system, specifically the inherent low-pass characteristic of the lens. The DOLPF filter coefficients are designed in combination with the lens—whose frequency response varies with the F-number—while using a predetermined amount of energy in the stopband as a criterion.

4.3.1 Standard approach

The previous section stated that the impulse amplitudes in the two-dimensional impulse response are directly proportional to the time that the window spends on each discrete position. A reexamination of both Chapter 3 and the impulse response of the birefringent OLPF reveals that the envelope of the impulse response forms either a rectangular or a triangular window function. In harmonic analysis, a window function is applied to the truncated signal in order to minimize the effects of spectral leakage. In the DOLPF filter design process, a similar problem is encountered: we want to minimize the stopband frequency but also to minimize the alteration of the passband frequencies' components. In addition to harmonic analysis, applications of window functions include filter design [6] and beamforming [41].

A comparison graph of several windows frequently used in harmonic analysis is shown in Figure 4.6. The distance between window taps is carefully chosen so that the first zero-crossing of the frequency response is exactly at 30 lp/mm. The same zero-crossing

facilitates comparisons between the characteristics of the frequency responses for several typical window functions. The first four analyzed window functions are considered to be the classic windows: rectangle, triangle, Hanning, and Blackman-Harris. The other two are constructed windows: Tukey and Gaussian [42]. If a window frequency response (i.e., the Gaussian window function) does not have a zero-crossing, then the frequency where the magnitude reaches -60 dB is considered a zero-crossing frequency.
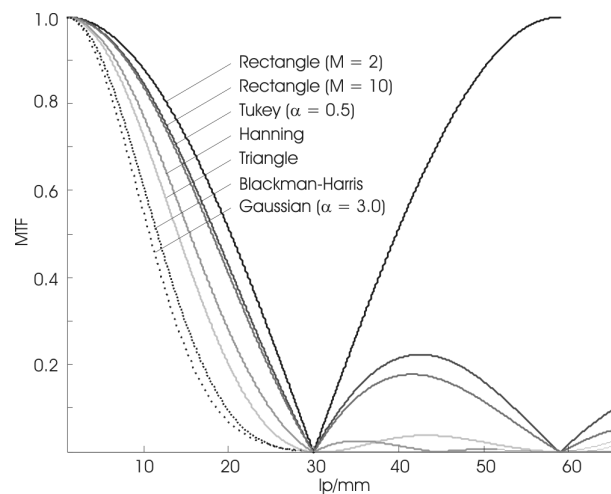
Figure 4.6: Theoretical frequency response of window functions typically used in harmonic analysis. The distance between window taps is chosen so that the first zero-crossing is at 30 lp/mm.

Table 4.1 lists specific performance parameters of the examined window functions: highest side-lobe, 6 dB bandwidth, passband area, and stopband area.

The highest side lobe parameter is defined as the peak level of the highest side lobe, relative to the peak level of the main lobe. The table column named "6 dB bandwidth" presents the frequencies where the window frequency response reaches -6 dB, or 50% of the response at DC. The passband area represents a normalized surface under the frequency response graph for the passband frequency components. For reference, an ideal low-pass filter with a zero-crossing at 30 lp/mm has a passband area of 1. The stopband area represents a normalized surface under the frequency response graph for the

49

stopband frequency components. For an ideal low-pass filter, the surface under the

stopband frequencies is 0.

Window	Highest side-lobe level (dB)	6 dB BW (lp/mm)	Pass-band area	Stop-band area
Rectangle (M=2)	0	20.00	0.6449	0.6288
Rectangle (M=10)	-13	18.12	0.5984	0.1558
Triangle	-27	13.60	0.4706	0.0198
Tukey (α=0.5)	-15	17.72	0.5881	0.1184
Hanning	-32	15.04	0.5158	0.0102
Gaussian (α=3.0)	-55	10.12	0.3670	0.0037
Blackman-Harris	-67	11.11	0.3954	0.0012

Table 4.1: A comparison of the window functions used in the analysis. The passband area represents a normalized surface under the frequency response graph in the passband region. An ideal low-pass filter measures 1 for the passband area parameter. The stopband area represents a normalized surface under the frequency response graph in the stopband region.

As seen in Figure 4.6 and Table 4.1, a window function that performs poorly in the

stopband region behaves better in the passband region. The opposite is also true; a

window function that performs well in the stopband region behaves poorly in the passband

region. For example, the Gaussian window effectively attenuates the stopband frequency

components, but it is only half the bandwidth of the rectangle filter. An attempt to find the

answer for such a behavior will be discussed in the following text.

Analyzing filters' frequency responses using the z-transform

The z-transform is used to discover how the selection of the window function coefficients

affects the frequency response. For better understanding, the following analysis is only

aimed at one-dimensional spatial filters, although the same analysis could be extended to

the separable two-dimensional spatial filters. Linear space-invariant filters, with input

signal x[n] and output y[n], satisfy a linear constant-coefficient difference equation:

$$\sum_{k=0}^{N} a_k y[n-k] = \sum_{k=0}^{M} b_k x[n-k]$$

In the case of the OLPF, additional constraints to the system function are enforced by the physical limitations of the optical system. The first constraint is that OLPFs cannot form an infinite impulse response filter. They can only create finite impulse response spatial filters (FIR), which means that all a_k coefficients except a_0 are zeros. When $a_0 = 1$, the above equation can then be rewritten in this way:

$$y[n] = \sum_{k=0}^{M} b_k x[n-k]$$

If the z-transform is applied to both sides of the above equations, this is the result:

$$Y(z) = \sum_{k=0}^{M} b_k z^{-k} X(z)$$

The system function then has the following form when rearranged in terms of zeros c_k:

$$H(z) = \frac{Y(z)}{X(z)} = \sum_{k=0}^{M} b_k z^{-k} = b_0 \prod_{k=1}^{M} \left(1 - c_k z^{-1}\right)$$

Due to physical limitations, OLPFs cannot subtract or amplify light, which adds two additional constraints onto the filters' coefficients. These constraints can be expressed by these equations:

$$\sum_{k=0}^{M} b_k = 1 \quad and \quad b_k \geq 0 \ for \ \forall k$$

The first constraint is based on the assumption that the total light energy that enters the OLPF is equal to the energy that exits the OLPF. This is an acceptable assumption since the energy loss is negligible when light is passing through the optical window.

The resulting system function is an Mth-degree polynomial, which has M roots in the complex numbers. The following examples illustrate the z-transform applied to OLPF filters.

Example 1: Suppose that the impulse response for the two-tap rectangle OLPF can be expressed this way:

$$y[n] = b_0 x[n] + b_1 x[n-1],$$

where $b_0 = b_1 = 1/2$. This, then, is the system function:

$$H(z) = \frac{1}{2}\left(1 + z^{-1}\right) = \frac{1}{2}\left(1 - (-1)z^{-1}\right)$$

Note that the system function is a first-order polynomial with positive coefficients. The positions of the zeros and poles of the system function are shown in Figure 4.7.

Example 2: Suppose this is the impulse response for the three-tap rectangle OLPF:

$$y[n] = b_0 x[n] + b_1 x[n-1] + b_2 x[n-2],$$

where $b_0 = b_1 = b_2 = 1/3$. This, then, is the system function:

$$H(z) = \frac{1}{3}\left(1 + z^{-1} + z^{-2}\right)$$

The system function is a second-order polynomial with positive coefficients. This polynomial has two complex zeros:

$$z_1 = -\frac{1}{2} + j\frac{\sqrt{3}}{2}, z_1 = -\frac{1}{2} - j\frac{\sqrt{3}}{2}$$

It also has two poles in the origin. The constellation of zeros and poles for the three-tap rectangle filter is shown in Figure 4.7.

Example 3: Suppose this is the system function for the ten-tap Hann filter:

$$Y(z) = \sum_{k=0}^{9} b_k z^{-k} X(z),$$

where b_k = {0.0144, 0.0531, 0.1038, 0.1504, 0.1781, 0.1781, 0.1504, 0.1038, 0.0531, 0.0144}. The system function is a ninth-order polynomial with positive coefficients; it has

9 zeros located on the unit circle and 10 poles located in the origin, as shown in Figure 4.8.
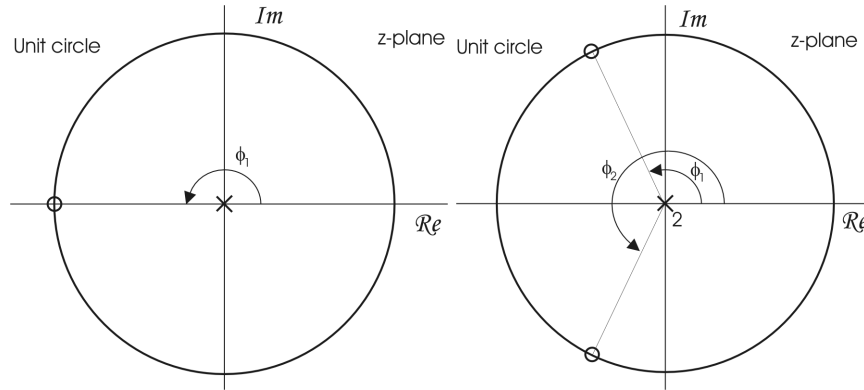
Figure 4.7: The pole-zero plot of the two-tap rectangle filter is shown on the left. One real zero is located at -1, and one real pole is located in the origin. The pole-zero plot of the three-tap rectangle filter is shown on the right. The three-tap filter has two complex-conjugate zeros located on the unit circle.
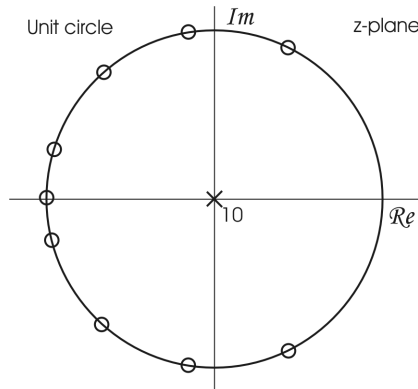
Figure 4.8: The pole-zero plot for the 10-tap Hann window. The system function is a ninth-order polynomial, which results in 9 zeros located on the unit circle.

The interpretation of zero-plane plots offers an insight into the way the location of zeros and poles affects the frequency response magnitude. In general, it is hard to determine the position of a polynomial's zeros based on its coefficients; however, several algebraic rules predict their general positions in the z-plane [43]. As determined earlier, the coefficients of a polynomial representing a DOLPF filter must be real and positive. When the coefficients of the polynomial are real, then complex-valued roots must occur in

complex-conjugate pairs. If it is not located on the unit circle, then a zero of a symmetric spatial filter must have a reciprocal pair. When the polynomial coefficients are positive, then there is no real positive zero.
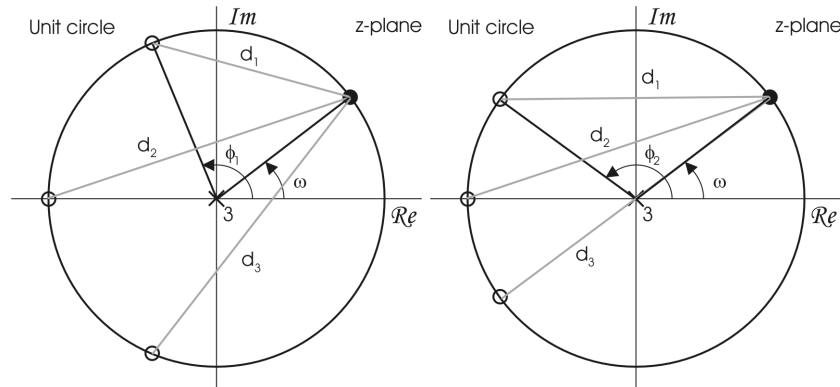
Figure 4.9: Pole-zero plots of two filters with the same numbers of zeros and poles. The positions of the complex-conjugate zeros are different in these two filters.

The left side of Figure 4.9 shows the locations of the zeros of a symmetric three-tap filter. One real zero is located on the unit circle's negative real axis. The other two are located on the unit circle at an angle of $\pm\phi_1$ from the positive real axis. The right side of Figure 4.9 shows the pole-zero plot of a three-tap filter, but with the complex zeros located on the unit circle at an angle of $\pm\phi_2$ from the positive real axis. Note that poles of a FIR filter are always located in the origin.

The magnitude response of a filter can be found by evaluating the filter's system function on the unit circle [44]. A zero's presence close to the unit circle causes the magnitude of the frequency response to be attenuated. In contrast, a pole located close to the unit circle causes the magnitude of the frequency response to be amplified. How much a zero or pole affects a specific frequency in the frequency response is determined by its distance from the evaluated point on the unit circle. In the example shown in Figure 4.10, d_1, d_2, and d_3 represent distances between the zeros and a point of the unit circle that corresponds to an evaluated frequency ω. The magnitude of $H(\omega)$ may be expressed by this equation [44]:

$$H(\omega) = |b_0| \frac{d_1 \cdot d_2 \cdots d_M}{v_1 \cdot v_2 \cdots v_N} ,$$

where d_n is the distance from a zero to the evaluated point on the unit circle and where v_n represents the distance from a pole to the same point. Since all poles are located in the origin, the distance between a pole and any point on the unit circle is 1. Hence, the equation above can be simplified:

$$H(\omega) = |b_0| \cdot d_1 \cdot d_2 \cdots d_M$$

Figure 4.11 shows the frequency response curves for the two filters shown in Figure 4.9. The filter shown on the left side of Figure 4.10 has zeros on the unit circle with angles π and ϕ_1 from the positive real axis. The corresponding frequency response has zero-crossings at those two frequencies. The second filter has zeros on the unit circle with angles π and ϕ_2 from the positive real axis, which results in zero-crossings at different frequencies. As demonstrated by the equation above, it is obvious that any given frequency in the magnitude frequency response is affected by every zero and every pole of the system function; the influence of zeros and poles is determined by their distances from the evaluated point.

Figure 4.10 shows a pole-zero plot of a filter constructed from the two filters shown in Figure 4.9. The position of the zeros is identical to the position of the zeros for the constituting filters. Therefore, the zero-crossing frequencies of these filters are the same. The magnitude frequency response of the combined filter is shown in Figure 4.12, which shows that the passband frequency components are lower than those of the individual three-tap filters. Similarly, the stopband frequency components are also more attenuated because additional zeros are located beyond the first zero-crossing.
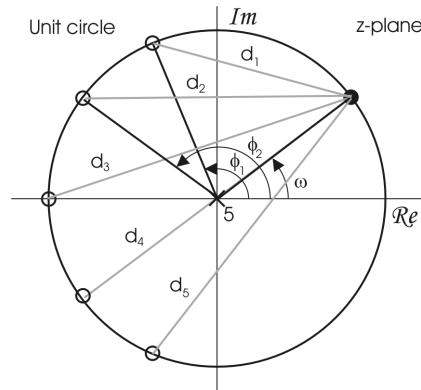
Figure 4.10: Pole-zero plots of a filter; the zeros and poles reflect the results of combining the two filters from Figure 4.10 into one filter.

As seen earlier, adding zeros to the system functions results in a better attenuation of the frequency components beyond the first zero-crossing. Since every zero and pole has a certain influence on each frequency of a response, adding zeros will have a negative consequence on the frequency components lower than the first zero-crossing.
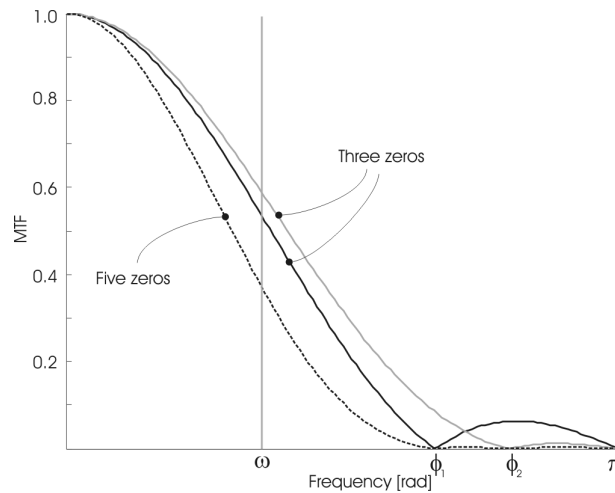
Figure 4.11: The theoretical magnitude frequency response of the filters from Figures 4.10 and 4.11. The zero-crossings' frequencies of the five-tap filter are the same as those of the two three-tap filters. The passband frequency components of the five-tap filter are lower than the passband frequency components of both three-tap filters.

Adding zeros located on the unit circle to a system function of a low-pass filter improves the attenuation of the stopband frequency components, but the adverse result of adding zeros is the degradation of the passband frequency components.

4.3.2 Coupling DOLPF and lens

The previous section explained how to design filter coefficients for the DOLPF when a fixed frequency response of the filter is one of the requirements. It also provided a few examples of such coefficients. In this section, we propose incorporating the lens characteristics into the design of the DOLPF filter coefficients. The DOLPF is dynamically controlled, and it is not imperative to have the frequency response of the filter fixed. Any alteration of the frequency response of the optical elements that are preceding and/or following the DOLPF may have effects on its coefficients while continuing to satisfy certain overall criteria. As shown earlier, the optical elements in the capturing system are cascaded, and each of them contributes to the system frequency response.

The fact that the frequency response of the lens is a function of the F-number is considered when designing the DOLPF filters. The amount of energy allowed in the stopband is a criterion.
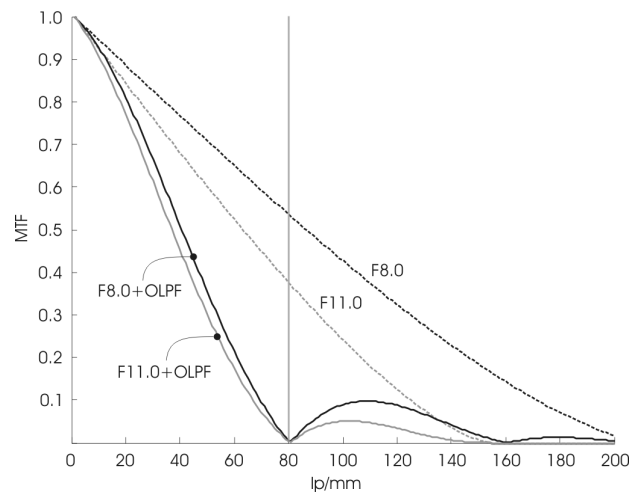
Figure 4.12: An example of a system that has a fixed OLPF. The four-tap OLPF has its first zero-crossing set to 80 lp/mm. Changing the F-stop of the lens also changes its frequency response.

Figure 4.12 illustrates an example of a system with a fixed frequency four-tap OLPF and a diffraction limited lens for two lens apertures. For demonstration purposes, the first zero-crossing of the OLPF is set to 80 lp/mm.

When observing the stopband frequency components of the combined response, it can be seen that the system whose aperture is set to F11 has these components attenuated better. This is easy to explain; the lens itself better attenuates higher frequency components when the aperture is set to F11 instead of F8.
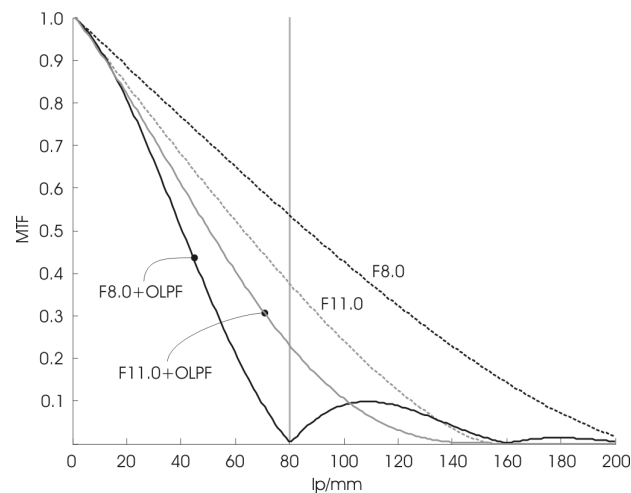
Figure 4.13: An example of a system with the dynamically controlled OLPF. Initially, the four-tap OLPF has its first zero-crossing set to 80 lp/mm. As the lens aperture is modified, the first zero-crossing of the filter is altered to keep the energy above the Nyquist frequency the same.

If the energy of a system above the Nyquist frequency is used as a parameter with the aim to keep it constant, then the frequency response of the DOLPF can be altered to compensate for the changes of the lens's frequency response. An example is shown in Figure 4.13. The DOLPF zero-crossing frequency, for a lens aperture of F11, is set to approximately 150 lp/mm to keep the energy equally above the Nyquist frequency in both systems. As a positive outcome, the passband frequency components for the system whose aperture is set to F11 are less attenuated, and its image appears sharper.

4.4 Controlling Bandwidth

The shape of the DOLPF's frequency response, as explained in the section 4.3, is determined by its number of filter taps and their amplitudes. This section will explain that for any given shape, the spatial distance between taps affects the bandwidth of the DOLPF frequency response. Earlier in this chapter, it was explained that the spatial positions of impulses in the impulse response of a filter are a function of the continuous angle at which the optical window travels around the axes. Therefore, the spatial distance between the impulses can be of any value and is only limited by the maximum angles of the window's rotation. In the following bandwidth control examples, the rectangle filters are used for illustration. This choice does not limit our study, and using any other filter would lead to the same conclusions.

Figure 4.14 shows the MTF for a rectangular filter with two taps, with three taps, and with four taps. In all three cases, the spatial distance between taps is kept the same. The figure shows that by adding filter taps, the number of zero-crossing is increased, but the width of the main lobe is decreased.
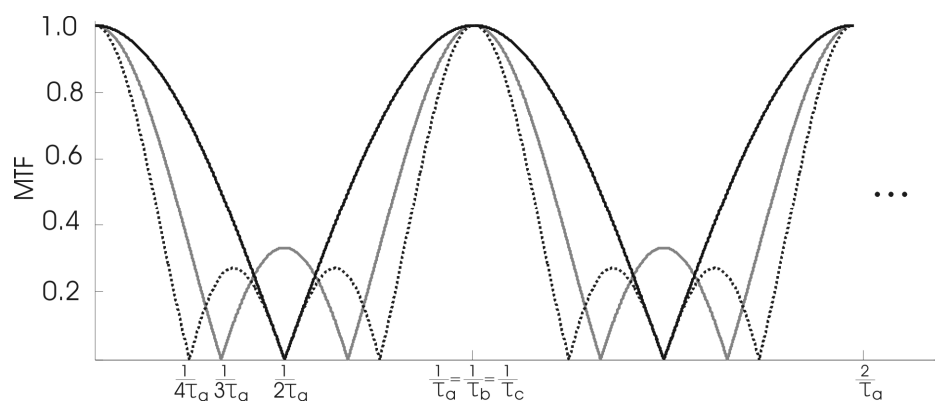
Figure 4.14: Theoretical MTF of two-, three-, and four-tap rectangle filters, whose spatial distances between taps are equal ($\tau_a=\tau_b=\tau_c$).

The frequency response of the filters is a periodic function with period $1/\tau$. Since it is a periodic function, one usually shows only the first period of the function. Figure 4.15

shows the theoretical MTFs of the two-, three-, and four-tap rectangle filters whose spatial

distances between taps are set so that the first zero-crossing is at the same frequency for

all three filters.
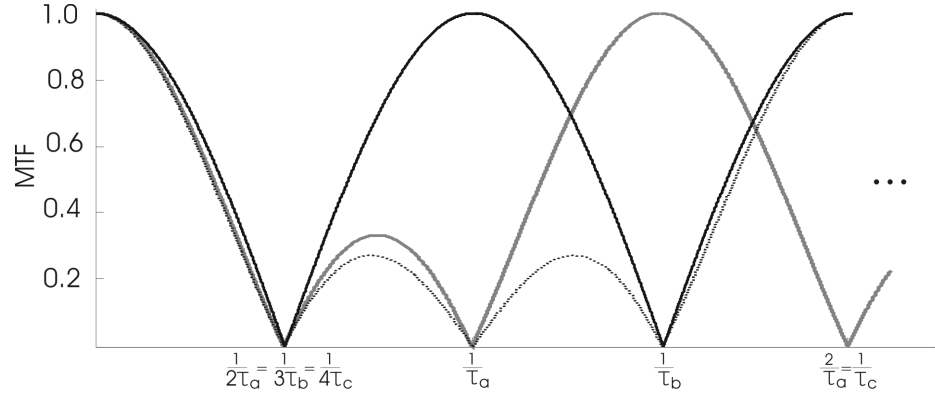
Figure 4.15: Theoretical modulation transfer functions of two-, three-, and four-tap rectangle filters, whose distances between taps are set to $\tau_a = 3\tau_b/2 = 2\tau_c$.
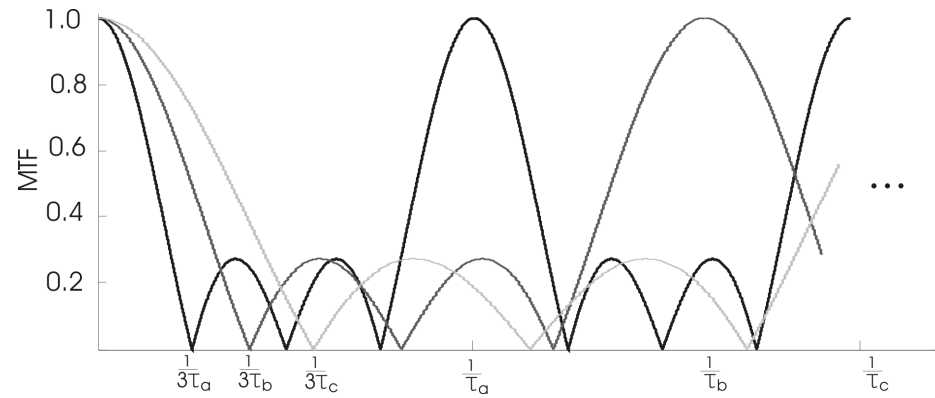
Figure 4.16: Theoretical modulation transfer functions of a three-tap rectangle filter for three different distances between filter taps (τ_a, τ_b, and τ_c).

Figure 4.16 shows the theoretical modulation transfer functions of a three-tap filter with

three different spatial distances between taps. Decreasing the distance between filter taps

is equivalent to increasing the sampling frequency. When the distance is infinitely small,

all filter taps merge into one tap, and the filter becomes an all-pass filter. Increasing and

decreasing the distance between taps can be viewed as stretching and contracting the

frequency response of the filter. It will be shown later that the practical implementation of

60

the DOLPF can control the spatial distances between taps with fine precision. This technique offers close control of the main lobe of the implemented filter and, consequently, of the filter's bandwidth. The control of the spatial distance between filter taps and the experimental results of the DOLPF will be addressed in the following chapter.

Chapter 5

Experiment Setup and Results

To validate the theory introduced in Chapters 3 and 4, a dynamic optical low-pass filter experiment is created, and its results are presented in this chapter. The first half of this chapter is dedicated to the description of the experiment and its elements, and the second half focuses on the results of the experiment.

5.1 Experiment Setup

This section provides information about the optical elements used in the experiment. It also provides details about the elements' settings and the tunings needed to achieve the desired effects. This experiment is designed to test the theoretical and practical aspects of the DOLPF. A part of the DOLPF consists of a window that is able to rotate only around the Y axis. Therefore, the lateral displacement of the image is in the horizontal direction only. As mentioned in Chapter 4, the window must also rotate around the X axis for the full two-dimensional spatial filter. Nevertheless, even this simplified experiment is sufficient to prove the theory presented in the previous chapters.

5.1.1 The DOLPF construction

Figure 5.1 shows a custom-built optical test fixture that was designed for the DOLPF experiment. A glass window made of B270 glass with an index of refraction n = 1.53 and

with dimensions of 25mm x 25mm x 2mm is mounted on an aluminum frame. Other

materials with similar or better performance, such as crown glass (including BK7 glass) or

sapphire, can be used. The window is coated on both sides with a single-layer

antireflective magnesium fluoride coating. The window is fixed on the frame using optical

cement. The frame with the window has one degree of freedom of motion, and it is able to

rotate around the vertical axis (Y axis). The window is mounted on a fixed frame, which

also holds a linear piezo actuator. The depth of the fixed frame is set to 11mm so that the

whole test fixture can be positioned between the lens mount and the imager. The whole

construction is attached to a plate, which allows anchoring to a stable platform, such as an

optical bench.
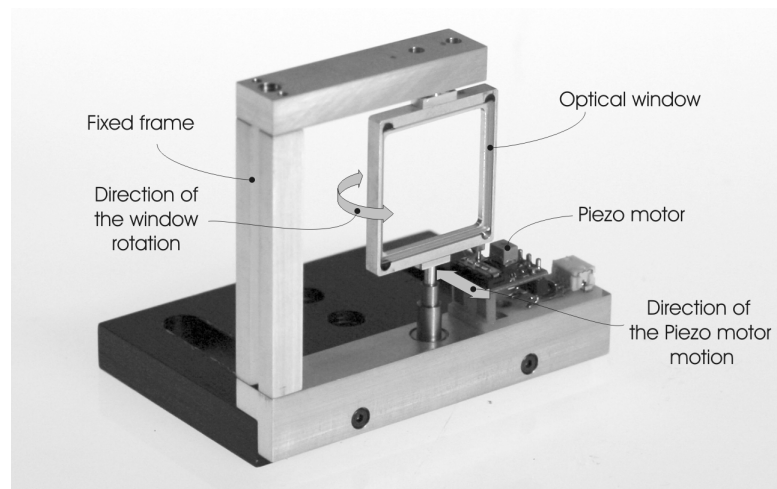
Figure 5.1: The optical test fixture designed for the DOLPF experiment.

The frame with the optical window is subject to rapid movement; hence, it is important to

keep it as light as possible. The total weight of the frame with the glass window is 5.3

grams, which allows the piezo actuator to move the frame in a rapid manner.

The linear piezo actuator, P-653, manufactured by Physic Instruments, is a miniature

linear motor with a 2mm travel range and a velocity of up to 200 mm/s without load. The

piezo actuator is controlled, in an open loop, by a custom-built microprocessor board,

which allows precise timing. The motor is attached to the frame at the exact edge of the window glass, at 12.5 mm from the axis of rotation. Therefore, for every 1μm of piezo motor linear travel, the window rotates for approximately 0.00458^o. The travel range of the motor is 2mm, which allows a maximum rotation of 9.1^o. For every 1μm of piezo motor linear travel, the emergent ray is displaced relatively to the incident ray by approximately 55nm, provided that the optical glass window is 2mm thick.

5.1.2 Target

The quality of the target used for the MTF measurements plays a determining role in the accuracy of the results. Among several MTF measurement methods and their applicable targets [1], one with sinusoidal patterns proved to be the easiest to manufacture and to use for the MTF evaluation. The target, shown in Figure 5.2, is designed specifically for the experiment, with the goal of obtaining a detailed MTF measurement of the elements of the image capturing system.
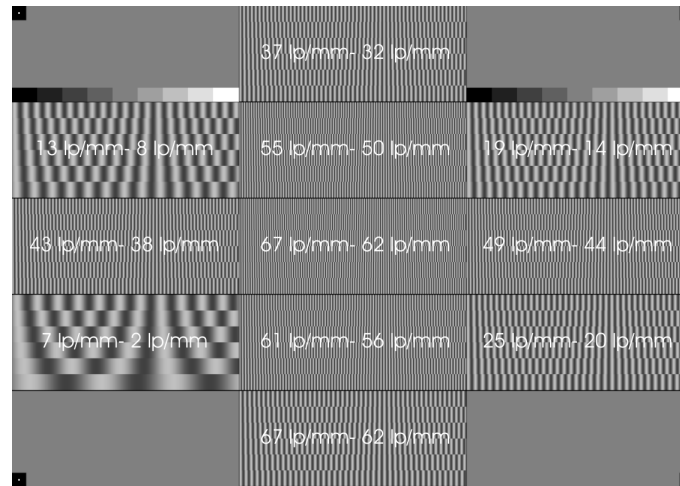
Figure 5.2: The target designed for the experiment. When the target's image is formed on the sensor, the frequencies indicated on the target are present in the captured image.

The sinusoidal patterns, which have the same modulations but varying frequencies, are printed in eleven groups with six patterns in each group. In order to minimize the off-axis

effects of the lens MTF, the groups with higher frequency components are printed at the center of the target, whereas the groups with the lower frequency components are printed closer to the edges of the target. There are a total of 66 sinusoidal patterns, the frequencies of which range from 0.031056 lp/mm to 1.040366 lp/mm. When the target is properly framed, an image of the target, consisting of sinusoidal patterns whose frequencies range from 2 lp/mm up to 67 lp/mm, is formed on the sensor. The highest frequency formed on the sensor is also the Nyquist frequency of the sensor used in the experiment. The target is printed using a continuous tone printer Durst Lambda, manufactured by Durst Phototechnik AG [45]. A printing density of 400 dpi (15.75 dots/mm) guarantees that the highest frequency sinusoidal pattern is represented by at least 15 dots per cycle.

After each printing cycle, the target is assessed according to two criteria: linearity and modulation transfer function. The printing is repeated until a target that has a satisfactory linearity and modulation transfer function is created.
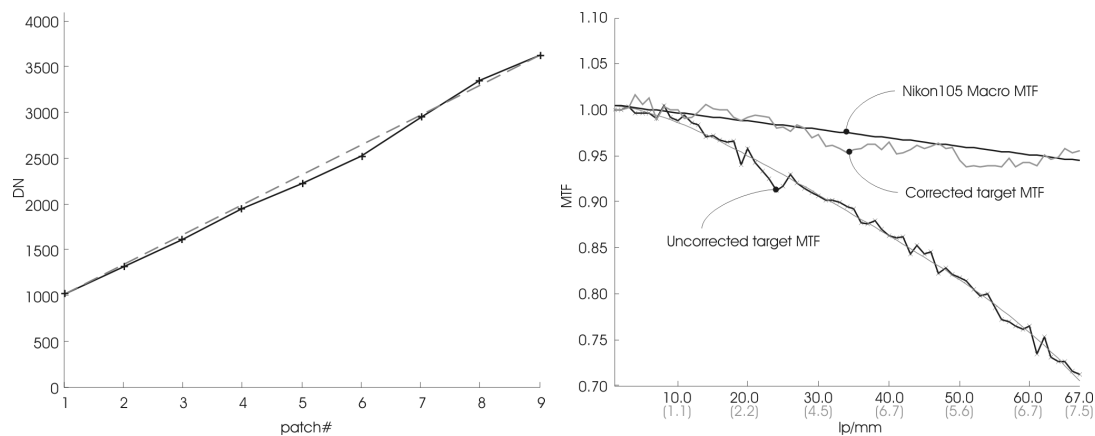
Figure 5.3: The linearity of the final target is shown on the left. On the right is the target's MTF before and after compensation for the printer's MTF.

To aid the linearity test of the printing process, two linear grayscales with 9 steps ranging from black to white are printed on the target. The linearity is estimated using a digital camera whose linearity was previously established using a calibrated exposure chart

manufactured by Sekonic [46]. The left side of Figure 5.3 shows the output of the camera when pointed to the grayscale of the target, after the final target corrections have been incorporated and before printing. The X axis represents the grayscale patch number, whereas the Y axis represents the average value of the given patch. A straight line connects the lowest and highest values in the figure for reference. The MTF of the printer alters the frequency components of the prints, and it must be counteracted in the target printing process. The MTF of the printer is estimated by capturing a close-up of each sinusoidal pattern with the digital camera. When the target is captured from a close distance, the lens and camera have less influence on the frequency components in the captured target. For instance, when the target is correctly framed, the center sinusoidal pattern forms a pattern on the sensor with a frequency of 67 lp/mm. However, when the target is captured from a close distance, the same sinusoid forms a pattern with a frequency of 7.5 lp/mm. The black line in the graph on the right side of Figure 5.3 shows an uncorrected MTF of the target affected by the printer MTF. For reference, the graph also indicates the MTF of the lens used for the printer MTF estimation. The gray line shows the estimated MTF of the final target after compensation for the printer's MTF. As seen in the figure, the MTF error of the final target is approximately 2%.

5.1.3 Camera and supporting electronics

The 2-megapixel GE1900 is a high-resolution CCD camera with a gigabit Ethernet interface [47]. The GE1900 incorporates a 1"-format HD-resolution Kodak KAI-2093 CCD sensor [48]. The sensor's resolution is 1920 x 1080, and its dimensions are 14.208mm x 7.922mm with 7.4μm square photosites. The sensor's Nyquist frequency is 67.5 lp/mm, and it is the same in both vertical and horizontal directions. The camera is equipped with an external trigger control, and it provides a line that indicates when the sensor is being

exposed. Both the external trigger and the exposure indication are required in order to synchronize the DOLPF with the camera.

The main controller board consists of a general-purpose processor SC143, made by BECK IPC GmbH [49], and a Virtex II field programmable gate array (FPGA) made by Xilinx [50]. The driving signals for the piezo linear actuator are designed based on $1\mu s$ timing increments, and they should never be interrupted when the actuator is moving. Any departure from the designed timing of the piezo control signals will affect the impulse response of the implemented filter. A custom-written FPGA firmware driver, controlled by CPU, provides the desired precision and repeatability.

5.1.4 Overall experiment setup

The camera is mounted onto a linear stage with a micrometer. The DOLPF is placed between the camera and the lens mount with a 55mm Nikon lens, as shown in Figure 5.4. The flange focal distance for the Nikon lens is 46.5mm, and our system does not violate this constraint. The DOLPF, the lens mount, and the lens are anchored to the optical bench.
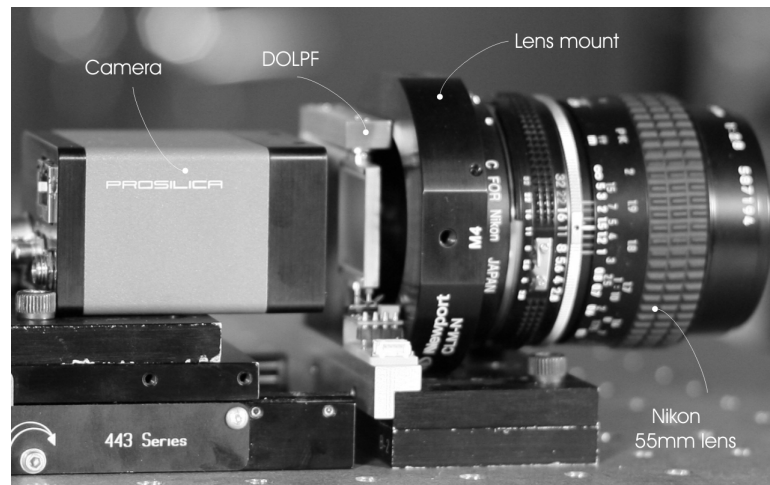
Figure 5.4: The overall optical setup shows the camera, DOLPF, lens mount, and lens. The DOLPF is positioned between the lens and the camera.

The lens aperture is set to F8.0, which was established earlier (using the MTF bench) as the aperture setting that has the best MTF response. The coarse focusing is accomplished with the lens, while the back focusing is accomplished using the linear stage with the micrometer. Focusing is aided by a custom software program that indicates when the optimal focus is reached. The ability to focus on the target and the negligible vignetting are determined when setting up the experiment. The DOLPF and the camera are connected to a CPU board, which provides timing and synchronization. All elements of the experiment are controlled from a PC, which allows interactive modifications of the DOLPF. The DOLPF rotation must occur simultaneously with the imager exposure, which is why the DOLPF is synchronized with the camera. The captured frames are transferred to the PC via Ethernet cable for image processing and MTF estimation.

5.2 Tuning the DOLPF

The displacements and angles in the DOLPF are in the order of microns and fractions of degrees. To measure such small values, an experiment (shown in Figure 5.5) is conducted to determine the accuracy of the DOLPF control. An alignment laser is pointed toward the DOLPF at a 30° angle. A laser beam, partially reflected from the glass window surface, is projected onto a board positioned several meters away. A measurement tape is attached to the board so that the bounced laser motion displacement can be read directly.

The distance between the DOLPF and the board is carefully set so that the window rotation, which corresponds in a lateral displacement of 1 μm of the ray passing through the window, would result in a laser beam displacement of 10 mm on the board. A digital still camera, not synchronized with the window rotation, is used to capture the trace of the laser beam as it moves across the board when the window is in motion.
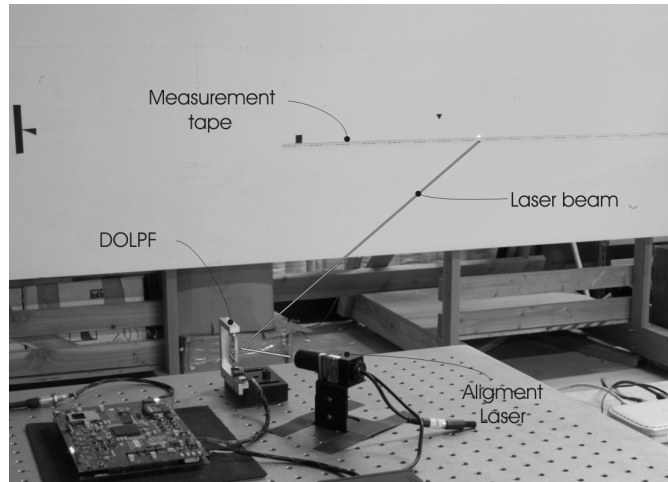
Figure 5.5: The optical experiment for tuning the DOLPF. In the foreground—on the optical bench—is the alignment laser, the optical test fixture, and the CPU board. In the background is the board with the calibrated scale.

The camera exposure is set to 1 second so that it can capture the trace that the laser

beam travels. Figure 5.6 shows the trace of the laser beam on the board as the window

rotates from its resting point on the right to its resting point on the left. The control

software is set to stop for a few milliseconds at the four positions between the resting

points. For measurement purposes, the scale under the beam trace consists of 10 mm x

10 mm squares. As seen in Figure 5.6, the beam travels between the stops for

approximately 50 mm, which corresponds to a ray lateral displacement of 5 μm. It can

also be seen that due to the rapid window movement between stops, the window does not

immediately stop at the desired position but rather keeps oscillating before it comes to a

complete rest. The maximum amplitude of the oscillation is estimated at 2 μm. It is

important to emphasize that we are interested in the points between the resting positions,

which are highlighted by white squares. In order to minimize the oscillations when the

window reaches a desired position, the control signal is modified using the "input shaping"

technique [51]. This yields excellent results in canceling the oscillations, as shown in

Figure 5.6. The window oscillations are canceled, which results in a single dot on the board

for each stop. The window spends an equal time at each of the four points, resulting in spatial filtering of a passing image with the four-tap rectangle filter.
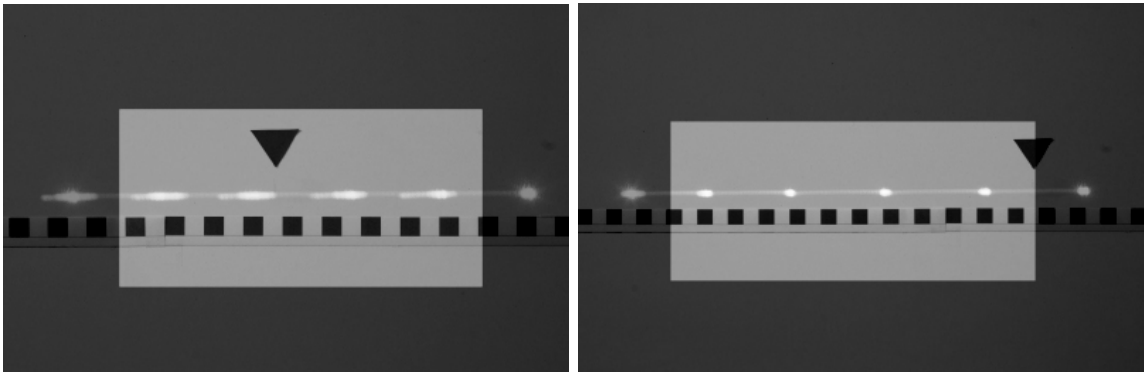
Figure 5.6: The trace of the laser beam bouncing off the glass window and stopping at four points. The laser beam travels from the resting point on the right to the resting point on the left. The left side shows the trace when the control signal is uncompensated. The right side shows the trace when the window is controlled with a compensated signal.

In the following few examples, the spatial effects of the DOLPF on the image are demonstrated. It was shown in Chapter 4 that when the DOLPF moves during the single exposure, it causes a lateral movement of the formed image on the imager, forming several copies of the scene. After the image exposure is completed, all image copies are integrated into one resulting image. On the left side of Figure 5.7, the properly framed target captured by the Prosilica camera is shown.
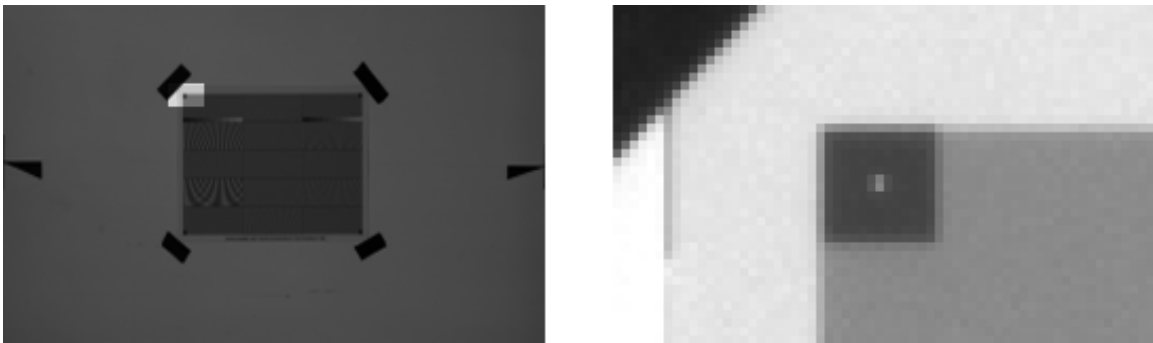
Figure 5.7: The white square in the left figure shows the position of the magnified area of the target shown on the right. The DOLPF is not moving during the single exposure.

The white square located at the top left corner of the target shows the enlarged portion

that is shown on the right side of the figure. During the sensor exposure, the DOLPF is not

moving, and the output image is formed from only one copy. The feature on the target

activates a small portion of the sensor, which is approximately one photosite in size.
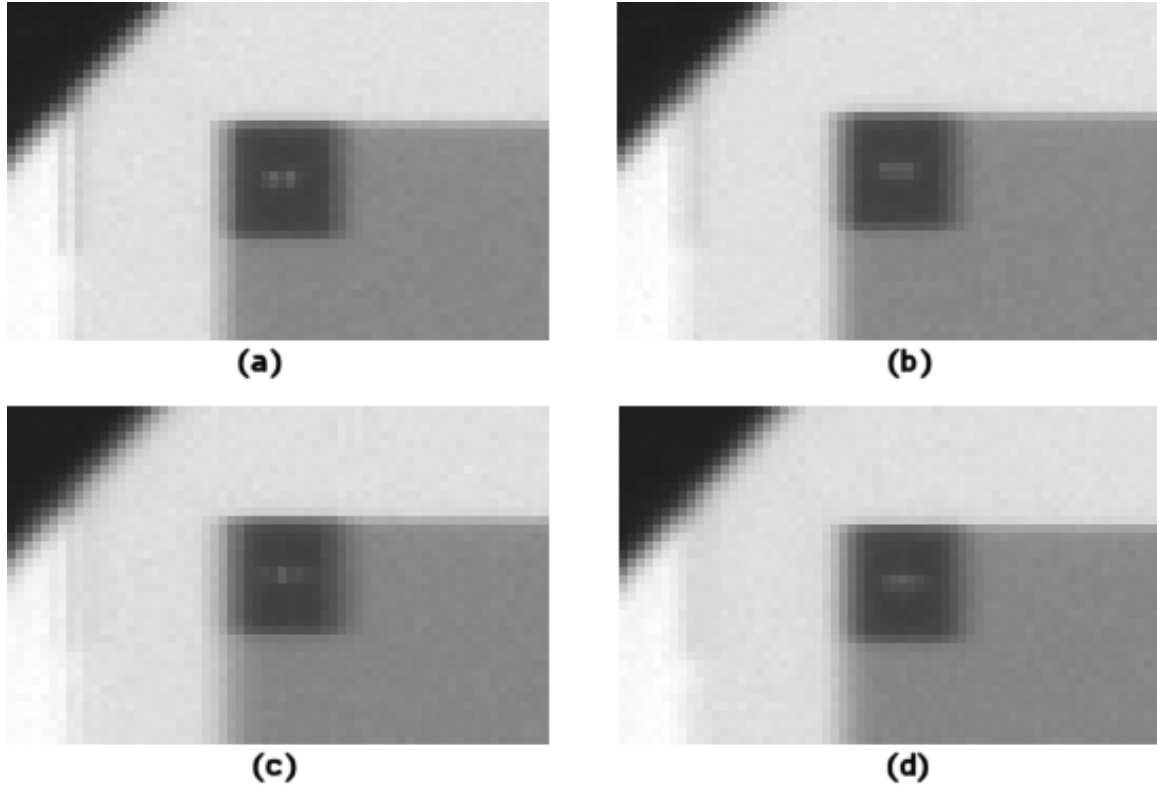
Figure 5.8: The two-tap rectangle filter is shown in (a). The three-tap rectangle filter is shown in (b). Figures (c) and (d) show the three-tap and five-tap triangle filters, respectively.

Figure 5.8 illustrates four examples of the resulting images formed by the integration of

the several laterally displaced image copies during the single exposure. The copies are the

results of the DOLPF rotating around the Y axis. In these examples, the DOLPF rotation is

intentionally exaggerated for demonstration purposes. Normally, the DOLPF rotation will

result in a lateral displacement of the copy that is less than the dimensions of a photosite.

For example, the copies in Figure 5.8(a) are more than one photosite apart, which would

result in the zero-crossing frequency being significantly lower than the Nyquist frequency

of the sensor. Figures 5.8(a) and 5.8(b) respectively show the continuous scene filtered by the two- and three-tap filters. Figures 5.8(c) and 5.8(d) show the target filtered by the three- and five-tap triangle filters, respectively.

To reiterate a conclusion made in Chapter 4, the lateral moves of the copies across the imager are not limited by the sampling structure of the sensor, only by the continuous angles at which the filter travels around the axes. This allows us to create a prefilter that is not limited by the sensor's sampling structure.

5.3 Results

This section demonstrates the achieved level of control over the DOLPF, in terms of the filter's bandwidth and shape. An OLPF is not an image-forming device; therefore, its frequency response can be observed only when it is combined with other optical elements. In order to interpret the results properly, Figure 5.9 illustrates how the observable overall frequency response (the black line) is the result of the interaction between the lens and the OLPF responses.
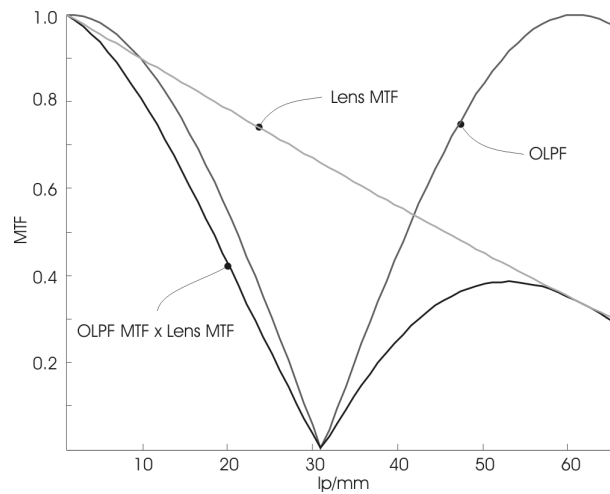
Figure 5.9: An illustration of the lens's effect on the overall response. The black line represents the observable response after the OLPF response is altered by the lens's MTF.

For the demonstration only, the spatial optical filters used in the examples are designed to attenuate frequencies above 30 lp/mm. As a reminder, the Nyquist frequency for the sensor is 67 lp/mm, and setting the first zero-crossing frequency of the filter at 30 lp/mm allows us to evaluate the characteristics of the DOLPF without aliasing.

5.3.1 The shape of the DOLPF

The results of implementing several different filters with the DOLPF (such as rectangle, Tukey, Gaussian, triangle, Hanning, and Blackman-Harris) are presented in this section. In addition to discussing theoretical and practical results, brief information about each filter is given.

Using complex filters has been validated in certain fields. It will be shown in the following subsections, however, that their implementations with the DOLPF are not always justified. In Chapter 3, we highlighted two characteristics of the system frequency response that are of critical interest when selecting a filter: the attenuation of the stopband frequency components and the width of the main lobe. In the following examples, we examine these two parameters in both measured and theoretical system frequency responses for the selected filters. It will be shown that the implementation of a complex filter (such as Blackman-Harris or Hanning) instead of a simpler filter (such as Tukey or Gaussian) contributes little to the improvement of the overall system performance.

DOLPF based on a rectangle filter

The rectangle filter is the simplest filter to implement since it is a constant over the nonzero interval. Figure 5.10 shows the rectangle DOLPF theoretical response, and Figure 5.11 shows the measured system response. In both figures, several frequency responses are calculated for different numbers of filter taps. As seen in both figures, when observing the attenuation of the stopband frequency components, there is a modest gain in

73

attenuation if the number of taps is increased beyond four. The main lobe is minimally

affected with any selection of tap number.
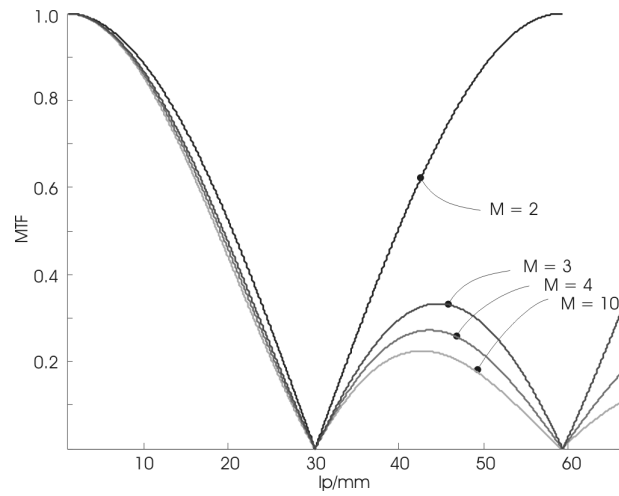
Figure 5.10: Theoretical MTFs for the DOLPF, implementing two-, three-, four-, and ten-tap rectangle filters.
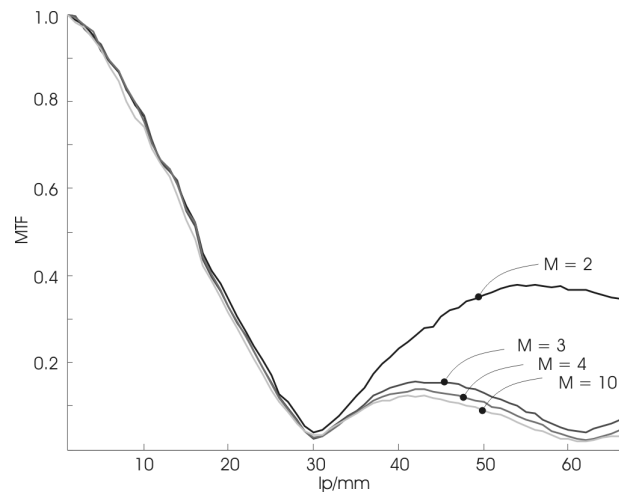
Figure 5.11: Measured overall MTFs for a system with a rectangle filter. Four measurements, with the filters having different numbers of taps (M = 2, 3, 4 and 10), are shown.

DOLPF based on a Tukey filter

The Tukey filter represents an attempt to smooth the boundaries at the end of the

rectangle filter. The parameter α controls the smoothness of the edges; for α close to 0,

the filter resembles the rectangle filter, whereas when α is close to 1, the Tukey filter

resembles a cosine function. As seen in Figures 5.12 and 5.13, the stopband frequency components for α greater than 0 are more attenuated than with the rectangle filter. However, the main lobe is also affected, especially for α closer to 1.
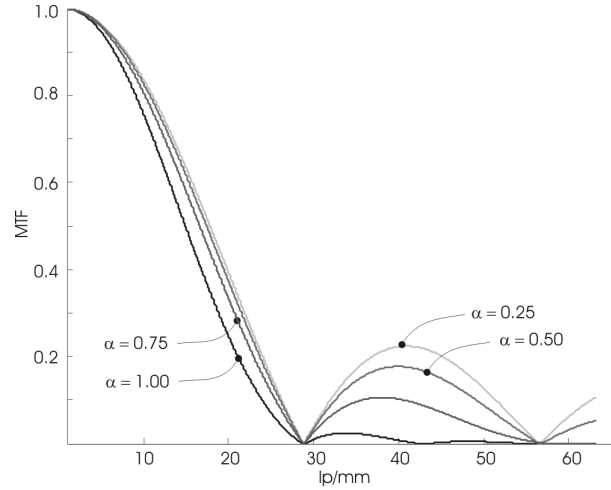
Figure 5.12: Theoretical MTFs for the DOLPF, implementing a ten-tap Tukey filter for four different alphas.
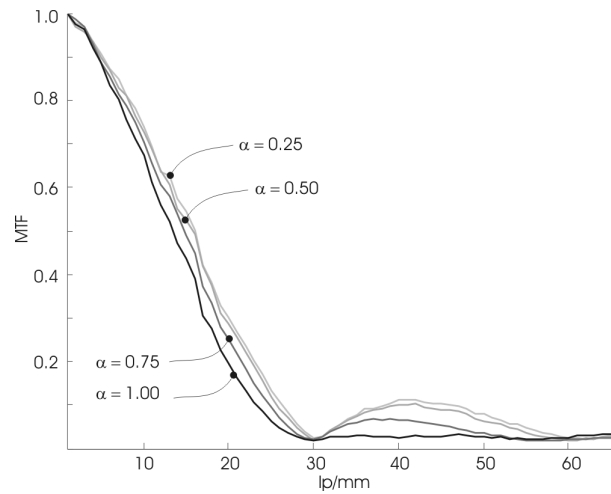
Figure 5.13: Measured overall MTFs for a system with a ten-tap Tukey filter and varying parameters α.

DOLPF based on a Gaussian filter

This filter is parameterized on α, the reciprocal of the standard deviation, which is a measure of the width of the filter's Fourier transform. For α close to 1, the severity of the

discontinuity at the filter's edges is significant, which results in noticeable sidelobes. As seen in Figure 5.14, the MTF of the Gaussian filter, for α close to 1, is similar to the MTF of the rectangle filter. On the other hand, for α greater than 1, the tail of the filter in the spatial domain is thinner, and the stopband frequency components are better attenuated. However, as seen in both Figures 5.14 and 5.15, the width of the main lobe is also more affected; when α is greater than 2, the main lobe of the system MTF is significantly altered.
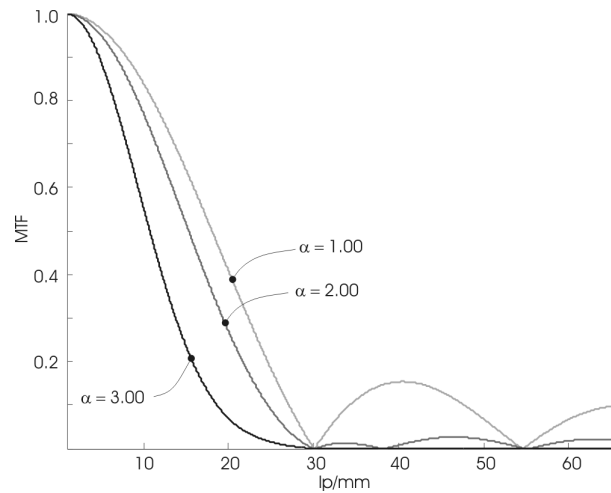
Figure 5.14: Theoretical MTFs for the DOLPF, implementing a ten-tap Gaussian filter and three different alphas.
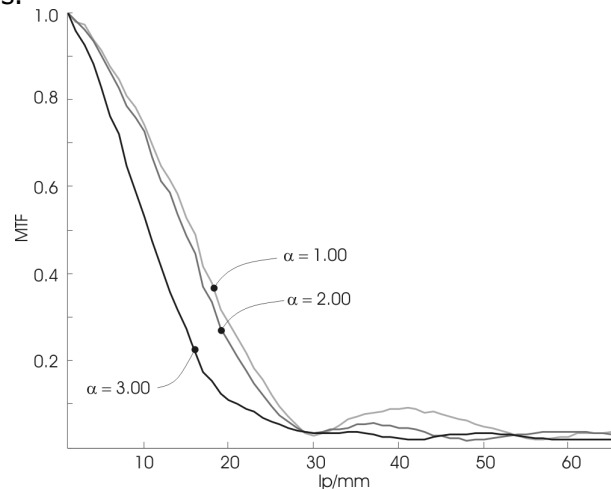
Figure 5.15: Measured MTFs of a system with a ten-tap Gaussian filter and three different alphas.

DOLPF based on triangle, Hanning, and Blackman-Harris filters

The modulation transfer function of the triangle filter is the squared MTF of the rectangle filter [42]. The Hanning and Blackman-Harris filters are constructed from cosine kernels, and they are not easy to generate. As seen in Figures 5.16 and 5.17, the two filters' stopband frequency components behave in the same fashion, but the Blackman-Harris filter has the best characteristics (although it also has the narrowest main lobe).
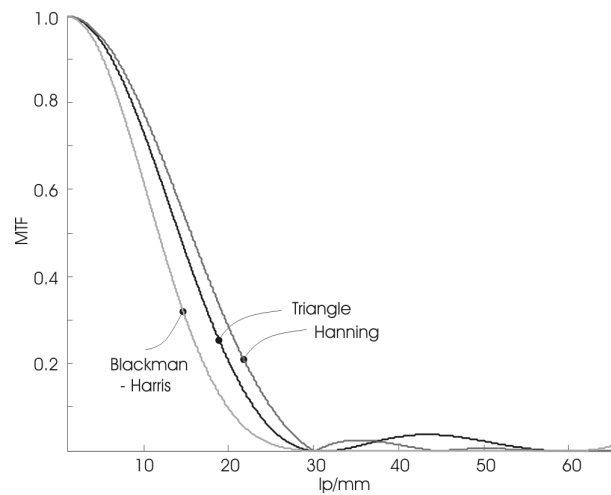
Figure 5.16: Theoretical MTFs of the DOLPF, implementing ten-tap triangle, Hamming, and Blackman-Harris filters.
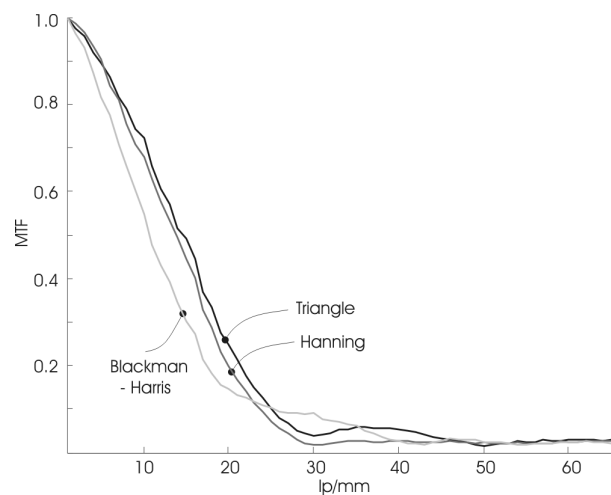
Figure 5.17: Measured MTFs of a system with ten-tap triangle, Hamming, and Blackman-Harris filters.

5.3.2 Coupling the DOLPF with the lens

In Chapter 4, we stated that it would be beneficial to couple the DOLPF with other optical elements of the capturing system. The rationale for this assertion is the idea that any alteration of the frequency response of the optical elements that precede and/or follow the DOLPF may alter the filter's coefficients while continuing to satisfy certain overall criteria. Figure 5.18 shows the measured MTFs of the Nikon 55mm lens with the lens aperture as a parameter. As seen in the figure, the lens itself behaves as a low-pass filter.
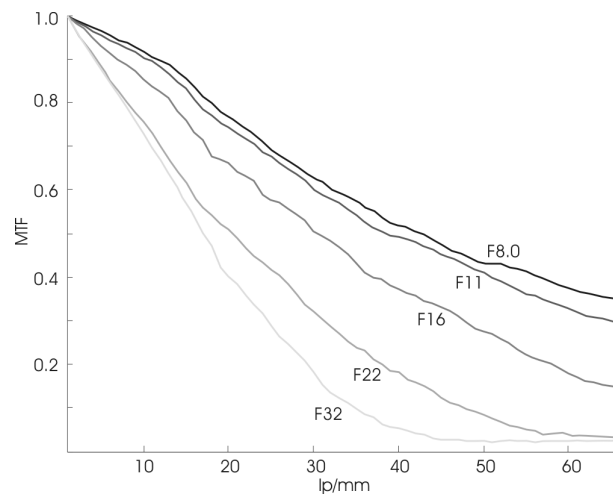
Figure 5.18: Measured system MTFs without an OLPF. This figure shows that the lens's MTF when is mostly dominated by the lens's diffraction limitation.

Figure 5.19 shows the measured MTFs of a system in which the equivalent of a classic 4-point separation birefringent OLPF is placed in front of the sensor. The first zero-crossing of the filter is set at 30 lp/mm. As seen in the figure, for the lens aperture set to F8, there is a possibility of aliasing since the filter attenuates the stopband frequencies only to a certain extent. However, as the lens aperture changes, the diffraction limitation of the lens has more influence. Finally, when the lens aperture is set to F32, the frequency

components above 30 lp/mm are almost completely attenuated by the lens's low-pass filtering characteristics.
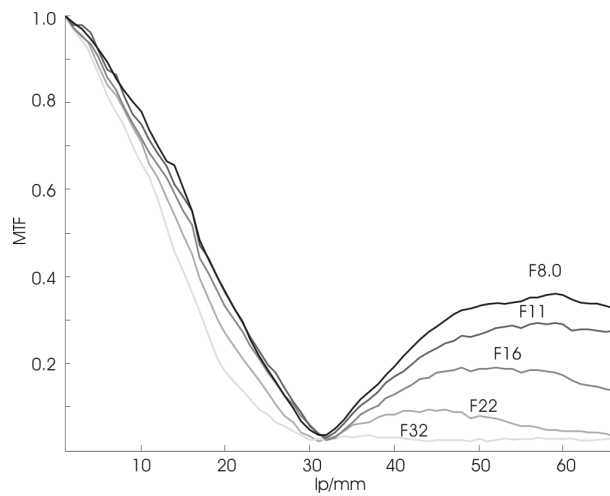
Figure 5.19: Measured overall MTFs for a system with a fixed four-point separation birefringent OLPF, set at approximately 30 lp/mm and at various aperture positions.
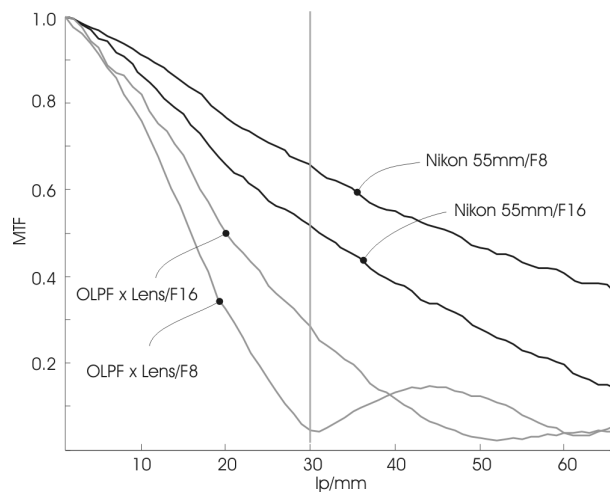
Figure 5.20: An example of a system that uses the dynamically controlled OLPF.

Figure 5.20 illustrates an example when the DOLPF MTF is altered to accommodate for a change in the MTF of the lens. The three-tap rectangle filter, with its first zero-crossing set at 30 lp/mm, is used when the lens aperture is set to F8. If we desire to keep the power of the signal above the Nyquist frequency constant, then the first zero-crossing of the filter can be moved to 50 lp/mm when the lens aperture is set to F16. This modification

decreases the passband frequency attenuation, which results in an increased sharpness of the resulting image.

5.3.2 The bandwidth of the DOLPF

In Chapter 3, we explained how the distance between the filter's taps alters the bandwidth of the DOLPF. In essence, the filter's bandwidth is determined by the angles at which the window travels around the axes of rotation before stopping at the selected points. Figures 5.21-5.25 demonstrate the level of bandwidth control for several filters previously discussed (rectangle, triangle, Blackman-Harris, and Tukey).

In the given examples, we attempt to raise the first zero-crossing frequencies from 30 lp/mm to 80 lp/mm, moving in 10 lp/mm steps. The selected zero-crossing values are chosen only for demonstration purposes; they can be any desired values. These examples clearly demonstrate that we can accomplish precise control of the optical prefilter bandwidth with the DOLPF and with dynamic changes, if required by the application.
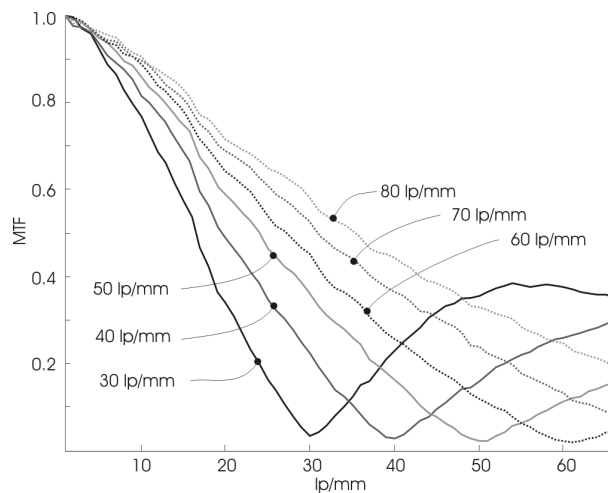
Figure 5.21: Demonstration of the MTF bandwidth control for a system that uses a two-tap rectangle filter. Note the significant sidelobes in the filter's response.
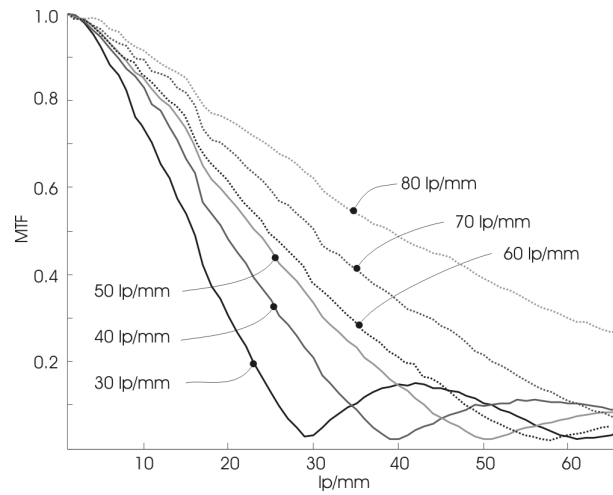
Figure 5.22: Demonstration of the MTF bandwidth control for a system that uses a three-tap rectangle filter.
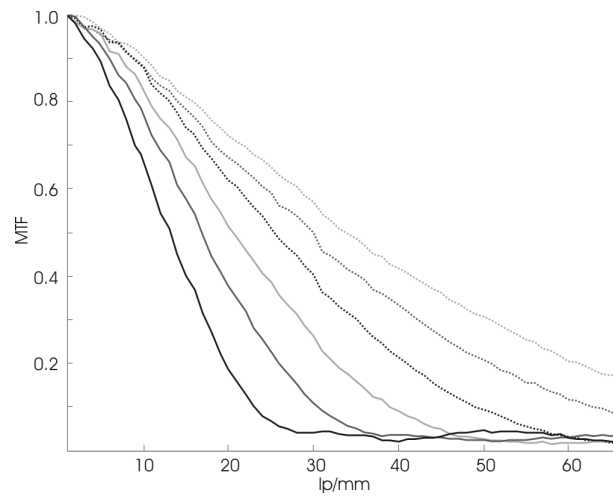
Figure 5.23: Measured MTFs of a system with a five-tap triangle filter and a variable bandwidth.
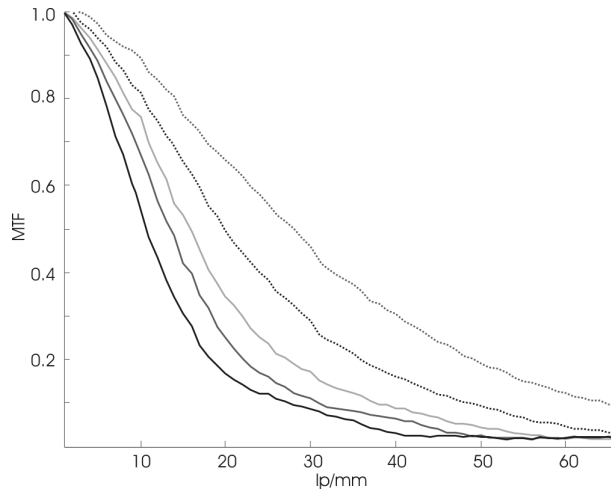
Figure 5.24: Measured MTFs of a system with a ten-tap Blackman-Harris filter and a variable bandwidth.
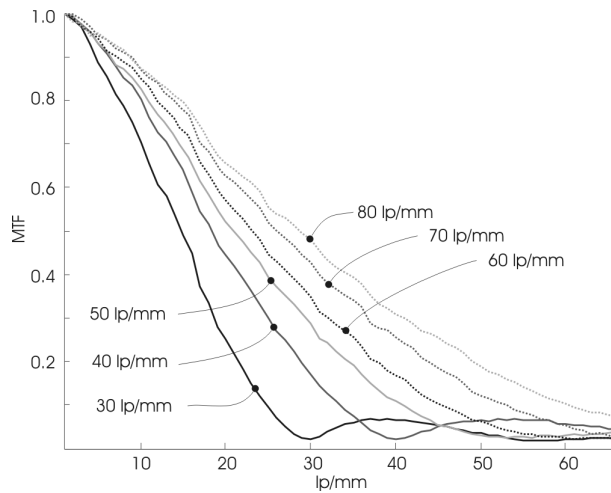
Figure 5.25: Measured system MTFs with a ten-tap Tukey filter (α=0.75) and a variable bandwidth.

5.3.3 Additional observations

In the previous section, we studied symmetric filters with positive coefficients that have all zeros located on the unit circle in the zero-pole plane. As shown in Chapter 3, a zero located on the unit circle results in a zero-crossing in the frequency domain. The dynamic optical low-pass filter does not necessarily require that the implemented filters have

symmetric responses. In such a case, the zeros of the system function are not necessarily located on the unit circle in the zero-pole plane—this results in the absence of a zero-crossing in the frequency domain.
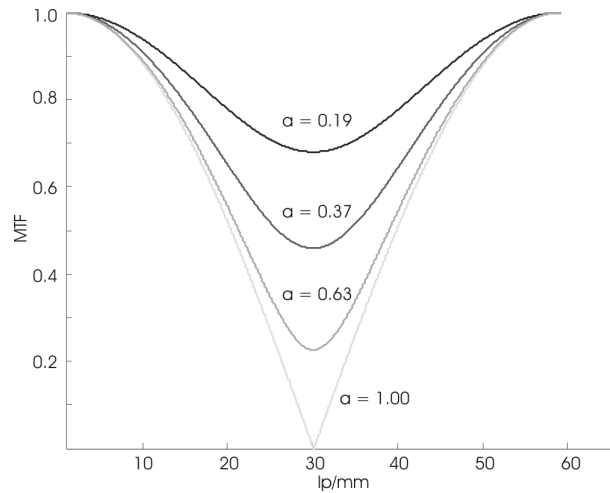
Figure 5.26: Theoretical MTFs of a two-tap filter, where the parameter "a" represents a ratio between the filter's coefficients.
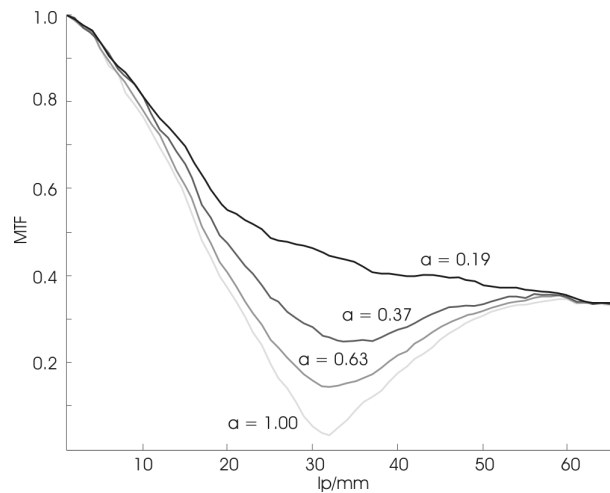
Figure 5.27: Measured overall MTF for a system with a two-tap OLPF, where the parameter "a" represents a ratio between the filter's coefficients.

Figure 5.26 shows the theoretical modulation transfer function of a two-tap filter, where the parameter "a" is a ratio between the amplitudes of the filter. When two taps are equal in amplitude, then the filter is a regular two-tap filter, which we presented and analyzed in

Chapter 3. Conversely, as the coefficient ratio decreases, the filter tends to behave as an all-pass filter. As seen in Figure 5.26, we can control the attenuation at a desired frequency by varying the ratio between the filter's coefficients. Figure 5.27 shows the measurements of the practical implementation of such a filter.

Chapter 6

Conclusions and Future Research

In this work, the author proposed and demonstrated the use of a parallel optical window positioned between a lens and a sensor as an optical low-pass filter. Controlled X- and Y-axes rotations of the optical window result in a manipulation of the point-spread function of the system. Consequently, changing the point-spread function of the system affects some portions of the frequency components contained in the image formed on the sensor. The ability to manipulate the frequency components of the image before it is digitized is important when we want to prevent aliasing. Despite the fact that an optical low-pass filter is intended to manipulate a continuous signal, we demonstrated that it can be analyzed with tools coming from the discrete signal domain. We also showed that, due to physical laws, the filters used for shaping the system PSF can be implemented only as FIR filters with nonnegative coefficients.

In the dissertation, the author demonstrated the ability to precisely control the optical window rotation, which enabled the use of various filter functions: rectangle, triangle, Tukey, Blackman-Harris, and others. Based on the evaluation of two critical characteristics of the system frequency response (i.e., the attenuation of the stopband frequency components and the width of the main lobe), we showed that the implementation of a complex filter (such as the Blackman-Harris or Hanning) instead of a simpler filter (such

as the Tukey or Gaussian) contributes little to the improvement of the overall system performance.

In addition to the ability to change the PSF, this study demonstrated that the PSF can be manipulated dynamically, which allowed us to change the PSF to counteract any alteration of other optical elements of the capturing system. This ability was demonstrated by altering the frequency response of the OLPF to compensate for the lens's frequency response changes when the aperture is changed. It was also demonstrated in theoretical analysis and supported by practical examples that this implementation of the optical low-pass filter has the ability to control the bandwidth with fine precision.

In the dissertation, an optical simulation software package was used to demonstrate that positioning the parallel optical window in front of the sensor does not significantly affect the performance of the system, and that it is an acceptable tradeoff, considering that the intended purpose of the window is low-pass filtering.

An extended evaluation of currently used birefringent-based optical low-pass filters is provided. In their basic form, birefringent OLPFs are simple, reliable, and relatively inexpensive, but they also present a few drawbacks, which the author attempted to address with this work.

Nevertheless, the DOLPF has several shortcomings. One of them is the requirement to complete the motion of the parallel optical window before the image exposure is complete. In modern digital still cameras, exposure time can be very short, which would require very fast window rotations. This requirement may limit the use of this approach to image acquisitions with relatively longer exposures, such as digital film and video capturing.

A second important drawback was noticed during the experiment execution: there is a minimum time required for rotating the window from one position to another. The angle of the window rotation directly determines the distances between the taps in the filter. As we

demonstrated in the work, the distances between taps determine the bandwidth of the filter. To cover even the smallest distance between filter's taps, the time that the window spends traveling from one point to another is greater than zero. When the number of filter taps is bigger and/or the image exposure is shorter, the time that the window spends traveling between the taps can negatively affect the frequency response. On the contrary, for a smaller number of taps or a longer image exposure, the traveling time can be neglected.

In this particular implementation of the DOLPF, a piezo actuator was used for rotating the parallel optical window. Although this actuator met the requirements for speed and travel distances, a noise generated during the rotation was not acceptable.

In order to maintain a reasonable scope for this work, some additional ideas were left for further research. Future works should investigate the possibility of designing a dynamically controlled, optical low-pass filter that takes into consideration the sensor color filter array. Specifically, for the sensors with color filter arrays that sample the color information with unequal sampling frequency (e.g., Bayer pattern CFA), achromatic DOLPFs can be tuned only to a single color. That would leave the color with a different bandwidth that is insufficiently filtered or filtered too aggressively, resulting in aliasing or damaging the image MTF, respectively.

Another direction for research concerns the extension of the DOLPF's implementation to a two-dimensional filter. The current implementation used to experimentally support the claims stated in this dissertation, showed its ability to rotate around one axis only, which results in a one-dimensional filter. This was sufficient to demonstrate the idea, but extending the filter's support to a second dimension would allow experiments with separable, nonseparable, symmetrical, nonsymmetrical, and other types of filters.

Appendix A

Optical Simulation Details

The lens used in the simulation is a Double Gauss type lens, which prescription is a part of the Code V software package. The reasoning behind the use of this particular type of lens is that the lens that is used in the final experiment is a Nikon 55mm lens, which is also a Double Gauss type of lens. The inability to obtain the prescription for a Nikon 55mm lens left me with no option but work with a similar lens. The lens was scaled to have an effective focal length (EFL) of 55mm. The aperture stop of the lens was set to F4.0 to make it a diffraction limited lens. The goal was to minimize the influence of the lens aberration on the results.

The angles under which the tracing rays are entering the system (field angles) are X = 0°/Y = 0°, X = 7.36°/Y = 4.16°, X = -7.36°/Y = -4.16°, X = 0°/Y = 4.16° and X = 7.36°/Y = 0° to cover all critical points of the sensor as shown in Figure A.1. These field angles were chosen to cover the critical points of the sensor (14.208mm x 7.992mm) which will be used in the final experiment. As it can be seen from the figure, a total of five points are observed in the image plane. The circle represents boundary of the surface that the lens optically covers.

All simulations were done using three typical wavelengths, specifically 656nm, 587nm and 486nm which represent red, green and blue lights, respectively.

Three types of criterions were used to quantify the effects of the glass window insertion in our simulation:

- Optical path difference (OPD): the optical path difference is the difference between the real wavefront and a spherical reference wavefront. Rayleigh criteria says that if the OPD is less than or equal to one-quarter of the wavelength of the light, then the performance will be almost indistinguishable from perfect. This is also called peak-to-valley OPD,

- Root-Mean-Square (RMS) wavefront error: represents more of an averaging over the wavefront than the peak-to-valley OPD measure,

- Modulation transfer function (MTF).

The aforementioned measures were used to evaluate the three optical setups shown in Figure A.2. The setup shown on the top is the reference design with lens and sensor only. This is a baseline case. The second case, shown in the middle, has the 2 mm optical window inserted between the lens and the sensor. The third case has the optical window tilted for 1.250° around two perpendicular axes, and represents the worst case scenario in our optical setup. This angle is a required angle to achieve the desired ray displacement. The optical window results in a longer optical path; therefore there is a difference in the position of the detector between the baseline and the other two cases.

All the figures presented in the following text are the results of simulations with Code V software package. Figures A.3-A.5 show the optical path differences for all field angles. It can be seen in Figure A.3—the lens without the glass window—that the OPD is less than 1/4 of the wavelength of light. That implies a near perfect lens, limited only by the diffraction limit. In Figures A.4 and A.5 the worst results are highlighted. They are, as expected, for a situation when the window is tilted for 1.250° around both perpendicular axes. Table A.1 shows the RMS of OPDs for all three cases, while Figures A.6-A.11 show

the MTFs of all three cases. Each optical setup is accompanied by two MTF curves: the first one shows the MTF up to the diffraction cut-off frequency. The second graph shows the MTF up to the Nyquist frequency of the sensor which is 67 lp/mm.

It is important to remember here that the second and third optical arrangements represent only two of many positions of the dynamically controlled optical low-pass filter. During the exposure time, the window moves around two axes, and dwells on these two particular positions only for a fraction of the total exposure time. Therefore, the degradation caused by the window located as shown in the third case will have less influence than the window positioned normally to the optical axes.
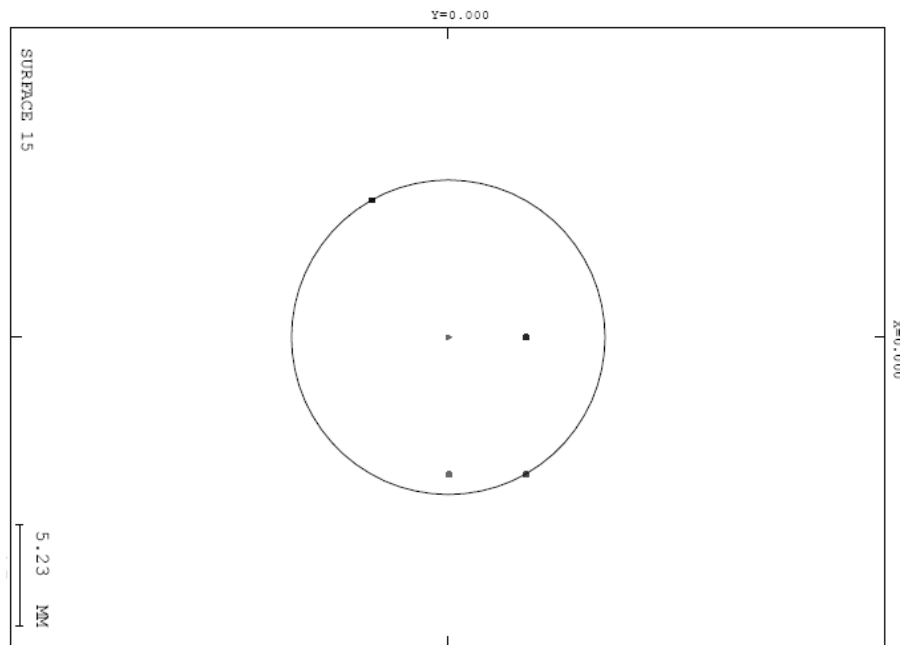
Figure A.1: The three systems under evaluation are tested with five field angles chosen to cover the critical points of the sensor. The circle represents the boundary of the surface that the lens optically covers.

Figure A.2: The three optical setups used in the simulation. Top figure shows the setup without the optical window, used as a reference setup. The middle figure shows the setup with the window perpendicular to the optical axis. The window in the last setup is tilted to displace the passing rays.

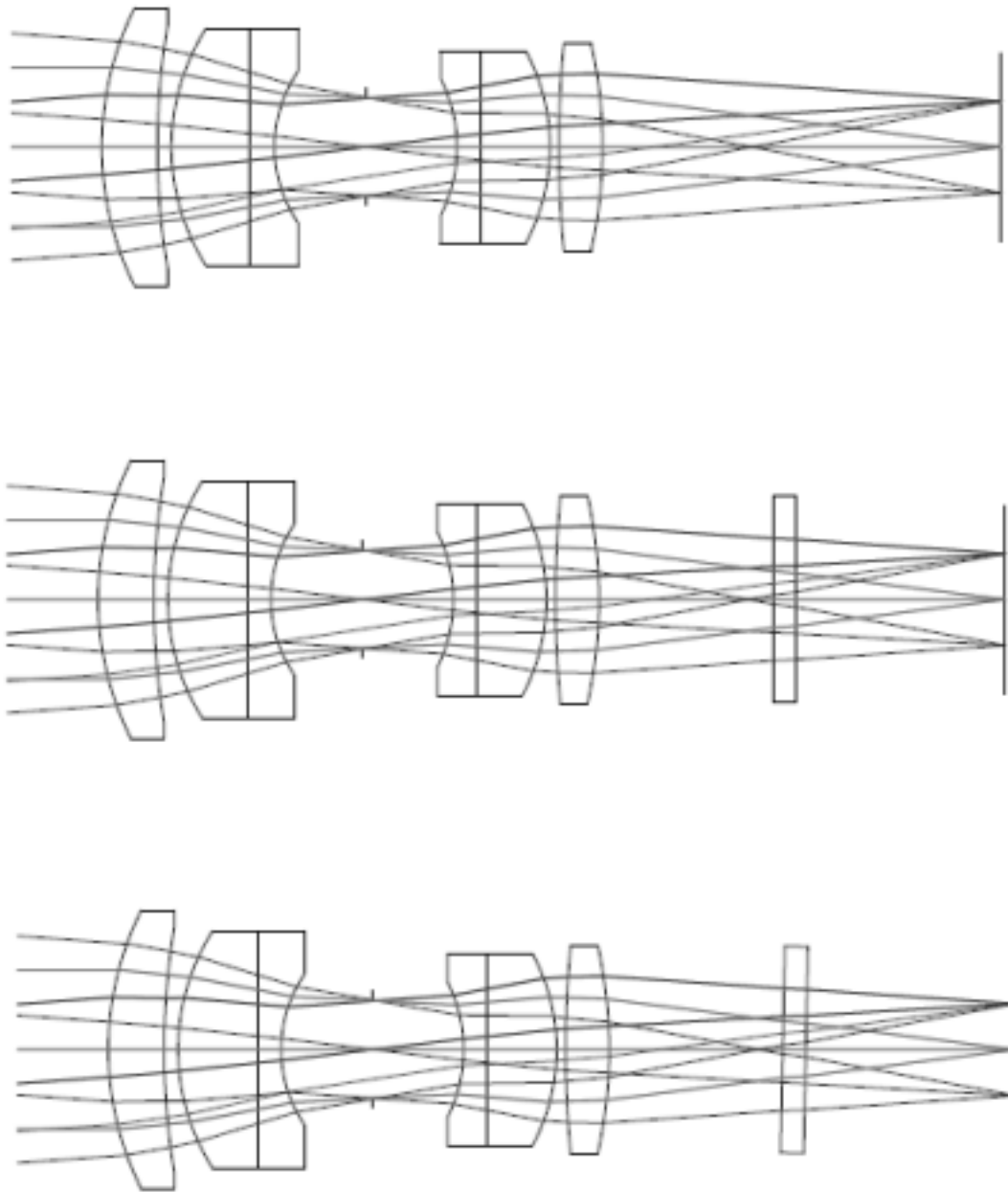|		Field	Best individual focus			Best composite focus		
		Degrees	Shift [mm]	Focus [mm]	RMS [waves]	Shift [mm]	Focus [mm]	RMS [waves]
Reference Design	X	0.00	0.000000	0.000569	0.0481	0.000000	0.000000	0.0481
	Y	0.00	0.000000			0.000000		
	X	7.36	-0.000274	-0.001539	0.0536	-0.000120	0.000000	0.0540
	Y	4.16	-0.000160			-0.000072		
	X	-7.36	0.000274	-0.001540	0.0536	0.000120	0.000000	0.0540
	Y	-4.16	0.000160			0.000072		
	X	0.00	0.000000	0.001629	0.0502	0.000000	0.000000	0.0506
	Y	4.16	0.000291			0.000197		
	X	7.36	0.000103	0.000600	0.0505	0.000043	0.000000	0.0506
	Y	0.00	0.000000			0.000000		
							Composite RMS :	0.05145
With DOLPF 0°	X	0.00	0.000000	-0.004837	0.0468	0.000000	0.000000	0.0509
	Y	0.00	0.000000			0.000000		
	X	7.36	-0.000535	0.002074	0.0860	-0.000744	0.000000	0.0864
	Y	4.16	-0.000305			-0.000424		
	X	-7.36	0.000536	0.002071	0.0859	0.000744	0.000000	0.0863
	Y	-4.16	0.000305			0.000424		
	X	0.00	0.000000	-0.001208	0.0519	0.000000	0.000000	0.0522
	Y	4.16	-0.000239			-0.000170		
	X	7.36	-0.000336	0.002455	0.0748	-0.000581	0.000000	0.0755
	Y	0.00	0.000000			0.000000		
							Composite RMS :	0.07167
With DOLPF 1.25°	X	0.00	-0.000137	-0.003500	0.0482	-0.000137	0.002386	0.0541
	Y	0.00	-0.000137			-0.000137		
	X	7.36	-0.000305	0.008166	0.0995	-0.000886	0.002386	0.1022
	Y	4.16	-0.000231			-0.000564		
	X	-7.36	0.000982	-0.001390	0.0758	0.000603	0.002386	0.0774
	Y	-4.16	0.000500			0.000282		
	X	0.00	-0.000137	0.002012	0.0571	-0.000137	0.002386	0.0571
	Y	4.16	-0.000330			-0.000308		
	X	7.36	-0.000248	0.007055	0.0852	-0.000713	0.002386	0.0873
	Y	0.00	-0.000133			-0.000133		
							Composite RMS :	0.07744

Table A.1. Tabulated RMS of OPDs for all field angles and all three optical systems used in the simulation.
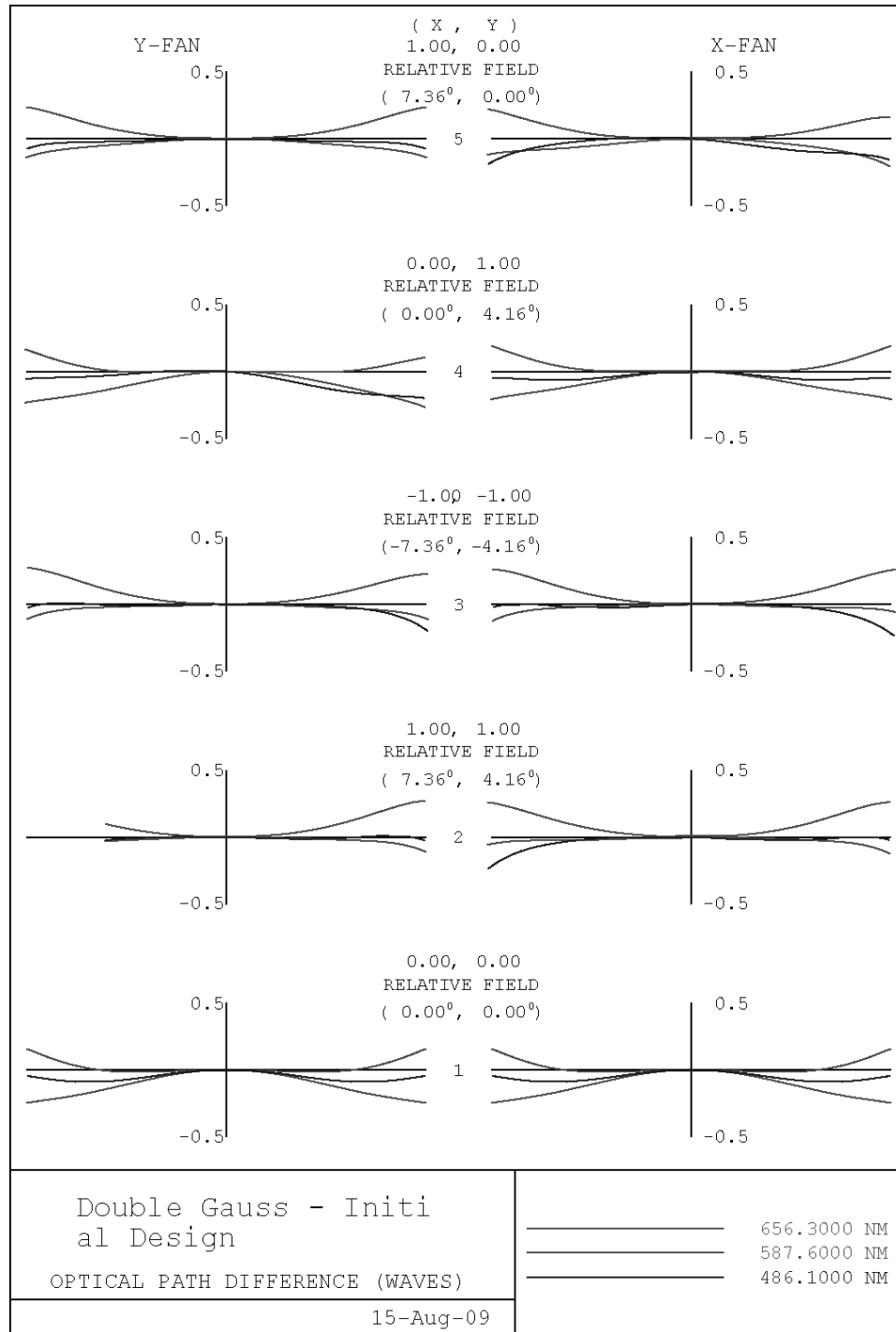
Figure A.3: Optical path differences for the reference system evaluated at the five critical field angles.
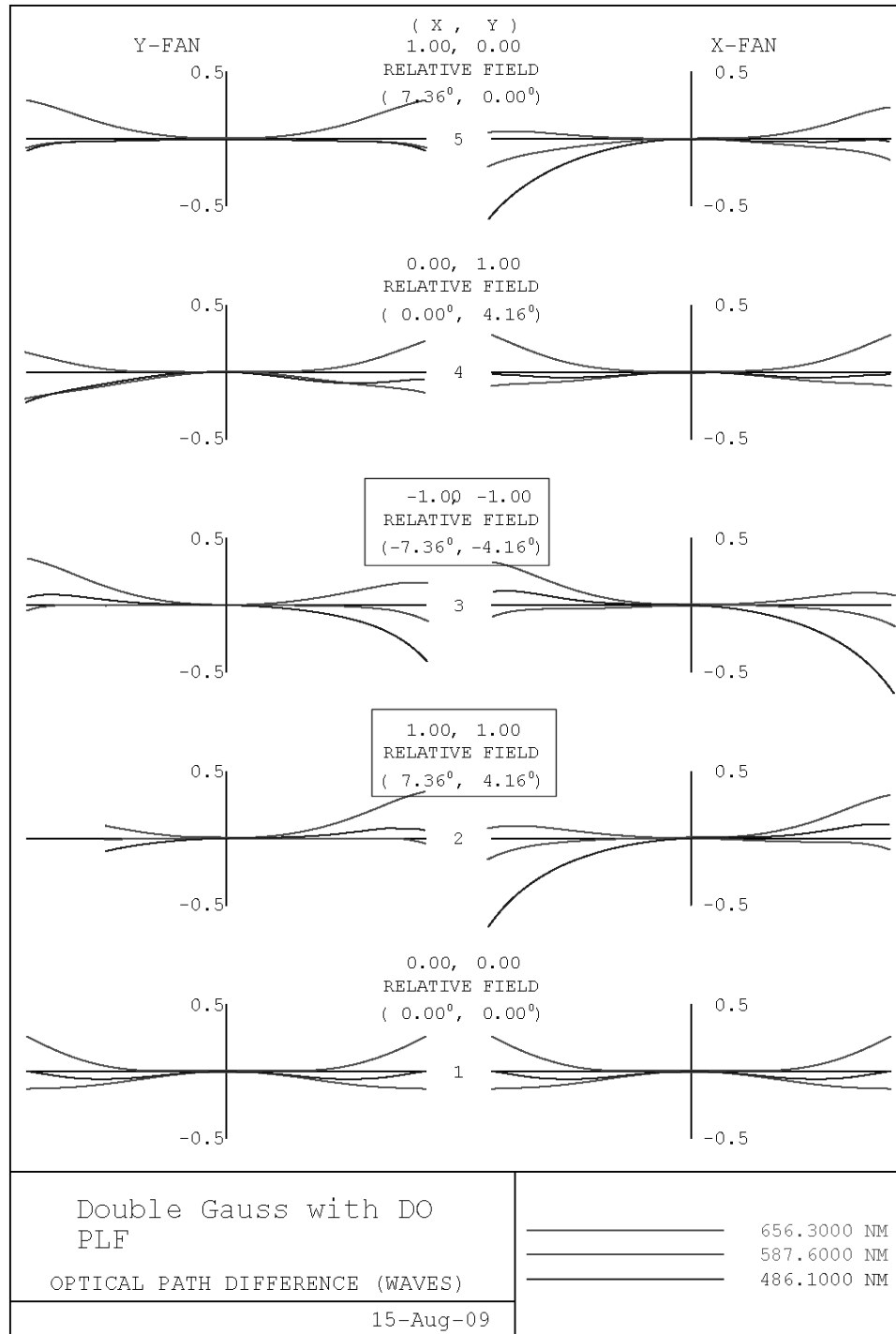
Figure A.4: Optical path differences for the system, with the optical window perpendicular to the optical path, evaluated at the five critical field angles.
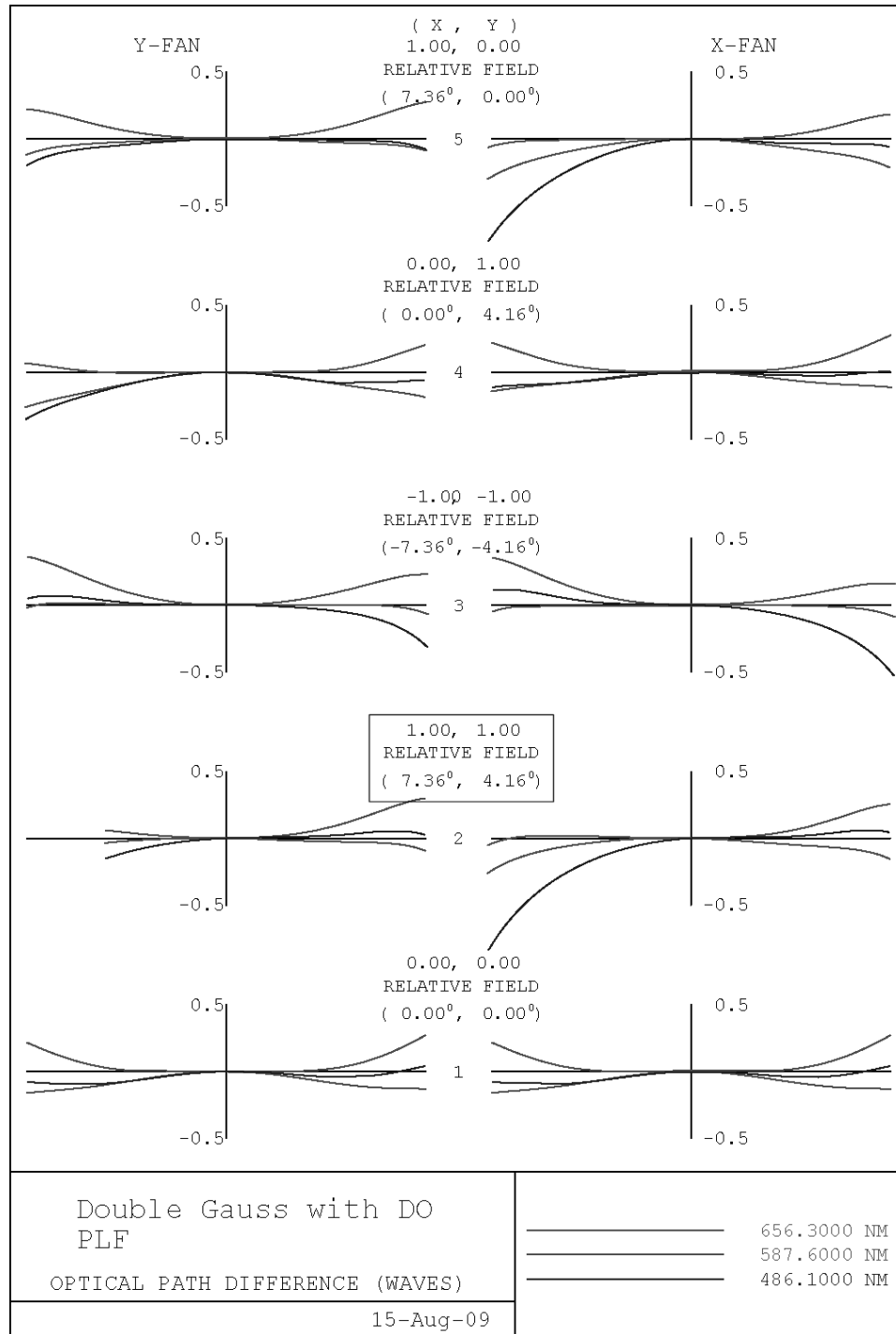
Figure A.5: Optical path differences for the system, with the tilted optical window, evaluated at the five critical field angles.
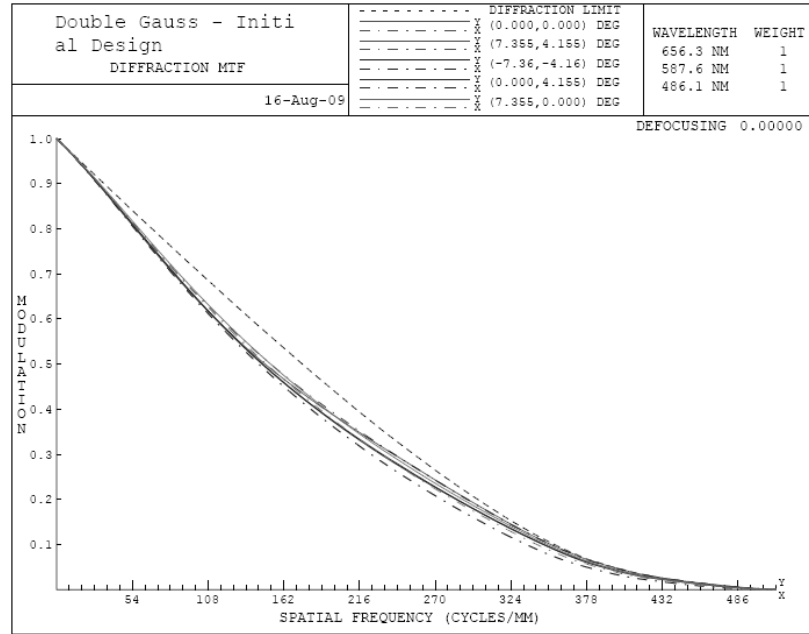
Figure A.6: MTFs of the reference system evaluated up to the cut-off frequency.
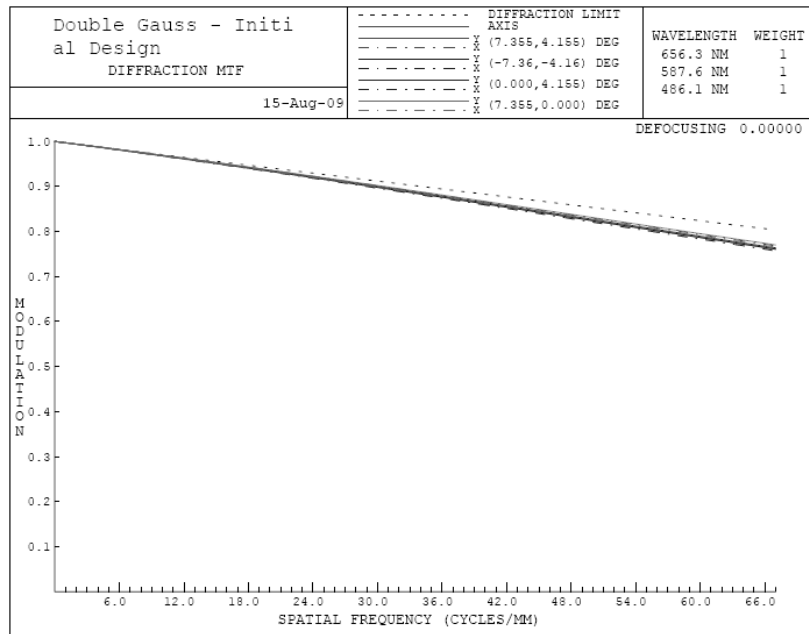
Figure A.7: MTFs of the reference system evaluated up to the sensor Nyquist frequency.

Figure A.8: MTFs of the system, with the optical window perpendicular to the optical axis, evaluated up to the cut-off frequency.

Figure A.9: MTFs of the system, with the optical window perpendicular to the optical axis, evaluated up to the sensor Nyquist frequency.

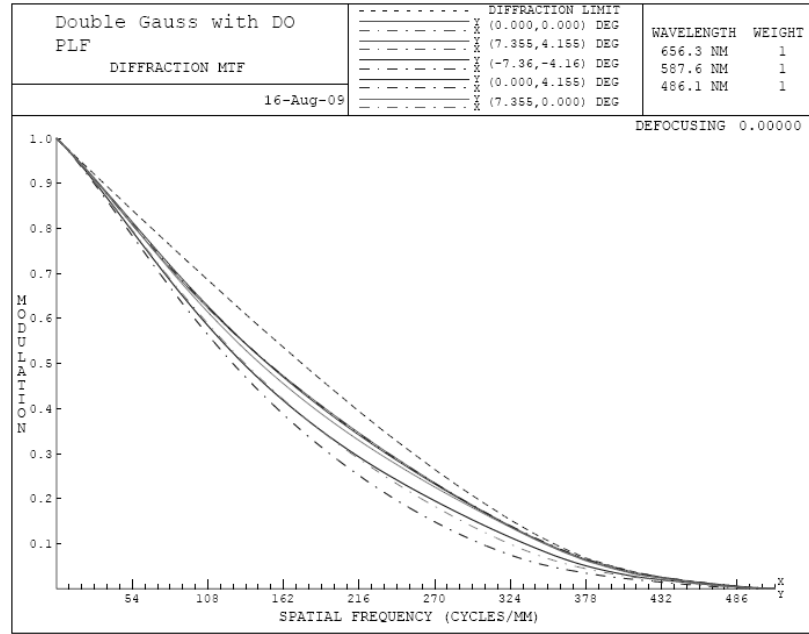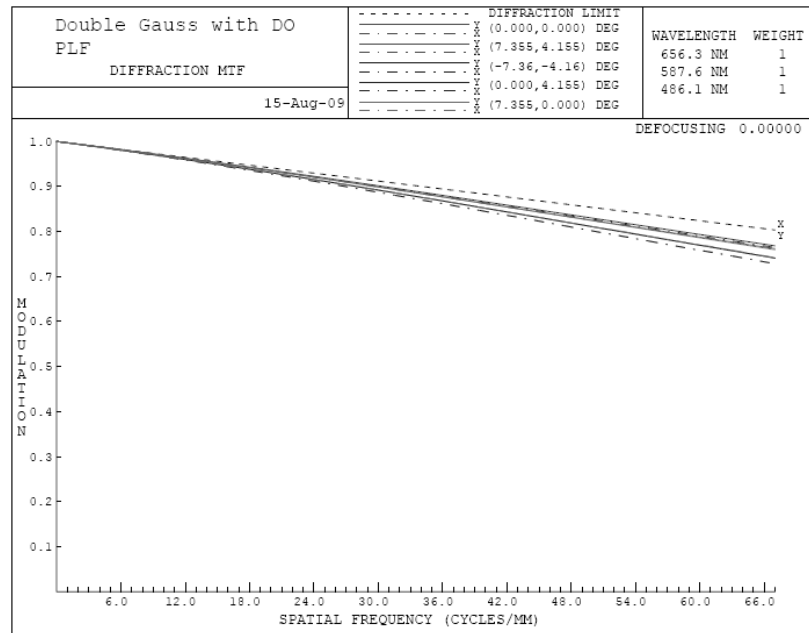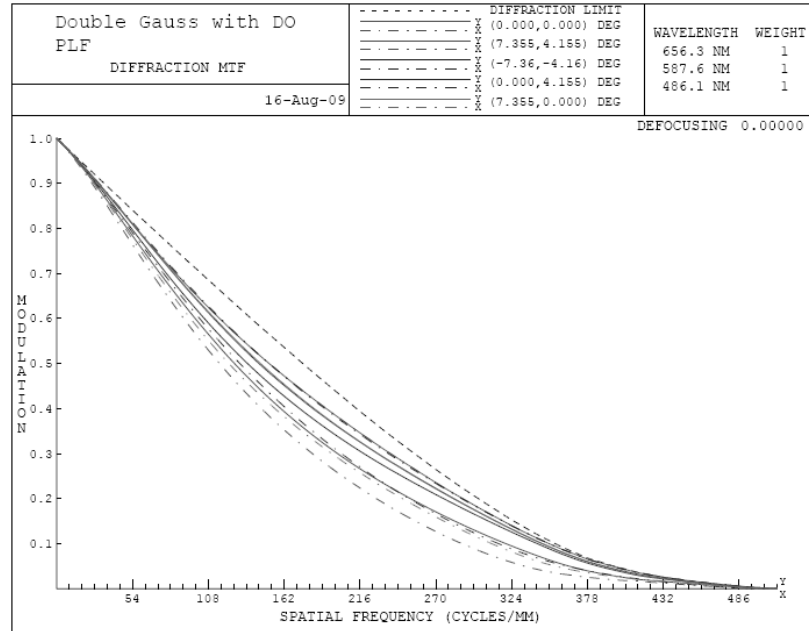Figure A.10: MTFs of the system, with the optical window tilted, evaluated up to the cut-off frequency.
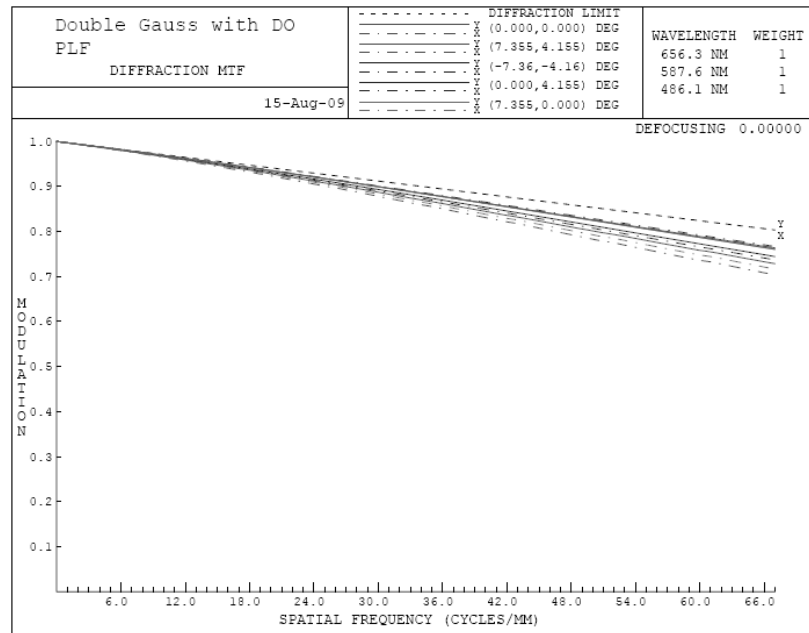
Figure A.11: MTFs of the system, with the optical window tilted, evaluated up to the sensor Nyquist frequency.

Bibliography

[1]   G.D. Boreman, *Modulation Transfer Function in Optical and Electro-Optical Systems*, Washington: SPIE-The International Society for Optical Engineering, 2001.

[2]   R. E. Fischer, B. Tadic-Galeb, and P. R. Yoder, *Optical System Design*, 2nd ed. New York: McGraw-Hill, 2008.

[3]   Panavision Imaging Technical Staff, *Dynamax-35 Product Brief*, Panavision Imaging, 2009.

[4]   Y. Wang, J. Ostermann, and Y. Zhang, *Video Processing and Communication*, Upper Saddle River, NJ: Prentice-Hall, 2002.

[5]   J. Nakamura, Ed., *Image Sensors and Signal Processing for Digital Still Cameras*, Boca Raton, FL: CRC Press, 2006.

[6]   A. V. Oppenheim, R. W. Schafer, and J. R. Buck, *Discrete-Time Signal Processing*, 2nd ed. Upper Saddle River, NJ: Prentice-Hall, 1998.

[7]   Kodak Technical Staff, *KAC-9647 CMOS Image Sensor*, Rev. 1.92, Eastman Kodak Company, September 2004.

[8]   J. W. Goodman, *Introduction to Fourier Optics*, 3rd ed. Englewood, CO: Roberts & Company, 2005.

[9]   D. H. Pritchard, "Adjustable bandwidth optical filter", U.S. Patent 3,588,224, June 28, 1971.

[10]   D. Kessler, "Anti-aliasing low-pass blur filter for reducing artifacts in imaging apparatus", U.S. Patent 6,937,283, August 30, 2005.

[11]   Y. Ogawa, Y. Nakada, H. Yasui, S. Ochi, "Development of CCD Imaging Block For Single Chip Color Camera", *IEEE Transactions on Consumer Electronics*, vol. CE-31, Issue 3, August 1985.

[12]   Q. Xunjun, L. Bin, and C. Xiangqun, "Optimization and test of two-dimensional birefringent low-pass filter", *Proc. SPIE,* vol. 6722, 2007.

[13]   Z. Tingyu, W. Rong, L. Yuling, and Y. Feihong, "Characteristic-analysis of optical low pass filter used in digital camera, *Proc. of SPIE,* vol. 6034, 2006.

[14]   L. Xiaoyan, J. Shangzhou, and L. Wang, "Design of double refractive pattern recognition system for optical low pass filter", *Proc. of SPIE,* vol. 6834, 2007.

[15]   L. Bin, C. Zhebo, and C. Xiangqun, "The performance of optical low pass filter", *Proc. of SPIE* ,vol. 5279, 2004.

[16]   J. Greivenkamp, "Color dependent optical prefilter for the suppression of aliasing artifacts", *Applied Optics*, vol. 29 no. 5, 1990.

[17]   J. Greivenkamp, "Optical spatial frequency filter", U.S. Patent 4,574,193, March 11, 1986.

[18]   E. Hecht, *Optics*, 4th ed. San Francisco: Addison Wesley, 2002.

[19]   I. Takanashi, "Optical comb filter", U.S. Patent 4,227,208, October 7, 1980.

[20]   Sony Technical Staff, *HDW-F900 Operational Manual*, Sony Corporation, 2000.

[21]   H. Okada, "Image input apparatus having a spatial filter controller", U.S. Patent 5,834,761, November 10, 1998

[22]   K. Nishioka, "Optical low-pass filter without using polarizes", U.S. Patent 5,091,795, February 25, 1992.

[23]   K. Nishioka, "Television camera for endoscopes provided with an optical low-pass filter", U.S. Patent 4,805,028, October 19, 1987

[24]   G. Kreymerman, "Adjustable opto-acoustical low-pass filter and technique", U.S. Patent 6,356,379, March 12, 2002

[25]   L. Yunchuan, L. Bin, W. Zhuangfei, Z. Liewei, and C. Xiangqun, "Digitalization measurement of structure parameters of optical-low pass filter", *Proc. of SPIE*, vol. 6150, 2006.

[26]   M. Mino, "Optical low-pass filter", U.S. Patent 3,756,695, July 12, 1971.

[27]   H. Nishino, "Optical low pass filter", U.S. Patent 3,768,888, July 21, 1971.

[28]   H. Abe, "Color television camera optical system", U.S. Patent 3,940,788, December 6, 1973.

[29]   S. Ohneda, "Color encoding video system with optical low-pass filter", U.S. Patent 4,101,929, February 15, 1977.

[30]   T. Shinozaki, "Optical low-pass filter", U.S. Patent 4,472,735, April 17, 1981.

[31]   K. Ise, "Optical low-pass filter utilizing a phase grating", U.S. Patent 4,795,236, December 20, 1985.

[32]   K. Ise, "Optical low-pass filter", U.S. Patent 4,878,737, December 16, 1987.

[33]   W. Plummer, "Anti-aliasing optical system with pyramidal transparent structure", U.S. Patent 4,989,959, June 12, 1989.

[34]   O. Yong-Ho, G. Chun-Soo, L. Jai-Cheol, L. Sungwoo, and K. Shi-Ho, "Comparison of a grating optical lowpass filter with a birefringent filter", *Proceedings of SPIE,* vol. *4594*, 2001.

[35]   L. Bergmann, and C. Schaefer, *Optics of Waves and Particles*, Berlin: Walter de Gruyter, 1999.

[36]   R. B. Rauch, "Image registration for raster output scanner (ROS) color printer", U.S. Patent 5,821,971, October 13, 1998.

[37]   D. C. Redpath, "Image motion detection system", U.S. Patent 3,561,870, February 9, 1971.

[38]   *Code V: Optical Design & Analysis software for Imaging and Telecommunication Optics* [CD-ROM]. Pasadena, CA: Optical Research Associates, 2009.

[39]   *Zemax-EE: Software for Optical System Design* [CD-ROM]. Bellevue, WA: ZEMAX Development Corporation, 2009.

[40]   B. L. Benamati, "In Search of the Ultimate Image Sensor", Photonics Spectra by Laurin Publishing, September 2001.

[41]   D. G. Manolakis, V. K. Ingle, and S. M. Kogon, *Statistical and Adaptive Signal Processing*, McGraw-Hill Higher Education, 2000.

[42]   F. J. Harris, "On the Use of Windows for Harmonic Analysis with the Discrete Fourier Transforms", *Proceedings of IEEE*, vol. 6, no. 1, January 1978.

[43]   V. V. Parsolov, *Polynomials*, , 2nd ed. Berlin, 2001.

[44]   J. G. Proakis and D. G. Manolakis, *Digital Signal Processing - Principles, Algorithms, and Applications*, 3rd ed. Upper Saddle River, NJ: Prentice-Hall, 1996.

[45]   Durst Phototechnik Technical Staff Large Format Division, *Lambda 131 HS Large Format Digital Laser Imager*, Durst Phototechnik AG, August 2006.

[46]   Sekonic Technical Staff, *Exposure Profile Target II*, Sekonic Corporation, 2009

[47]   Prosilica Technical Staff, *User Manual GE 1900/GE 1900C*, Prosilica Inc., December 15, 2009.

[48]   Kodak Technical Staff, *Kodak KAI-2093 Image Sensor*, Rev. 3.0, Eastman Kodak Company, March 19, 2007.

[49]   Beck Technical Staff, *Hardware Manual IPC@CHIP Embedded Controller Family SC123/SC143*, Rev. 1.02, BECK IPC GmbH, April 2006.

[50]   Xilinx Technical Staff, *Virtex-II Pro and Virtex-II Pro X FPGA User Guide*, Xilinx, March 23, 2005.

[51]   W. E. Singhose and S. T. Towell, "Double-Pendulum Gantry Crane Dynamics and Control", *Proceedings of IEEE International Conference of Control Applications*, 1-4 September, 1998.